



Plumbing System Architecture and Differentiation Processes of the Nyiragongo Volcano, DR Congo

Sander M. Molendijk ^{1,2,*}, Olivier Namur¹, Ephrem Kamate Kaleghetso^{1,3,4}, Paul R. D. Mason⁵, Benoît Smets^{6,7}, Jacqueline Vander Auwera² and David A. Neave ⁸

¹Department of Earth and Environmental Sciences, KU Leuven, Celestijnenlaan 200E, 3001 Leuven, Belgium

²Département de Géologie, Université de Liège, Allée du Six-Août 12, B-4000 Liège, Belgium

³Goma Volcano Observatory, Avenue du Rond-Point 142, Goma, Democratic Republic of the Congo

⁴Département de Géologie, Université de Goma, Avenue Ishasha 32, Goma, Democratic Republic of the Congo

⁵Department of Earth Sciences, Utrecht University, Princetonlaan 8A, 3584 CB Utrecht, The Netherlands

⁶Natural Hazards and Cartography Service, Royal Museum for Central Africa, Leuvensesteenweg 13, B-3080 Tervuren, Belgium

⁷Department of Geography, Vrije Universiteit Brussel, Pleinlaan 2, B-1050 Brussels, Belgium

⁸Department of Earth and Environmental Sciences, The University of Manchester, Oxford Road, M13 9PL Manchester, United Kingdom

*Corresponding author. E-mail: sander.molendijk@kuleuven.be

The Nyiragongo volcano is one of the most alkali-rich volcanic centres on the planet ($\text{Na}_2\text{O} + \text{K}_2\text{O}$ generally >10 wt.%, alpaite index up to 1.34), characterized by a semi-permanently active lava lake which hosts silica-undersaturated ($\text{SiO}_2 < 40$ wt.%), low viscosity lavas. To improve our understanding of this unique magmatic system, we present a set of 291 samples, acquired during new field excursions between 2017 and 2021. The major and trace element composition of all samples was measured, revealing a lithological range extending from primitive picrites (Mg\# 82) erupted from parasitic cones to a variety of highly evolved nephelinites, leucitites, and melilitites erupted from the main edifice as recently as 2002, 2016, and 2021.

We measured major and trace element compositions from the full spectrum of minerals present in all sampled lithologies. From these we calculated that the main magma reservoirs feeding Nyiragongo are at approximately 9–15 and 21–33 km depth, in agreement with recent seismic observations. Fractional crystallization modelling using observed mineral compositions and proportions was performed to quantitatively link the lithologies to specific residual liquid fractions assuming evolution from an olivine-melilitite parental melt.

Our modelling indicates that fractionation and cumulate formation in deep chambers reduces the remaining melt fraction to ~60%, after which melts are injected into upper, liquid dominated magma chambers where fractionation and accumulation of clinopyroxene, melilite, and feldspathoids dominates.

Characterisation of mineral textures and geochemistry reveals high crystal mobility in a repeatedly recharging plumbing system split between liquid-dominated, evolved magma chambers and more solid-dominated, primitive mushes, decreasing in liquid fraction with depth.

Key words: Nyiragongo; lava lake; alkaline magmatism; feldspathoids; plumbing system

INTRODUCTION

The Nyiragongo volcano (DR Congo), located on the western branch of the East African Rift System (EARS), is one of most silica-undersaturated ($\text{SiO}_2 < 40$ wt.%) volcanic systems active on Earth, which is best compared with the carbonatitic Oldoinyo Lengai in Tanzania and the now extinct Mt Etinde in Cameroon (Nkoumbou *et al.*, 1995). It is characterized by a semi-permanently active lava lake and low-viscosity lavas that impacted the city of Goma destructively as recently as January 2002 (Komorowski *et al.*, 2002) and May 2021 (Smittarello *et al.*, 2022). The silica-undersaturated character of the lavas is reflected in a variety of alkaline lithologies including (olivine-) melilitites, nephelinites, and leucitites (Tazieff, 1949; Sahama, 1953a; Sahama & Meyer, 1958; Sahama, 1978; Demant *et al.*, 1994; Platz *et al.*, 2004) which make them unique even within the alkaline Virunga Volcanic Province (VVP) (Fig. 1a, b) and wider EARS (Haapala, 2011;

Barette *et al.*, 2017). The formation of these lavas must require a unique combination of mantle source and plumbing system characteristics, the nature and structure of which remain poorly constrained. This limits our understanding of subsurface processes active in volcanically active continental rift settings as a whole and hampers any attempts to adequately predict volcanic hazards in such areas. Moreover, in part due to its continuous activity, Nyiragongo and Nyamulagira (Fig. 1b, d) together represent one of the largest global sources of volcanic SO_2 (3.5 kt/day of the global 63 kt/day) and CO_2 (7–12 kt/day, Nyiragongo during normal intra-crater activity) (Carn, 2002; Sawyer *et al.*, 2008; Carn *et al.*, 2017; Aiuppa *et al.*, 2021), meaning that they may have a global influence on atmospheric processes. Lastly, understanding the only currently active system of this kind may help us to understand similar historic systems.

Although the first scientific expedition to Nyiragongo was carried out in 1949 by Tazieff (1949), most of the key petrological work

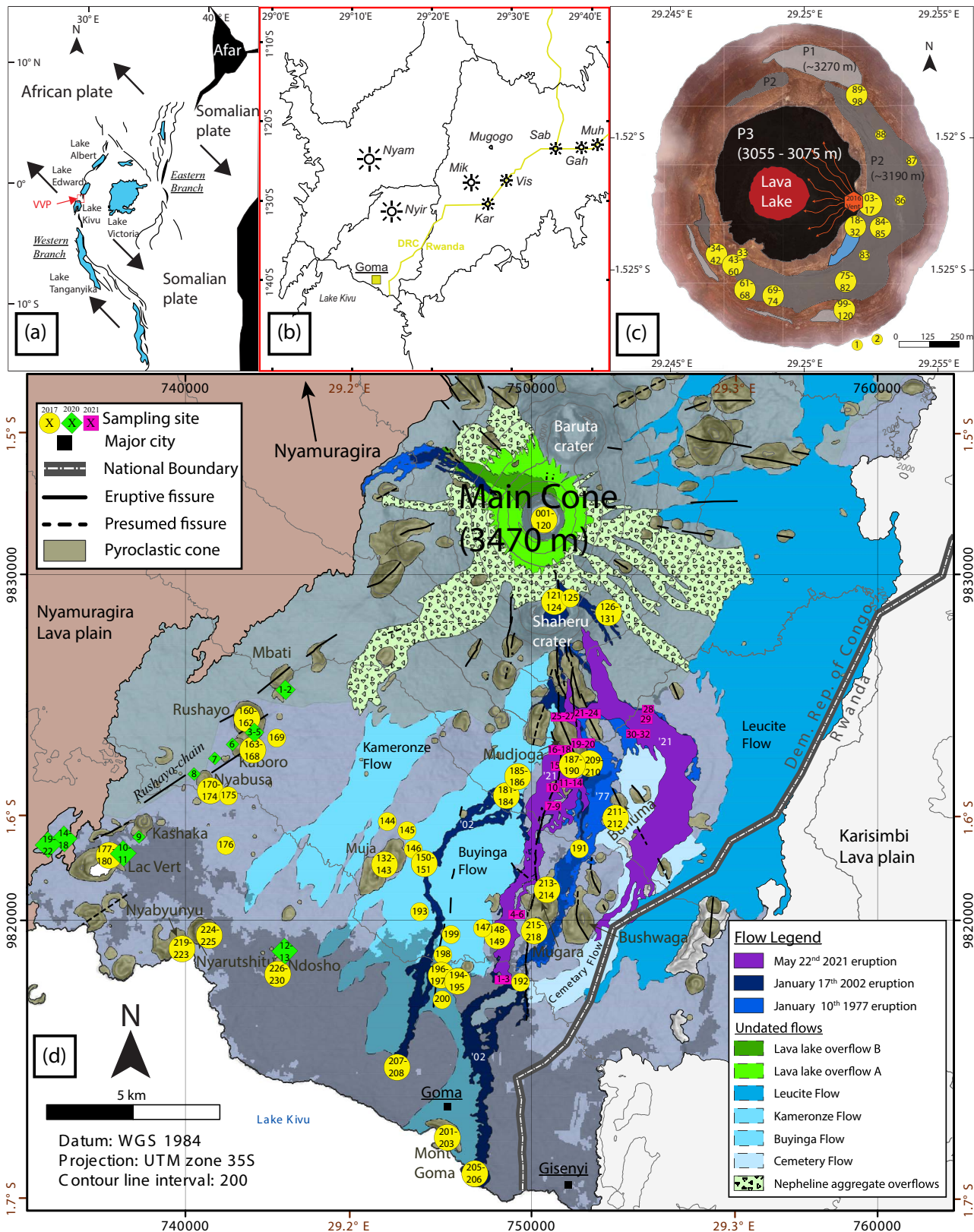


Fig. 1. Overview of the Nyiragongo volcanic field in context of the (a) East African Rift System (EARS) and (b) Virunga Volcanic Province (VVP) including sampling sites for whole-rocks in the (c) main crater and (d) surrounding area. From west to east, map (b) denotes the volcanic edifices of Nyamulagira (Nyam), Nyiragongo (Nyir), Mikeno (Mik), Karasimbi (Kar), the Mugogo cone, Visoke (Vis), Sabinyo (Sab), Gahinga (Gah), and Muhavura (Muh). Map (d) is based on the maps by Thonnard & Denaeyer (1965) and Smets & Poppe (2016). Altitudes shown in (c) are from time of sampling and are no longer accurate. Sampling markers from the original 2017 expedition are circular, whereas samples collected in 2020 and 2021 are shown in diamonds and rectangles, respectively. Sample numbers match those of Electronic appendix 1 Table S1.

on Nyiragongo was performed by Th. G. Sahama and K. Hytönen following various expeditions within the Virunga National Park that took place between 1952 and 1972 (Sahama, 1953a, 1953b, 1962, 1968, 1978; Sahama & Hytönen, 1957; Sahama & Meyer, 1958). These early studies recorded the mineralogical diversity at Nyiragongo and constructed a preliminary model for its eruptive behaviour through time (Sahama, 1953a, 1964, 1968, 1973; Sahama & Hytönen, 1957) in collaboration with, and building on the data of multiple authors (e.g. Denaeyer, 1952, 1963, 1966, 1969, 1972, 1975; Sahama & Meyer, 1958).

Recent eruptions (1977, 2002, 2021) are dominated by foiditic compositions erupted from the volcano's flanks that are compositionally similar to the summit lava lake ($\text{SiO}_2 = 39\text{--}41$ wt.%, $\text{Na}_2\text{O} + \text{K}_2\text{O} = 10\text{--}11$ wt.%) (Sahama, 1978; Santo *et al.*, 2002; Minissale *et al.*, 2019; Smittarello *et al.*, 2022). Nevertheless, the full range of reported lithologies from the Nyiragongo volcanic field stretches from highly primitive picrites ($\text{Mg}\# = 86$, calculated with all Fe as Fe^{2+}) to evolved peralkaline glasses ($\text{Mg}\# = 24$, $(\text{Na} + \text{K})/\text{Al} \geq 2$) (Demant *et al.*, 1994; Andersen *et al.*, 2012). Despite ample studies, much about the plumbing system of Nyiragongo remains unknown. No definitive constraints on the number and depths of magma reservoirs are available, complicating seismic interpretations of signals that may indicate imminent eruptions. Moreover, the parental magma composition and crystallization sequence of Nyiragongo remain a subject of debate (Platz *et al.*, 2004; Chakrabarti *et al.*, 2009a), making it unclear to what degree the unusual composition of the main cone lavas may be attributed to its source or its plumbing system.

Here we apply geochemical and imaging methods to a collection of 291 newly collected samples to construct a detailed geochemical and textural dataset of Nyiragongo's lavas and thereby gain insights into its plumbing system. Specifically, we use mineral, whole-rock data, and modern geothermobarometric techniques to discern the nature and location of dominant magma reservoirs. We then use modelling to explain the formation of the extreme lava compositions erupted by both the main-cone complex and parasitic cones of Nyiragongo.

GEOLOGICAL SETTING

The Nyiragongo volcano is located on the western branch of the EARS which, along most of its length, separates the Congolese craton from the Tanzanian craton (Ebinger, 1989; Chorowicz, 2005) (Fig. 1a). The EARS is one of few global examples of an active continental rift, with its earliest manifestations dating back to ~ 30 Ma, associated with extensive plume-generated volcanism along the northern rift segments at the future Red Sea, eastern Gulf of Aden and, central Ethiopian Plateau (Hoffman *et al.*, 1997; Ebinger & Sleep, 1998; Ebinger & Furman, 2003). South of current Ethiopia, at approximately 3°N , the rift subdivides into western and eastern branches (Fig. 1a), which coincide with the margins of the deep-rooted Archaean Tanzanian craton (McConnel, 1972; Ebinger, 1989; Ebinger & Sleep, 1998; Chorowicz, 2005; Stamps *et al.*, 2008). The VVP is located mid-branch on the western branch of the EARS, on the topographical rise of the Kivu dome (Ebinger & Furman, 2003; Chorowicz, 2005); (Fig. 1a). Volcanism in this region started at around 11 Ma (Bellon & Pouclet, 1980; Kampunzu *et al.*, 1998) and is still locally active, comprising eight main volcanic (composite) edifices (Nyamulagira, Nyiragongo, Mikeno, Karisimbi, Visoke, Sabinyo, Gahinga, and Muhavura) and hundreds of parasitic (mostly) monogenetic cones (Fig. 1b, d). Out of the eight main volcanoes, only Nyamulagira and Nyiragongo have been active in historic times (Komorowski *et al.*, 2002;

Tedesco, 2002; Smets *et al.*, 2015; Poppe *et al.*, 2016; Barette *et al.*, 2017; Pouclet & Bram, 2021; Smittarello *et al.*, 2022). Volcanism in the VVP and Kenya rift has been associated with a heterogeneous plume head beneath the Tanzanian craton (Chakrabarti *et al.*, 2009a), which has either experienced carbonate metasomatism itself (Chakrabarti *et al.*, 2009a, 2009b; Condomines *et al.*, 2015), or is causing erosional melting of comparably heterogeneous metasomatised lithospheric mantle (Vollmer & Norry, 1983; Furman & Graham, 1999; Furman *et al.*, 2015; Pitcavage *et al.*, 2023). As a result, eruption products in the VVP are alkaline to foiditic in composition (Baker *et al.*, 1972; Barette *et al.*, 2017). Lavas erupted in the VVP range from alkali basaltic and basaltic to trachytic, tephri-phonolitic and foiditic in composition (Barette *et al.*, 2017). Foidites are nevertheless limited to a small selection of samples from Visoke and Mikeno, the singular eruption of the Mugogo solitary cone (Fig. 1b) (Verhaeghe, 1958), and Nyiragongo.

The Nyiragongo volcanic field has three primary areas of eruptive activity: the main edifice including northern parasitic cones, the Rushayo (or Rusayo) chain in the south-west, and the Mudjoga-Bushwaga group of parasitic cones and fissures in the south-east (Fig. 1d). The main edifice of Nyiragongo (3470 m a.s.l.) is made of a summit crater flanked by two large inactive cones, Baruta (north, ~ 3100 m a.s.l.) and Shaheru (south, ~ 2800 m a.s.l.). The main body of lithologies reported from the volcano is derived from these three cones and mostly comprises porphyritic (clinopyroxene-) melilitites, nephelinites, and leucitites (Platz *et al.*, 2004). These rocks lack feldspars, and instead include significant amounts of melilite, nepheline, and leucite amongst lesser proportions of kalsilite, magnetite, apatite, olivine, and calcic-clinopyroxene. More scarcely reported accessory phases include perovskite and phlogopite (Sahama, 1962, 1968, 1978; Demant *et al.*, 1994; Platz *et al.*, 2004).

The eruptive history of Nyiragongo is dominated by lava lake activity within the crater (Barrière *et al.*, 2022), but three historical flank eruptions are also known from the years of 1977 (Pottier, 1978), 2002 (Komorowski *et al.*, 2002), and 2021 (Smittarello *et al.*, 2022). The lavas associated with these events erupted along a pre-existing N-S fracture system and their release was likely triggered by flank failure due to a combination of magmatic pressure and tectonic shock (Komorowski *et al.*, 2002; Wauthier *et al.*, 2012, 2015; Pouclet & Bram, 2021; Barrière *et al.*, 2022). In addition, recurrent eruptions along the same pathways likely introduced additional structural weaknesses, which are thought to have led to the eruption in 2021 (Smittarello *et al.*, 2022). Older, undated eruptive events are evidenced in the field as the southern lying Kameronze, Buyinga, and Cemetary flows, as well as the eastern Leucite flow and several overflow events (Demant *et al.*, 1994; Fig. 1d).

Changes in the recent eruptive activity of Nyiragongo left (remnants of) platforms in the summit crater testifying of the lava lake levels prior to flank eruptions. Before the 2021 eruption, 3 platforms (P) existed, with P1 and P2 representing the pre-1977 and pre-2002 crater bottom levels, respectively, and P3 being the active pre-2021 crater bottom (Tedesco, 2002; Durieux, 2004; Smittarello *et al.*, 2022; Fig. 1c). At the time of the first sampling expedition (June 2017) the lava lake and P3 were located at 3055–3075 m a.s.l., i.e. 115 to 135 m below P2, ~ 200 m below P1, and ~ 350 m below the crater rim. End of February 2016 a spatter cone emerged on P3 east of the lava lake, at the foot of the cliff leading to P2 (Balagizi *et al.*, 2016; Burgi *et al.*, 2018; Barrière *et al.*, 2022), which actively ejected material onto P3, and later, P2, until May 2021 (Fig. 1c). Just before the 2021 eruption, the eastern part of P3 reached the level of P2. When the eruption occurred,

the lava lake was drained, triggering a series of collapses of P3, which ultimately led to a ~850 m deep crater and the almost total disappearance of P3 (Smittarello *et al.*, 2023).

The main edifice is surrounded by approximately 100 parasitic cones distributed along radial fractures, the most significant being the Rushayo chain, located SW of the main edifice and oriented SW–NE (Denaeyer, 1975; Demant *et al.*, 1994; Fig. 1d). This collection of approximately 20 Holocene parasitic cones stretches from Rutoke cone in the north to Lake Kivu in the south (Fig. 1d). Contrary to the main cone, these eruptive centres have primarily produced mafic olivine-melilititic and olivine-nephelinitic lavas throughout their eruptive history (Denaeyer, 1975; Demant *et al.*, 1994). While the cones closer to the main edifice are primarily magmatic vents, those directly adjacent to Lake Kivu are dominantly of a phreatomagmatic nature (Denaeyer, 1975; Poppe *et al.*, 2016).

SE of the main edifice, the Mudjoga-Bushwaga group (Fig. 1d) contains a variety of parasitic cones and fissures, among which the northernmost are those of the 1977, 2002, and 2021 eruptions. Cones further south are reported to erupt clinopyroxene-rich nephelinites and melilite-nephelinites (Demant *et al.*, 1994). In between the two fissure-rich parasitic cone tracks are the isolated cones of Muja (Fig. 1d), which are uniquely known to have erupted picrites (Demant *et al.*, 1994). The easternmost Muti cone bordering the Karisimbi volcanic field was also noted to erupt clinopyroxene-rich plagioclase-bearing lavas (Demant *et al.*, 1994).

PETROLOGICAL CONTEXT

The first model of petrological evolution for Nyiragongo was presented by Sahama (1973, 1978). It indicated that Nyiragongo's eruptive activity started with an initial phase of explosive activity as carbonated, gas-charged nepheline-melilitite (bergalite) magma from the top of a magmatic column ascending from the mantle was erupted, building the first edifice. After exhausting this material confined to the top of the magma column, a compositional change to leucite-nephelinite magma occurred as deeper magma rose to the higher edifice, occasionally erupting and building the main cone structure. These authors determined that crustal contamination at Nyiragongo is minimal, and argued for a potential shared source between Nyamulagira and Nyiragongo, explaining the compositional difference between their lava compositions through gaseous transfer of alkalis (Sahama, 1973). More recent sampling and analyses have been performed which focus on the unique mineralogy of Nyiragongo (Hertogen *et al.*, 1985; Demant *et al.*, 1994; Platz *et al.*, 2004; Chakrabarti *et al.*, 2009a, 2009b; Andersen *et al.*, 2012, 2014; Minissale *et al.*, 2019) and the specific stages of magma production and evolution. These works will be presented here from source melting to mineral fractionation and eruption. The source of Nyiragongo's parental magmas was inferred to be heterogeneously enriched, and distinct from Nyamulagira (Vollmer & Norry, 1983; Furman & Graham, 1999), evidenced by unusual isotopic variations. This was attributed to mantle metasomatism of the subcontinental lithospheric mantle (SCLM) which was being eroded away by a mantle plume, triggering melting (Furman & Graham, 1999). The presence of such a plume, however, is still debatable, given that no convincing He-isotope signature, such as in Afar, is found in the area (Pik *et al.*, 2006). The plume hypotheses were continued by Chakrabarti *et al.* (2009a) who argued for the mantle plume under the Tanzanian craton to be heterogeneous in itself, causing melting of a variably carbonated garnet- and phlogopite-

bearing source at 80 (2.4 GPa) to 150 km (4.6 GPa) depth. They explain the volcanic activity around the entirety of the Tanzanian craton through this model and argue that the foiditic lavas of Nyiragongo's main cone must be primary in nature. Nevertheless, later work by Pitcavage *et al.* (2021), as well as Minissale *et al.* (2022) argued against a plume-source, favoring metasomatised SCLM source hypotheses, with melting triggered through thinning-driven adiabatic decompression.

Magmatic reservoir depths were listed in the abstract of Louaradi *et al.* (1993) who used melt- and fluid inclusion data from olivine and clinopyroxene phenocrysts. These authors agreed upon three major storage regions occurring at a depth of 27–30 km (790–880 MPa) (Rushayo olivine) 10–14 km (320–450 MPa) (olivine, clinopyroxene nephelinites), and < 1 km (feldspathoids). The 10–14 km reservoir was additionally backed up by geophysical observations by Tanaka (1983). Observations from work on ^{238}U - ^{230}Th - ^{226}Ra - ^{210}Pb disequilibria (Chakrabarti *et al.*, 2009b) discerned that Nyiragongo magmas ascend (in their assessment) rapidly (<8 ka) from the mantle to the volcanic edifice, but may stagnate in the upper reservoir system for years to decades before eruption in the lava lake or along the flanks.

The model of Sahama (1978) describing the development of the main cone (see geological setting) was expanded upon by Hertogen *et al.* (1985) who indicated the necessity of high-pressure clinopyroxene fractionation in addition to gas-fluxing. Demant *et al.* (1994) re-affirmed Sahama (1978)'s three-stage model and built on the detailed description of parasitic cone lithologies by Denaeyer (1966, 1969) to incorporate them into a general model for the whole Nyiragongo system through the accumulation of olivine and clinopyroxene.

The late stages of magmatic evolution at Nyiragongo were investigated by Platz *et al.* (2004), who reviewed the old sample collections of Sahama (1978) and Denaeyer (1969) and established a petrogenetic model for Nyiragongo driven by low-pressure (≤ 120 MPa) fractionation inside the volcanic edifice in combination with feldspathoid accumulation to form glomeroporphyritic lithologies (Platz *et al.*, 2004). These low pressures are required to produce leucite, which they believed to control fractionation at Nyiragongo given that it depletes the melt in silica. However, they reported that the first stages of magmatic evolution start with an olivine-melilitite parental melt such as is erupted by the parasitic cones (Demant *et al.*, 1994), which fractionates to pyroxene-nephelinite composition at 10–14 km depth (320–450 MPa) once again based on the work by Tanaka (1983) and the abstract by Louaradi *et al.* (1993) (Platz *et al.*, 2004). Their geochemical modelling approach was limited to major element modelling of olivine-melilitite to pyroxene-nephelinite chemistries, with which they explain the initial crystallization stage from parasitic-cone lavas to main-cone compositions. In addition, they refer to the work of Gee & Sack (1988) to explain the presence of high-Ca clinopyroxene in melilite-nephelinites through a peritectic reaction between olivine, melilite, and liquid. The petrographic features of lavas from the 2016 vent were described by Minissale *et al.* (2019), classifying them as glassy larnite-normative melilite nephelinites, and reporting glass-crystal partition coefficients. Most recently, the 2021 lavas were described and placed in context of the older eruptions by Minissale *et al.* (2022), and their chemical similarity to the 2002 lava compositions were confirmed by Smittarello *et al.* (2022) who described the volcano-tectonic mechanisms of the most recent eruption. The most extreme, peralkaline assemblages were found in residual melt pockets in vesicles of already evolved foidites. Minerals included in these were documented by Andersen *et al.* (2012, 2014) who showed that they

were produced in post-magmatic to sub-solidus recrystallization stages in response to thermal metamorphism and metasomatism.

The dynamics of the lava lake itself have been well-studied by a variety of authors (e.g. Burgi *et al.*, 2014; Smets *et al.*, 2017; Barrière *et al.*, 2019, 2022). Their work indicates that the upper vent system is governed by gas piston driven convection which brings gas-rich lavas to the surface. In addition, seismic activity at 11–15 km depth concurrent with lava-lake drops indicate partial draining of the lava lake as intrusions branch off at depth when sufficient overpressure is reached (Barrière *et al.*, 2019, 2022; Walwer *et al.*, 2023).

SAMPLING AND ANALYTICAL METHODS

Samples

Samples were collected during three expeditions to Nyiragongo in 2017, 2020, and 2021. Most samples were collected during the first expedition, when we aimed to collect all lithologies present insofar as was possible under safe conditions. The total collected volume from 2017 comprises 232 whole-rocks, 129 of which were derived from the central crater. The remaining samples were collected from flows from the southern lava fields (51), cones from the Bushwaga-Mudjoga chain and Muja (22), the phreatomagmatic cones bordering Lake Kivu (16), and the magmatic vents of the Rushayo chain (14) (Electronic appendix 1 Table S1, Fig. 1d). Samples from the central crater can roughly be divided into four categories: nephelinitic to melilititic fine grained ropy lava flows found on platforms (P1 and P2), glassy melilititic lava bombs ejected from the 2016 vent (Fig. 2a), scarce holocrystalline melilitite blocks sampled on the cliffs between P2 and P1, and highly phyrlic leucitites and nephelinites derived from dykes and lava flows forming the slopes between cliff platforms (Fig. 2b). The 2020 expedition targeted the Rushayo chain (Fig. 1d) in order to collect more primitive material, and comprises 26 additional samples, all of which are highly olivine-phyric (Fig. 2f, g). Lastly, 33 samples collected in May 2021 are exclusively sourced from the May 22nd 2021 lava flows (Fig. 1d). These lavas are subject to selective sampling of the upper parts of the flow, which causes some preferential enrichment of light nepheline (Fig. 2c,d). Such floatation was also observed in nepheline-rich flows found in the crater.

Petrographic methods

Petrographic study of our rock samples was performed using a Nikon optical microscope in reflected and transmitted light. Whole-section photographic images were taken with a Sony Alpha A7RII mirrorless digital camera equipped with a Sony FE 0 mm f/2.8 Macro G OSS Lens. Volume distributions of phases were determined through digital point-counting of thin section photographs, using JMicroVision v1.27 software. Samples with even phase distributions were measured using a rectangular grid, whereas a random grid was used for samples with heterogeneous phase distributions. Scanning electron microscope (SEM) images were used for point-counting of matrices whenever limits on crystal size prevented digital counting procedures.

A minimum of 1000 counts was applied for whole-sections, whereas with a minimum of 500 counts for sample matrices. Reported phase surface percentages are relative to the complete phenocryst content unless stated otherwise. SEM imaging of back-scattered electron (BSE) images was performed at KU Leuven, using a TESCAN MIRA 4 FEG equipped with a 4 quadrant Al-coated BSE detector. Operating conditions were 15 kV for all maps with a nominal beam current of ~1 nA and a working distance of

~10 mm. BSE maps of large crystals were taken at high-resolution (2048 x 2048 pixels; field of view = 100–500 μm) with a scan speed of 5 ms/pixels. Individual frames were stitched into single maps using Image Snapper Tescan. We also collected back-scattered electron images using a SEM and a JEOL JXA-8530F Hyperprobe at Utrecht University (see details below). We used an accelerating voltage of 15 kV, a probe current of 10 nA, a working distance of 11 mm, and an aperture of ± 60 nm.

Whole-rock chemistry

Major element compositions of all whole-rock samples were determined by X-ray Fluorescence (XRF) using an ARL PERFORM-X 4200 (Rh X-ray tube) spectrometer at the University of Liège. Samples were powdered at KU Leuven by first crushing the samples manually, after which a Pulverisette planetary micro mill was used to obtain a grain size of <1 μm . Resulting powders were dried at 1000°C for 2 hours to remove organics and determine the loss on ignition (LOI). The dried powder was mixed with lithium tetra- and metaborate (34/66 ratio) at ratio of 1:11 to produce glass discs for major element analysis. Major element calibration was performed using 66 international standards (magmatic whole-rocks, minerals, and soil samples). Accuracy was determined to generally be better than $\pm 5\%$ for all elements (see Electronic appendix 1). Likewise, repeated analyses of international and in-house standards indicate the 1σ analytical precision to be within 5% for major elements. Additional details on calibration, precision and accuracy can be found in Namur *et al.* (2020) and the raw data found in Electronic Appendix 1.

An additional 7 g of unheated material was used to make pressed powder pellets on which select minor and trace elements were measured (Co, Ni, Cu, Zn, Ga, Rb, Sr, Y, Zr, Nb, Th). Trace element data determined by XRF were only used for first order estimates, except for Nb and Zr, for which XRF data are preferred over ICP-MS data (see below). Quality of the trace element acquisition was estimated by repeated measurement of 11 international standards (GSD-10, GSD-9, JF-1, JR-1, Nim-D, Nim-G, Nim-L, Nim-N, Nim-P, STM-1, and SY-2). Accuracy is estimated better than $\pm 10\%$ and 1σ analytical precision is better than $\pm 3\%$ for all elements above 50 ppm.

We analysed the extended trace element content (⁴⁵Sc, ⁵¹V, ⁵²Cr, ⁵⁹Co, ⁶⁰Ni, ⁶³Cu, ⁶⁶Zn, ⁸⁵Rb, ⁸⁸Sr, ⁸⁹Y, ⁹⁰Zr, ⁹³Nb, ¹³³Cs, ¹³⁷Ba, ¹³⁹La, ¹⁴⁰Ce, ¹⁴¹Pr, ¹⁴⁶Nd, ¹⁴⁷Sm, ¹⁵¹Eu, ¹⁵⁷Gd, ¹⁵⁹Tb, ¹⁶³Dy, ¹⁶⁵Ho, ¹⁶⁶Er, ¹⁶⁹Tm, ¹⁷²Yb, ¹⁷⁵Lu, ¹⁷⁸Hf, ¹⁸¹Ta, ¹⁸²W, ²⁰⁸Pb, ²³²Th, ²³⁸U) of samples collected in 2017 using a PerkinElmer NexION 2000P ICP-MS at Utrecht University. We dissolved 125 mg of sample powder using a combination of HF, HNO₃, and HClO₄. Samples were first left to digest overnight at 90°C in a mixture of 2.5 ml HF and 2.5 ml mixed acid (HClO₄:HNO₃ = 3:2), after which excess acid was evaporated at 140°C. The leftover material was subsequently mixed with 25 ml of 1 M HNO₃, after which it was left to dissolve at 90°C for a minimum of 12 hours. Accuracy and precision were estimated by systematic measurement (n = 35) of a variety of international reference materials (AGV-1, AN-G, BE-N, BHVO-1, JB-2, JR-1, MA-N, MRG-1), blanks, and an in-house standard of Utrecht University (ISE921). A duplicate sample was also included in every batch for additional constraints on precision. Analytical accuracy is generally better than $\pm 10\%$ except for Cr ($\pm 12\%$), Y ($\pm 15\%$), and Ba ($\pm 12\%$). Elements Zr, Nb, Ta, and W were measured at such low accuracies (>25% for Zr, >100% for Nb, Ta, and W) that we report Zr and Nb data from XRF, whereas Ta and W measurements are disregarded entirely. The 1σ analytical precision of our analyses is <10% for all elements except for Nb ($\pm 24\%$), Ta ($\pm 48\%$) and W ($\pm 12\%$).

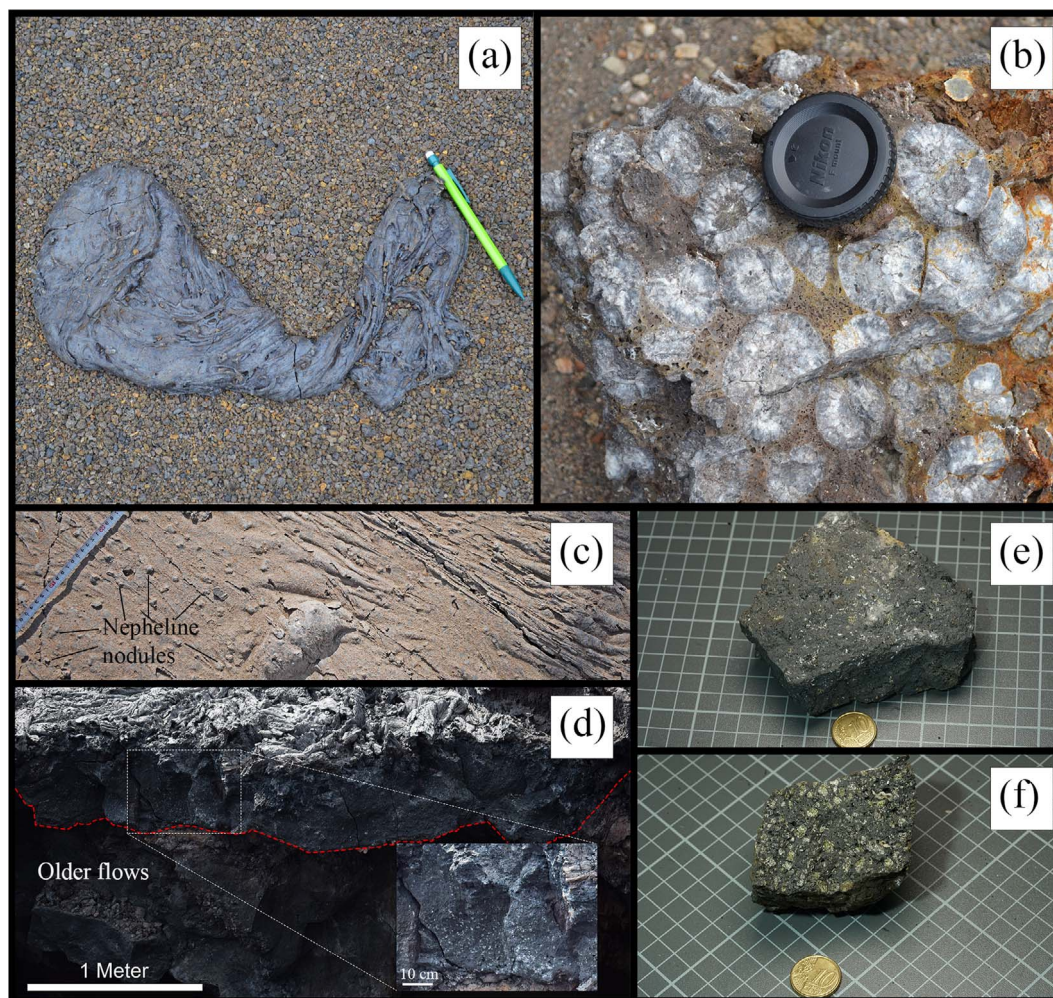


Fig. 2. Representative images of whole-rock samples as collected in the field. (a) A 2016 porphyritic melilitite as ejected from the 2016 vent and deposited on P2 (Fig. 1). (b) Hand sample of the massive leucitite lithology (see below), as recognized by cm-sized glomerocrysts in a fine-grained matrix. (c) and (d) are field images of the 2021 lava flow, displaying the abundance of nepheline nodules on top (c) and inside of (d) the flow. Panels (e) and (f) display a (e) picritic melilitite basalt from the Rushayo cone and (f) a picrite sample from the Muja cone, respectively. The background grid uses a 1 cm scale.

Electron microprobe analyses

Electron microprobe analysis (EMPA) was performed at Utrecht University using a JEOL JXA-8530F Hyperprobe. Operating conditions were 15 kV for all analysis, using a nominal beam current of ~15 nA for crystals and 8–10 nA for glasses. A standard beam size of 10 μm was applied unless crystal size or zoning warranted otherwise. On-peak counting times of 20 seconds were employed for all elements, with off-peak counting times of 10 seconds before and after analysis. Na and K were always measured first to avoid alkali-loss during analysis. Primary standardization was performed using Smithsonian VG-2 (Si, Al for glasses; NMNH 111240–52) and in house forsterite (Si for olivine), diopside (Si, Mg, Ca), corundum (Al), TiO-metal (Ti), hematite (Fe), synthetic KTIPO_5 (P, K), celestine (Sr), jadeite (Na), barite (Ba), tephroite (Mn), cancrinite (Cl), fluorite (F), KL-2 and GOR132-G glasses (Cr in olivine; from Jochum *et al.* (2006)), and MongOLSh11–2 olivine (Ni but also Si, Fe, Mg in olivine; from Batanova *et al.* (2019)). Secondary standardization was performed on Smithsonian VG-2, A-99, and IndianOcean basaltic glasses (NMNH 111240–52, NMNH 113498–1, and NMNH 113716–1, respectively), Kakanui augite (NMNH 122142), San Carlos olivine (NMNH 111312–44), ilmenite (NMNH 96189), microcline (NMNH 143966), fluorapatite (NMNH 104021),

and chromite (NMNH 117075). An overview of these analyses is provided in Electronic appendix 1 Table S2 and an overview of all measurement locations is supplied in Electronic appendix 2. Relative errors on major element concentrations based on secondary standard analyses are generally at <5% for all concentrations above 0.1 wt.%. Specifically, errors are 0.8% for SiO_2 , 1.8% for Al_2O_3 , 2.5% for MgO, 4% for TiO_2 , 1.8% for FeO, 1.4% for CaO, 7.6% for Na_2O , 5.4% for K_2O , 2.4% for P_2O_5 , 11.6% for MnO, 3.3% for Cl, 4.6% for F, 9.3% for NiO, and 1.9% for Cr_2O_3 at these concentrations. No appropriate secondary standards were measured for SrO and BaO.

LA-ICP-MS

The majority of laser ablation - inductively coupled - plasma mass spectrometry (LA-ICP-MS) analyses was performed at KU Leuven using an Agilent 8900 triple quadrupole ICP-MS coupled to an Analyte Excite excimer laser system equipped with an Ar-Ne 193 nm laser. Helium was used as the carrier gas between the sample chamber and ICP-MS system and a Th/ThO check was performed prior to analysis. Standard operating parameters used a fluence of 2.7 J/cm^2 , a repetition rate of 8 Hz, and a spot size of 85 μm . Cr-spinel measurements were instead performed with a fluence of 3.5 J/cm^2 and standard spot size of 35 μm . Olivine

measurements were performed with a fluence of 7.0 J/cm² and spot size of 110 μm. All analyses were preceded by a pre-rastering at a fluence of 4.0 J/cm² for olivine and 1.0 J/cm² for all other phases.

Analyses were performed in spot-mode by default, but line analyses were performed for olivine (30 seconds) and melilite crystals (20–30 seconds measurement depending on size). Pre- and post-measurement backgrounds were set to 30–45 seconds for all analyses. The NIST-612 reference standard was used for drift correction. A selection of LA-ICP-MS analyses were performed at Utrecht University using a ThermoFisher Scientific Element 2 magnetic sector ICP-MS connected to a Geolas 193 nm excimer laser. Similarly, a selection was measured at the ALIPP6 facility (Institut des Sciences de la Terre de Paris; Sorbonne Université) using an Analyte G2 UV excimer laser ablation system (wavelength of 193 nm) connected to an Agilent 8800 ICP-MS/MS. A full overview of measurement locations is supplied in Electronic appendix 2, whereas an overview of the analyses themselves is given in Electronic appendix 1 Table S3. Operating conditions in Utrecht and ALIPP6 were identical to those performed at the KU Leuven, though a spot size of 60 μm was used at Utrecht University and a fluence of 2.48 J/cm² was used at the ALIPP6 facility. Raw data was processed using GLITTER (Utrecht) and SILLS (Guillong *et al.*, 2008) software, using the LOD calculations by (Longerich *et al.*, 1996), as well as an in-house spreadsheet (Sorbonne).

External standardizations and signal stability evaluations were performed using BCR-2G and/or KL2-G glasses (Jochum *et al.*, 2006) and glass from the 2016 spatter cone (Minissale *et al.*, 2019; sample Ny17-007), respectively. Such measurements indicate relative errors <10% and <15% for >1 μg/g and <1 μg/g concentrations, respectively, and a relative precision of ~5–7%. Transition metals Ni and Cu report higher relative errors of <20%, whereas Zn measurements are subject to relative errors of up to 50%. Secondary standardization of olivine trace element measurements was performed using the MongOl Sh11–2 international reference standard (Batanova *et al.*, 2019), indicating relative errors of <10% for minor element and transition metals, with the exceptions of Cu (<150%) and Zn (<30%). Relative errors of particularly incompatible elements (<0.1 μg/g; Sr, Y, Zr, HREE) are generally <20%, with an average of 15%. No reference values are available for LREE and MREE in olivine.

All data was filtered for sub-detection limit measurements as well as potential influence of inclusionary phases. For internal standardization we used EMPA derived values for ²⁷Al (nepheline, leucite, melilite, phlogopite), ⁴³Ca (clinopyroxene, glass, perovskite), ²⁹Si (olivine), or ²⁵Mg (Cr-spinel).

RESULTS

Petrography

Our sample collection can be petrographically divided into eight main groups based on their dominant mineralogy, and into 17 groups when including textural divisions (Table 1). For the rest of the manuscript, the first five groups will be referred to as ‘evolved’ samples, whereas the last two (barring ‘Others’) will be referred to as ‘primitive’. The ‘Others’ category contains samples from both groups that are phenocryst-free.

In the descriptions below phenocrysts are defined as crystals with a long axis of >250 μm which are significantly larger (at least 2x) than the surrounding matrix grains. Megacrysts are defined as crystals with a long axis of >1 cm. Matrix grain sizes are split into crypto- (≤ 50 μm), micro- (≤ 250 μm), and macro-crystalline (>250 μm, usually >500 μm grain size).

Evolved lithologies

Leucitites

Leucitites are a major lithology at Nyiragongo and are found primarily in phyrlic dykes and lavas between platforms P1 and P2. This lithology is characterized by glomeroporphyritic leucite crystals which range in size from mm- (subgroup ‘glomeroporphyritic’) to cm-scale (subgroup ‘massive’). The glomeroporphyritic subgroup has a micro- to macro-crystalline matrix containing primarily clinopyroxene and nepheline, followed in abundance by oxides, leucite, apatite, and olivine (Table 2), whereas the massive subgroup has a microcrystalline matrix richer in olivine and poorer in nepheline (Table 2). The more primitive matrix of the latter group is also reflected by other isolated phenocrysts (Table 3) as well as the minor minerals included in the cores of leucite-dominated megacrysts (Fig. 3a). Centimetre-sized megacrysts host a core rich in olivine and sector zoned clinopyroxene inclusions, whereas mm-sized glomerocrysts varieties are more commonly rich in nepheline and clinopyroxene. In both groups, leucite phenocrysts are euhedral and frequently host oxide rims tracing former euhedral crystal shapes. Isolated phenocrysts of olivine are typically anhedral, whereas all other phenocrysts are typically subhedral. Minor amounts of secondary minerals are observed (1–5%), primarily concentrated around vesicles (baryte, calcite). It is notable that leucitites with mm-sized glomerocrysts and a macrocrystalline matrix may include clinopyroxene with an aegirine-rich rim.

Nephelinites

The nephelinite group is dominated by highly phyrlic samples primarily derived from the main cone. This group can be subdivided into a porphyritic subgroup, a glomeroporphyritic subgroup, and a last subgroup which we call ‘exsolved’ because this group of samples contains nepheline- kalsilite exsolution features (see below). The porphyritic variant of nephelinites is a matrix-rich, vesicle-poor (Table 3) subgroup with few mm-sized subhedral to euhedral phenocrysts of nepheline and sector zoned clinopyroxene in a commonly cryptocrystalline matrix. The bulk of this subtype is derived from the cliff between P1 and the summit of the main crater. Samples from the glomeroporphyritic subgroup are derived from the dykes in the main crater and overflow material surrounding the cone (Fig. 3b) and include nepheline-dominated glomerocrysts (Table 3) with abundant clinopyroxene in glomerocryst cores (Fig. 3b). The matrix of this subgroup is microcrystalline and evolved in composition (Table 2). Phenocrysts are several mm in size and are subhedral (clinopyroxene) to euhedral (feldspathoids). The final subtype of ‘exsolved’ nephelinites is primarily derived from the pre-1977 lava flow sequence preserved inside the main crater. It includes eight porphyritic samples dominated by subhedral nepheline-rimmed kalsilite crystals which show exsolution lamellae of nepheline, as described in detail by Sahama (1960) (Fig. 4b). The matrix of these samples is cryptocrystalline and distinct from the other nephelinite subgroups (Table 2).

Melilitites

The melilitite group encompasses most of the recent flow material from Nyiragongo, including the majority of lavas from the 2002 eruption, the 2016 spatter cone in the crater, and the 2021 eruption products. Closely related to these specific eruptive episodes and their eruptive centres, melilitites are subdivided into a matrix dominated subgroup (2002 lavas), a glassy porphyritic subgroup (2016 cone; Fig. 3c), and a third,

Table 1: Overview of the lithological groups and associated characteristics as based on petrographic study

Main group	Subgroup	Samples	Rep. sections	Matrix size	Phenocryst size	Habit	Zoning-features
Leucitites	Glomeroporphyritic-	21	5	Macro	Mm-size leucite	Euhedral leucite, subhedral cpx	Sector zoning cpx
	Massive-	4	1	Micro	Cm-size	Euhedral leucite, sub-anhedral ol/cpx	Sector zoning cpx
Nephelinites	Exsolved-	8	1	Crypto to micro	500-1000 um	Subhedral	Sector zoning cpx
	Glomeroporphyritic-	20	3	Micro	Mm-size nepheline	Subhedral to euhedral	Sector and oscillatory zoning in cpx
	Porphyritic-	9	2	Crypto	Mm-size nepheline	Subhedral to euhedral	Core-rim and sector zoning cpx
Melilitites	2016-type porphyritic-	13	2	Crypto/glass	up to 1500 μm , cpx <500	Euhedral except cpx - Anhedral to sub	Core-rim and sector zoning cpx
	2021-type porphyritic-	31	1	Crypto to micro	up to 1500 μm	Subhedral to euhedral	Core-rim and sector zoning cpx
Pyroxene-nephelinites	Matrix-dominated-	55	5	Crypto to micro	<500 μm	Subhedral	-
	Aphanitic-	22	4	Micro	-	-	-
Altered Melilitites	Massive-	3	2	Macro	Mm-size nepheline/Cpx	Subhedral	Core-rim zoning
	Matrix dominated-	26	3	Crypto to micro	500-1000 μm	Subhedral to euhedral	Sector and core-rim
	Altered Melilitites	17	5	Macro	up to 1500 μm	Subhedral	Core-rim melilite zoning
Olivine Basalts	Picritic Melilite Basalts	9	1	Crypto or micro (depends on melilite)	Mm-size olivine. <500 μm melilite	Anhedral to subhedral, euhedral ol, subhedral melilite	Core-rim zoning
Olivine-Melilite Basalts	13	1	Crypto	Mm-size olivine and cpx	Anhedral to euhedral	Core-rim zoning in ol, sector and core-rim zoning in cpx	
Olivine-Cpx Basalts	4	1	Crypto to micro	Mm-size olivine and cpx	Anhedral to subhedral	Core-rim zoning in ol, sector and core-rim zoning in cpx	
Micro-olivine basalt	4	1	Crypto	<500 micron	Sub- to euhedral	Multiple zoning in ol, rim and oscillatory zoning in cpx	
Picrites	Picrites	12	1	Crypto	Mm-size olivine and cpx	Anhedral to euhedral	-
Others	Glassy	10	3				
	Cryptocrystalline	8	1				

Table 2: Point counting results for representative matrices associated with each lithological group based on volume%. Groups with non-porphyritic textures or glassy matrices are noted as '-'. A range is reported if multiple sections were analysed

Main group	Subgroup	Clinopyroxene(%)	Olivine(%)	Nepheline(%)	Melilite(%)	Oxide(%)	Leucite(%)	Apatite(%)	Perovskite(%)	Biotite(%)
Leucitites	Glomeroporphyritic-	52.81	0.30	26.61	0.00	12.06	5.84	2.38	0.00	0.00
Nephelinites	Massive-	32.68	2.93	42.86	0.00	4.31	15.27	1.95	0.00	0.00
	Exsolved-	21.56	1.23	43.33	15.40	8.62	8.62	1.23	0.00	0.00
Melilitites	Glomeroporphyritic-	28.83	0.00	15.13	15.13	28.22	11.86	0.83	0.00	0.00
	Porphyritic- 2016-type	39.3-45.4	0-2.3	30.0-31.2	0	5.4-7.4	16.6-21.8	1.4-2.0	0.00	0.00
Matrix-dominated-	porphyritic- 2021-type	17.15	5.44	24.69	24.48	7.53	20.29	0.42	0.00	0.00
	porphyritic- 29.8-30.8	0	22.4-33.0	10.6-31.8	2.8-6.4	9.4-16.0	2.8-4.3	0	0	0
Pyroxene-nephelinites	Aphanitic-	14.0-14.6	6.1-8.0	32.1-35.4	16.3-16.5	6.3-9.2	16.5-18.5	2.5-2.6	0-0.2	0-1.1
Altered Melilitites	Massive-	-	-	-	-	-	-	-	-	-
	Matrix dominated-	-	-	-	-	-	-	-	-	-
Olivine Basalts	Altered Melilitites	-	-	-	-	-	-	-	-	-
	Picritic Melilite	21.7-22.8	1.8-3.1	21.1-29.2	40.2-43.4	5.8-11.0	0	0	0	0
Basalts	Olivine-Melilite	30.3-37.3	0-2.2	21.7-30.7	11.8-23.8	5.2-9.0	4.4-18.6	0-3.2	0	0
	Basalts	56.89	0.64	23.16	0.43	10.25	8.54	0.11	0.00	0.00
Picrites	Olivine-Cpx	69.56	0.00	11.63	0.00	6.77	12.05	0.00	0.00	0.00
	Micro-olivine	61.9-64.9	10.5-11.1	15.6-16.6	0	2.7-4.3	4.8-7.7	0	0	0
Others	basalt	-	-	-	-	-	-	-	-	-
	Glassy	-	-	-	-	-	-	-	-	-
Cryptocrystalline	Cryptocrystalline	-	-	-	-	-	-	-	-	-
	talline	-	-	-	-	-	-	-	-	-

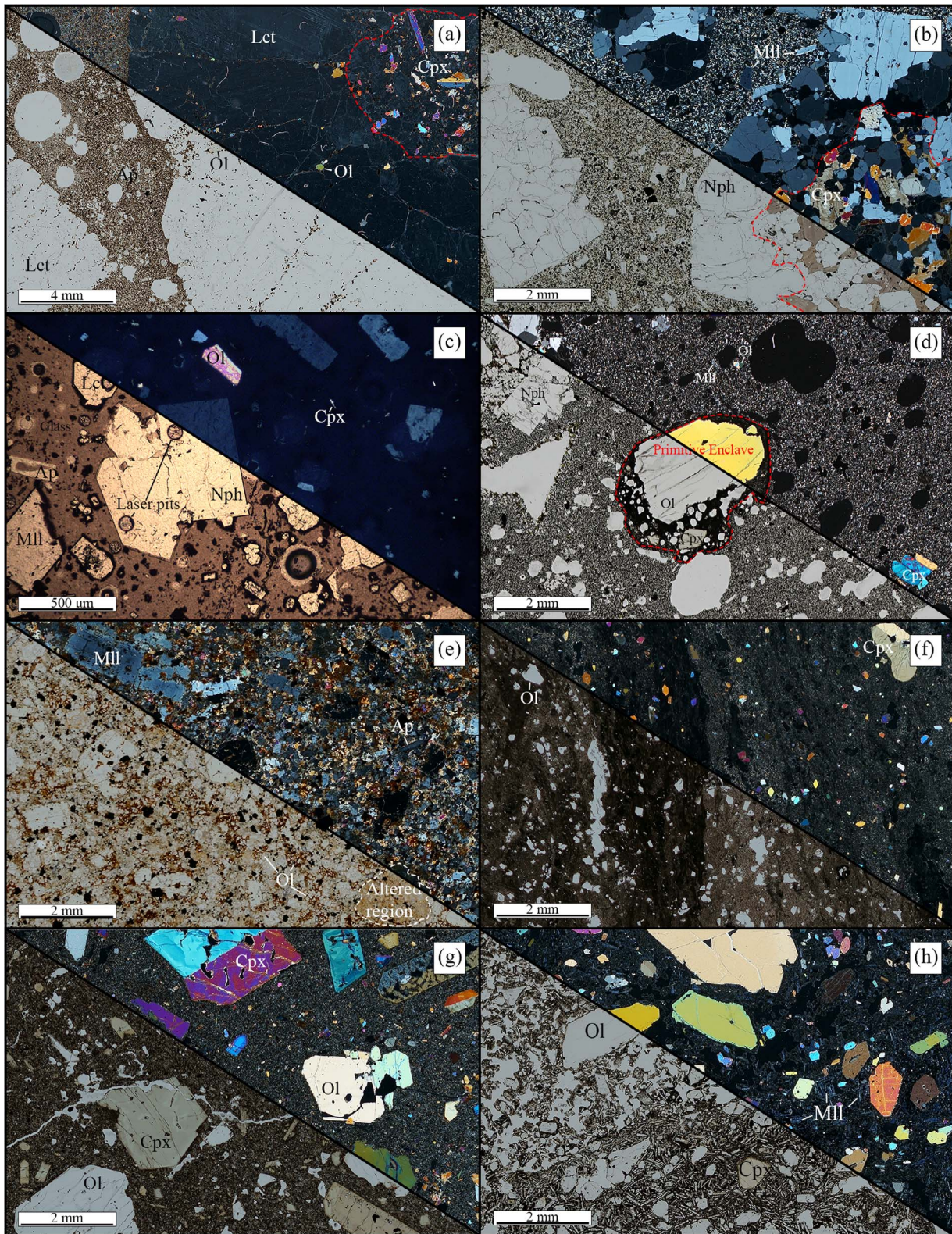


Fig. 3. Photomicrographs of the main lithologies at Nyiragongo, including (bottom left) plane- and (top right) cross-polarized views. Samples follow explanation in the text, starting with (a) massive leucitite Ny17-067 displaying a cm-sized leucite glomerocrysts with multi-mineralogical core and (b) glomeroporphyritic nephelinite Ny17-123. Panels (c) and (d) display 2016 and 2021 porphyritic melilitite samples (Ny17-007 and Ny21-028), respectively, with the latter displaying a primitive enclave at its centre. (e) Altered melilitite Ny17-054, including an altered glomerocrysts region and abundant olivine. Images (f), (g), and (h) represent primitive micro-olivine basalt (Ny17-217), olivine-cpx-basalt (Ny17-209), and picritic melilitite basalt (Ny17-164), respectively. Abbreviations are as follows: Lct: leucite, Nph: nepheline, Mll: melilitite, Cpx: clinopyroxene, Ol: olivine, Ap: apatite.

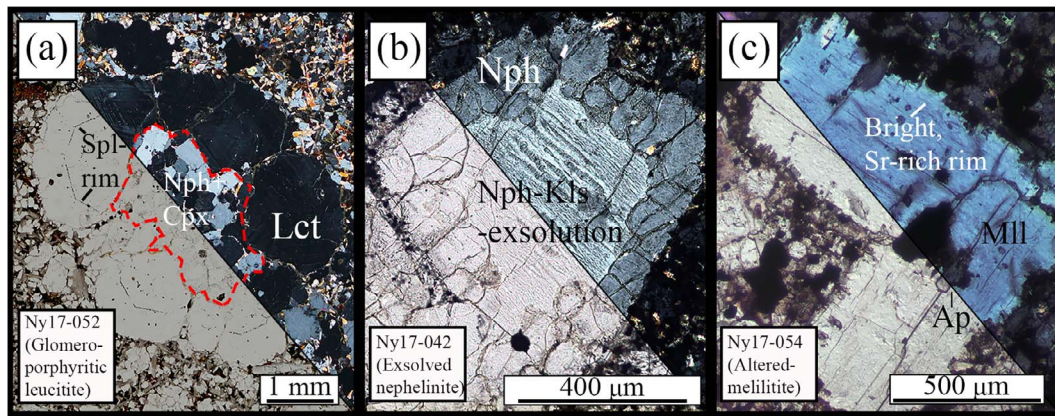


Fig. 4. Key feldspathoid textures as described in the text. (a) Leucite glomerocrysts surrounding a multi-mineralic core (dashed line). Spinel-rims are highlighted, displaying multi-stage growth. (b) Nepheline-kalsilite exsolution textures in an exsolved nephelinite, surrounded by a rim of blocky nepheline. (c) Rectangular melilite crystals with a bright, Sr-rich rim as found in altered melilitites.

(glomero-)porphyritic subgroup which primarily comprises lavas from the 2021 eruption (Fig. 3d). The matrix-dominated melilitites have a crypto- to microcrystalline matrix and only include <500 μm subhedral phenocrysts, of which the abundance decreases with distance from the eruptive fissure (in case of the 2002 flow).

The porphyritic samples from 2016 are almost exclusively glassy and vesicle-rich (Table 3), with diverse phenocryst contents (Table 3) that are dominated by melilite and nepheline. Crystals are euhedral and range up to approximately 1500 μm in size except for primarily <500 μm sized clinopyroxene, some of which are anhedral to subhedral. Few cryptocrystalline varieties which have had more time to cool notably have an increased abundance of clinopyroxene crystals, all of which present core-rim zoning. Glomerocrysts or crystal clusters composed of feldspathoids (primarily nepheline and leucite) and clinopyroxene are commonly encountered in these samples.

Samples from the 2021 lava flows form a third, (glomero-)porphyritic subgroup. These samples were taken primarily from the top of the lava flows, and are, therefore, especially rich in nepheline-glomerocrysts, as a result of floatation. The 2021 lavas vary from highly matrix-dominated (crypto- to microcrystalline) to more porphyritic (Table 3), with subhedral to euhedral crystals up to 1500 μm in size. This is partially associated with a trend from the bottom (crystal-poor) to top (crystal rich) of the flow. Compared to the 2016 lavas, their phenocryst content is significantly richer in clinopyroxene (Table 3). Unique to this flow are mm-sized enclaves of more primitive materials rich in anhedral olivine and unzoned clinopyroxene (Fig. 3d).

Altered melilitites

Altered melilitites comprise an unusual variety of rocks found primarily as blocks or bombs within the cliff-faces of the main cone (Fig. 1c). This lithology is highly crystalline, dominated by subhedral melilite phenocrysts of up to 1500 μm in a macrocrystalline matrix within which most crystals are anhedral, except for abundant apatite (Table 3). Alteration and recrystallization of these samples is evidenced by matrix calcite, abundant rim embayments, yellow staining of melilite crystals (Fig. 3e), and the presence of perovskite, phlogopite, and kirschsteinite-monticellite series olivine (see below; Table 3). In addition, rounded regions of strongly yellow-stained feldspathoids reminiscent of glomerocrysts make up a significant part of the total volume (noted as matrix in Table 3).

Pyroxene-nephelinites

Pyroxene-nephelinites are the most diverse and extensive group of lithologies, having been collected from all parts of the Nyiragongo lava plain (Electronic appendix 1 Table S1, Fig. 1d). The group is subdivided into aphanitic, matrix-dominated, and massive subgroups. The aphanitic and matrix-dominated samples are derived from the main cone, whereas the massive pyroxene-nephelinites are primarily represented by parasitic cone lavas and pre-1977 lava flows. Aphanitic pyroxene-nephelinites are microcrystalline rocks rich in subhedral feldspathoids and clinopyroxene (Table 3) and essentially represent a variety of matrix-dominated samples without any phenocrysts. The matrix-dominated subgroup constitutes porphyritic rocks which make up many flows on the southern lava fields as well as some main cone samples. This lithology has a crypto- to microcrystalline matrix (Table 2) in which subhedral to euhedral <1000 μm phenocrysts of primarily clinopyroxene are embedded (Table 3). The massive subgroup of this lithology contains rocks more closely related to glomeroporphyritic leucitites and nephelinites, but dominated by large clinopyroxene phenocrysts. Their matrix is macrocrystalline and phenocrysts (primarily leucite and clinopyroxene; Table 3) range up to several mm in size.

Primitive lithologies

Olivine basalts

Vents from both the Rushayo chain and Mudjoga-Bushwaga group erupt a variety of olivine-rich lithologies, forming the olivine basalt group. This group can be subdivided into four subgroups based on the presence of melilite and abundance of clinopyroxene, forming the picritic melilite basalt- (melilite rich, clinopyroxene poor) and olivine-melilite basalt- (melilite rich, clinopyroxene rich) subgroups, as well as the olivine-clinopyroxene basalt- (melilite-poor, clinopyroxene rich) and micro-olivine basalt (melilite poor, clinopyroxene poor) subgroups.

The two melilite bearing subgroups are both derived from the Rushayo chain cones, with the picritic melilite basalts coming from Kaboro, Kagundu, and Nyabusa, and the olivine-melilite basalts having been sampled from the Mbatu, Kashaka, Lac Vert, and Rushayo cones (Fig. 1d). The picritic subgroup contains the most crystal-rich olivine basalts, dominated by anhedral to euhedral mm-sized olivine phenocrysts, scarce subhedral to euhedral clinopyroxene, and ≤ 500 μm euhedral melilite laths embedded in a cryptocrystalline matrix (Table 2, 3; Fig. 3h). Melilite phenocrysts show flow-banding textures and may have

Table 3: Point counting results for phenocrysts, vesicles, and matrix associated with each lithological group based on volume%. A range is reported if multiple sections were analysed

Main group	Subgroup	Clinopyroxene(%)	Olivine(%)	Nepheline(%)	Melilite(%)	Oxide(%)	Leucite(%)	Apatite(%)	Perovskite(%)	Biotite(%)	Vesicles(%)	Matrix(%)
Leucitites	Glomeroporphyritic-Massive-	2.5-45.3	0-1.9	0.5-61.4	0-1.4	0.3-6.9	31.4-76.2	0.2-3.4	0	0	1.4-18.2	34.6-62.5
		2.0	2.7	0.0	0.8	3.7	90.5	0.4	0	0	12.7	26.0
Nephelinites	Exsolved-Glomeroporphyritic-	0	0.6	84	5.7	6.9	0.6	2.3	0	0	16.6	65.9
		0-13.5	0	68.4-94.0	0-5.6	0-28	3.4-28.0	0.8-3.2	0	0	3.3-42.6	34.9-79.1
Melilitites	Porphyritic-	0-16.1	0	47.4-74.2	0-18.4	4.8-26.6	0	4.8-7.6	0	0	5.3-11.3	75.6-89.4
	2016-type porphyritic-	7.2-31.5	0-8.8	22.7-26.2	19.5-28.2	7.4-17.2	12.2-13.1	2.3-3.9	0	0	34.0-34.6	36.8-54.0
i-tites	2021-type porphyritic-	10.1-35.9	0.9-5.4	7.6-45.3	11.8-28.3	0.9-14.1	0	2.7-14.1	0	0	11.5-20.1	70.1-85.9
	Matrix-dominated-	7-9.9	1.2	8.6-12.8	43.2-44.6	0-23.5	4.9-26.8	7.5-8.6	0	0	13.1-34.0	62.0-87.0
Pyroxene-nephelinites	Aphanitic-Massive-	26.2-37.6	1.1-2.8	15.3-32.2	6.0-24.2	13.4-15.6	5.3-9.8	4.4-6.0	0	0	19.4-22.6	-
		29.1-39.8	0.8-1.0	32.4-56.0	0	6.6-10.0	10.9-24.4	3.1-5.8	0	0	9.5-9.6	-
Altered Melilitites	Matrix dominated-Picritic Melilitites	63.8-82.5	2.2-6.7	0-6.2	0-4.7	11.4-19.7	0-6.6	3.1-4.7	0	0	11.0-31.6	62.2-81.4
		0.2-51.3	0-12.6	2.6-22.4	12.5-43.5	7.5-10.0	0-0.8	1.8-6.2	0.8-3.1	0-2.3	-	10.3-27.0
Olivine Basalts	Picritic Melilitite Basalts	2.1-9.1	66.7-97.9	0	0-25.8	0.7-2.8	0	0-0.4	0	0	5.2-21.2	49.4-60.0
	Olivine-Melilitite Basalts	28.5-62.9	37.0-62.9	0	0-32.4	0-2.3	0	0	0	0	0.2-14.5	62.2-84.1
Micro-olivine basalt	Olivine-Cpx Basalts	57.9-92.3	5.7-40.8	0	0	1.0-6.7	0	0	0	0	5.5-13.8	67.3-74.5
		12.4-28.3	56.8-83.4	0	0	7.0-15.0	0	0	0	0	7.7-14.8	81.2-87.8
Picrites	Micro-olivine basalt	0-1.8	96.5-99.5	0	0	0.5-1.9	0	0	0	0	3.6-33.9	32.3-51.2
	Picrites	-	-	-	-	-	-	-	-	-	-	-
Others	Glassy	-	-	-	-	-	-	-	-	-	-	-
	Cryptocrystalline	-	-	-	-	-	-	-	-	-	-	-

partially resorbed cores. It is noted that, while alteration is minimal, these rocks commonly exhibit areas of higher crystal density and reduced vesicularity (Fig. 3h). Olivine-melilitite basalts are dominated by mm-sized anhedral to euhedral olivine and clinopyroxene phenocrysts, the latter of which frequently present sector, core-rim, and spongy zoning (see below) (Fig. 3g). Melilitite is limited to the cryptocrystalline matrix (Table 2). Anhedral olivine is additionally found as chadacrysts in clinopyroxene crystals. The melilitite lacking subgroups are derived from the eastern parasitic cones, with olivine-clinopyroxene basalts having been sampled from Mudjoga and Buhuma and the micro-olivine basalts being derived from the lava flows south of Mugara (Fig. 1d). Olivine-clinopyroxene basalts are a subgroup dominated by clinopyroxene, often showing resorption textures as well as sector- and spongy zoning features. Crystals of anhedral to subhedral olivine and clinopyroxene are both mm-sized, and are embedded in a crypto- to microcrystalline matrix devoid of melilitite. Samples from the micro-olivine basalt subgroup are instead dominated by $\leq 500 \mu\text{m}$ subhedral to euhedral, sometimes dendritic olivine, with only minor subhedral clinopyroxene phenocrysts (Fig. 3f; Table 3). The matrix of these samples is cryptocrystalline and dominated by clinopyroxene (Table 2).

Picrites

The Muja cone located SSW of the main cone is the only location where true picrites have been found at Nyiragongo (Fig. 1d). Similar to the picritic melilitite basalts mentioned above, these samples contain an abundance of anhedral to euhedral mm-sized olivine embedded in a clinopyroxene-dominated cryptocrystalline matrix (Table 2). Melilitite is absent from these samples, with minor clinopyroxene and Cr-spinel representing the only other phenocrysts (Table 3). In some cases, quartz xenocrysts can be found in the picrites.

Others

Some samples in the collection are devoid of crystals and will therefore not be discussed other than for bulk chemical analysis.

Xenoliths

Silicic xenoliths

Fused quartz-rich xenoliths are found intermittently in the lavas of Nyiragongo and have been collected from the 2002 (Ny17-131) and 2021-flows (Ny21-013, Ny21-033). Similar blocks have been previously described at Nyiragongo (Sahama, 1973, 1978) and consistently present a green molten glassy contact with their host-rock. Such fragments are almost entirely made up of massive quartz, sometimes with clinopyroxene grains present within cracked veins.

Mineral textures and chemistry

Leucite

Leucite forms primarily subhedral to euhedral trapezohedrons, characterized in thin section by their distinct twinning (Fig. 3a, 4a). Individual leucite crystals can grow up to 4 cm in size (Fig. 2b; Fig. 3a) and represent the main glomerocryst phase in Nyiragongo. Inclusions in leucite phenocrysts are dominated by spinel and apatite, the former of which follows (former) crystal contours, indicating multi-stage growth (Fig. 4a).

Compositionally, leucite is consistently pure KAlSi_2O_6 , with very little change between lithologies. Trace elements of significant concentrations are limited to, in order of descending concentration, Na, Ba, Rb, Sr, and Cs (Fig. 5a; Table 4), all of which substitute for K. Sodium incorporation appears most prevalent in crystals from porphyritic melilitites and massive leucitites

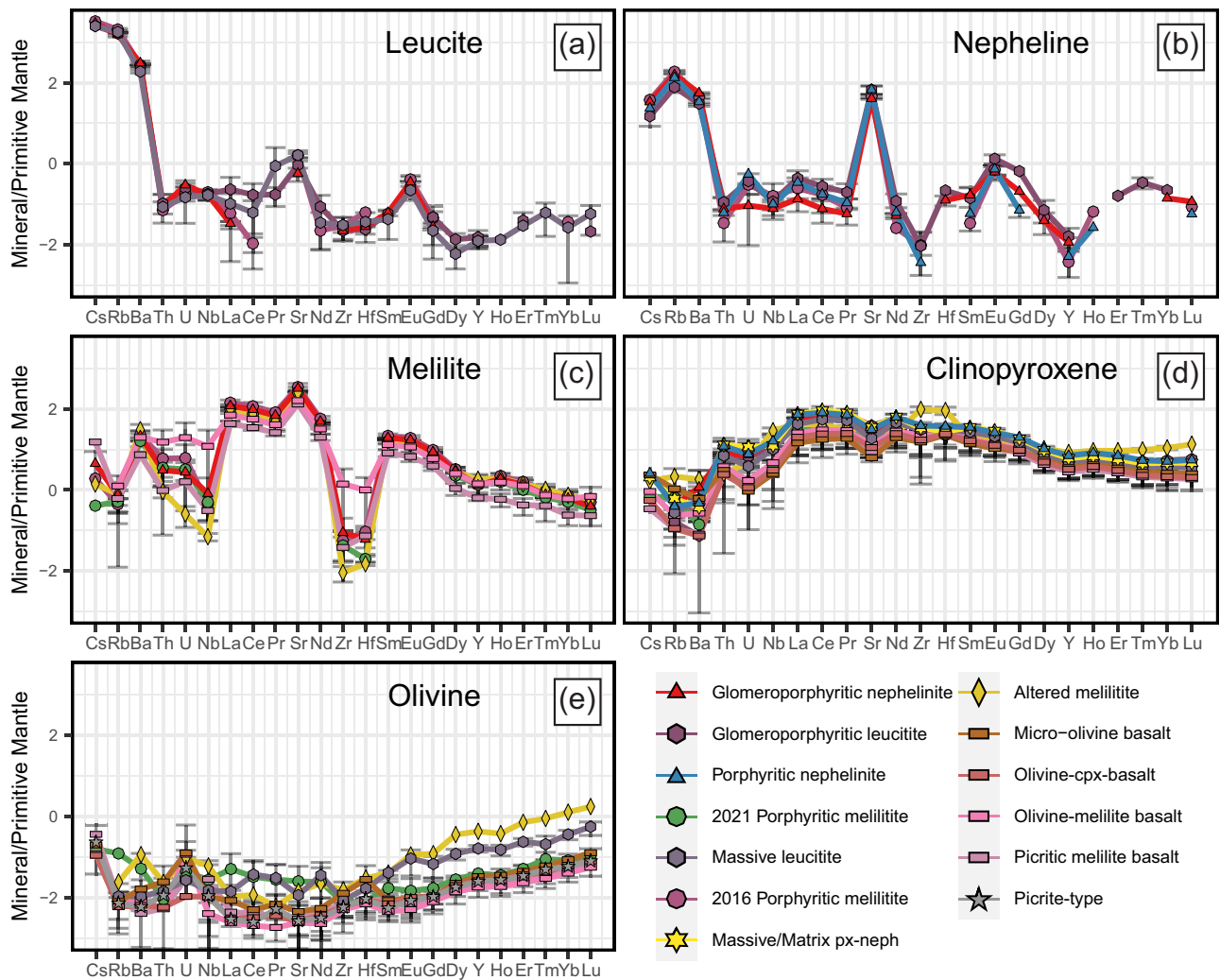


Fig. 5. Primitive-mantle normalized (Sun & McDonough, 1989) multi-element variation diagrams for the major rock-forming minerals at Nyiragongo. Concentrations are expressed in log₁₀ units and represent the mean value of multiple analyses from a single lithological subgroup. Error bars represent one standard deviation (1σ) error based on multiple measurements. Lower errors are excluded in case sub-zero values were obtained.

(1946–4792 $\mu\text{g/g}$), in which concentrations correlate negatively with K. Crystals in more nepheline-dominated lithologies contain less Na (368–1127 $\mu\text{g/g}$) and more K. Weaker negative correlations with K are also observed for Rb (800–1426 $\mu\text{g/g}$) and Sr (2–62 $\mu\text{g/g}$). For Ba (1111–2438 $\mu\text{g/g}$) and to a lesser extent Cs (14–30 $\mu\text{g/g}$), the relationship with K-incorporation is reversed, with a higher degree of incorporation in crystals rich in K. Rare earth element concentrations in leucite are negligible – only just above the detection limit up to Gd. LREE decrease in concentration from La (0.02–0.34 $\mu\text{g/g}$; $[\text{La}]_n = 0.03\text{--}0.50$ where n represents normalization to the primitive mantle composition of Sun & McDonough (1989) to Sm (0.006–0.039 $\mu\text{g/g}$; $[\text{Sm}]_n = 0.01\text{--}0.09$), beyond which a significant Eu-anomaly $[\text{Eu}^* = [\text{Eu}]_n / ([\text{Sm}]_n * [\text{Gd}]_n)^{0.5} = 5.0\text{--}13.6]$ is observed (Fig. 5a).

Nepheline

Nepheline is a primary glomerocryst-forming mineral characterised by rectangular or hexagonal cross-sections in thin section. This phase is poor in inclusions but may occasionally include spinel and apatite.

Compositionally, nepheline ranges from $\text{Na}_3\text{K}_{0.55}\text{Ca}_{0.22}\text{Al}_4\text{Si}_4\text{O}_{16}$ to $\text{Na}_{2.2}\text{K}_{1.6}\text{Ca}_{0.1}\text{Al}_4\text{Si}_4\text{O}_{16}$. The compositions richer in K are found in the most recent eruptive material of the 2016- and 2021

melilitic samples, whereas the Na-rich compositions are found in (glomero-) porphyritic nephelinites from the main crater walls. Trace element contents are primarily limited to mono- (Rb [28–139 $\mu\text{g/g}$], Cs [0.06–0.48 $\mu\text{g/g}$]) and divalent (Sr [792–2043 $\mu\text{g/g}$], Ba [197–410 $\mu\text{g/g}$]) cations (Fig. 5b). Mono-valent traces scale positively with K content and negatively with Na, whereas bivalent traces present an opposite trend following Ca. Only the lanthanides up to Gd are measured at above-detection limit concentrations, decreasing from La (0.036–0.71 $\mu\text{g/g}$; $[\text{La}]_n = 0.05\text{--}1.03$) to Sm (0.015–0.1 $\mu\text{g/g}$; $[\text{Sm}]_n = 0.03\text{--}0.23$), followed by a significant europium anomaly $[\text{Eu}^* \approx 7.5]$ (Fig. 5b).

Melilite

Melilite crystals are characterized by their commonly euhedral, lath-like, or tabular habit (Fig. 3b, c, e, h, 4c). All crystals show a bright rim in cross-polarized light (XPL) (Fig. 3b, c, h, 4c), indicative of normal zoning. Melilite crystals remain relatively small and do not form glomerocrysts. Altered melilitites and porphyritic melilitites from the 2016 lavas contain the largest crystals ($\leq 1500 \mu\text{m}$; Fig. 3e), followed by other feldspathoid-dominated lithologies (e.g. Fig. 3b) and lastly the picritic melilite-basalts which contain $\leq 500 \mu\text{m}$ laths (Fig. 3h). Spinel and apatite grains are common inclusions in melilite, especially in evolved rocks (Fig. 3c, 4c).

Table 4: Representative (average) compositions of minerals in the primitive and evolved lithologies as used in the modelling approach. Minerals hosted by altered melilitites were excluded from the selection

Stage	Picritic			Primitive			Evolved								
	Olivine	Spinel		Olivine	Spinel		Olivine	Melilite	Spinel	Clinopyroxene	Melilite	Spinel	Nepheline	Leucite	Apatite
SiO ₂	40.40	0.02		39.87	46.81		37.42	47.66	0.08	43.31	0.08	41.23	54.76	0.66	
TiO ₂	0.02	2.28		0.01	2.60		0.06	2.72	17.49	0.05	17.49	0.05	0.16	0.01	
Al ₂ O ₃	0.05	21.73		0.04	7.03		0.04	6.30	6.07	6.08	6.07	34.35	23.39	0.00	
Fe ₂ O ₃	10.44	22.63		13.52	5.90		21.66	7.04	66.31	4.01	66.31	0.64	0.28	0.12	
MnO	0.18	0.11		0.23	0.08		0.78	0.15	0.80	0.10	0.80	0.00	0.00	0.01	
MgO	48.34	15.04		45.43	13.12		37.64	12.43	5.84	8.21	5.84	0.13	0.01	0.09	
CaO	0.24	0.02		0.49	23.59		1.49	23.57	0.05	34.02	0.05	1.12	0.01	54.37	
Na ₂ O	0.00	0.00		0.00	0.30		0.02	0.40	0.01	3.14	0.01	13.87	0.25	0.05	
K ₂ O	0.00	0.00		0.00	0.01		0.02	0.02	0.01	0.18	0.01	8.94	21.10	0.02	
P ₂ O ₅	0.01	0.00		0.00	0.00		0.06	0.00	0.00	0.22	0.00	0.00	0.00	41.02	
Cr ₂ O ₃	0.05	36.91		0.02	0.00		0.00	0.00	0.00	0.00	0.00	0.00	0.00	0.00	
NiO	0.23	0.00		0.16	0.00		0.00	0.00	0.00	0.00	0.00	0.00	0.00	0.00	
V	5.17	-		5.20	91.42		4.09	53.46	5.27	0.30	5.27	0.49	0.40	6.46	
Cr	4.27	-		4.29	236.19		5.76	333.90	3259.73	7.02	3259.73	0.57	0.94	741.97	
Co	308.01	-		304.78	2046.66		14.21	343.29	30.34	1.07	30.34	2.11	1.32	298.98	
Ni	152.35	-		152.79	29.55		189.60	35.18	233.26	43.78	233.26	0.74	0.01	5.93	
Cu	1818.11	-		1811.15	150.49		693.95	68.12	161.16	7.20	161.16	0.03	0.08	71.03	
Zn	3.85	-		3.92	1.77		1.67	1.04	0.00	0.76	0.00	0.30	0.36	0.00	
Rb	75.65	-		75.86	19.31		132.74	31.51	426.14	281.09	426.14	5.83	1.04	495.05	
Sr	0.00	-		0.00	0.04		0.01	0.25	0.09	0.37	0.09	89.86	1135.07	62.73	
Y	0.06	-		0.08	240.60		0.26	581.19	0.88	6551.09	0.88	1157.15	27.43	5996.44	
Zr	0.10	-		0.10	14.70		0.75	26.00	0.24	6.98	0.24	0.03	0.04	207.43	
Nb	0.07	-		0.07	216.91		0.08	435.95	109.68	0.52	109.68	0.06	0.24	73.82	
Cs	0.01	-		0.01	2.69		0.01	9.55	86.86	0.30	86.86	0.06	0.12	28.24	
Ba	0.00	-		0.00	0.00		0.00	0.00	0.01	0.00	0.01	0.21	21.81	1.23	
La	0.04	-		0.06	1.59		0.19	4.16	0.82	165.84	0.82	285.02	1679.35	2282.87	
Ce	0.00	-		0.00	15.12		0.01	38.02	0.14	84.09	0.14	0.20	0.04	9165.81	
Pr	0.01	-		0.01	46.81		0.06	111.75	0.44	173.56	0.44	0.31	0.08	25556.36	
Nd	0.00	-		0.00	7.17		0.01	15.36	0.09	19.10	0.09	0.02	0.03	2798.24	
Sm	0.00	-		0.01	34.68		0.04	64.41	0.21	66.68	0.21	0.06	0.03	9933.85	
Eu	0.00	-		0.00	7.38		0.01	12.30	0.03	8.55	0.03	0.01	0.01	1295.06	
Gd	0.00	-		0.00	2.11		0.01	3.63	0.03	2.82	0.03	0.14	0.03	401.82	
Tb	0.01	-		0.01	5.81		0.03	9.24	0.00	5.12	0.00	0.02	0.01	820.12	
Dy	0.00	-		0.00	0.02		0.00	0.45	0.01	0.27	0.01	0.00	0.00	85.08	
Ho	0.01	-		0.01	3.61		0.09	6.20	0.07	2.17	0.07	0.01	0.00	466.53	
Er	0.00	-		0.00	0.61		0.02	1.08	0.02	0.33	0.02	0.00	0.00	70.40	
Tm	0.01	-		0.01	1.45		0.12	2.73	0.05	0.68	0.05	0.00	0.00	131.47	
Yb	0.00	-		0.00	0.17		0.02	0.35	0.01	0.07	0.01	0.00	0.00	14.40	
Lu	0.03	-		0.03	1.09		0.20	2.38	0.06	0.33	0.06	0.00	0.00	57.25	
Hf	0.01	-		0.01	0.16		0.04	0.39	0.01	0.03	0.01	0.00	0.00	7.80	
Ta	0.00	-		0.00	7.57		0.00	11.39	0.00	0.01	0.00	0.00	0.00	3.36	
Pb	0.00	-		0.00	0.71		0.00	1.74	8.54	0.01	8.54	0.00	0.02	8.96	
Th	0.00	-		0.00	0.00		0.00	0.06	0.07	0.41	0.07	0.11	0.05	154.21	
U	0.00	-		0.00	0.27		0.00	0.69	0.01	0.33	0.01	0.00	0.00	203.91	
	0.00	-		0.00	0.03		0.00	0.13	0.10	0.07	0.10	0.00	0.00	103.17	

All melilite crystals are alumo-åkermanitic in composition, ranging from an empirical formula of $\text{Na}_{0.25}\text{Ca}_{1.75}(\text{Al}_{0.25}\text{Mg}_{0.65}\text{Fe}_{0.1})\text{Al}_{0.05}\text{Si}_{1.95}\text{O}_7$ in picritic melilite basalts to $\text{Na}_{0.35}\text{Ca}_{1.65}\text{Al}_{0.3}\text{Mg}_{0.55}\text{Fe}_{0.15}\text{Si}_2\text{O}_7$ in altered melilitites. Strontium enters the melilite structure easily as a replacement for Ca, as evidenced by rim compositions in altered melilitites which can include up to 2.4 wt.% SrO (0.07 p.f.u. Sr; Fig. 5c). Strontium incorporation in unaltered crystals ranges from 2000 $\mu\text{g/g}$ in olivine-melilite basalts to $\sim 11\,000$ $\mu\text{g/g}$ in 2016 porphyritic melilitites. Similarly, Ba (40–350 $\mu\text{g/g}$), Mn (300–930 $\mu\text{g/g}$), Co (24–65 $\mu\text{g/g}$), and Zn (85–430 $\mu\text{g/g}$) readily partition into melilite (Fig. 5c). Melilite contains abundant LREE ($\text{La} = 23\text{--}132$ $\mu\text{g/g}$; $[\text{La}]_n = 96.7\text{--}555.6$) dropping off from Nd to Sm ($[\text{La}/\text{Sm}]_n = 4.87\text{--}7.91$, $[\text{Nd}/\text{Sm}]_n = 1.90\text{--}3.77$) (Fig. 5c). LREE concentrations correlate with the host composition from picritic melilite basalts to 2016 porphyritic melilitites. HREE are less affected, with Lu ranging from 0.01 (picritic melilite basalts) to 0.03 $\mu\text{g/g}$ (2016 porphyritic melilitites), generating a significant slope from MREE to HREE ($[\text{Sm}/\text{Lu}]_n = 9.95\text{--}87.3$).

Clinopyroxene

Clinopyroxene crystals are primarily found as either sub-euhedral laths in thin section (Fig. 6f, g, h) or anhedral crystals formed in confined spaces. The anhedral to subhedral laths are a common feature of evolved lithologies, and frequently have normal core-rim zoning features. Larger varieties of sub-euhedral crystals are instead found in the olivine basalt group. These crystals are commonly sector zoned (Fig. 6g), may include complex (though usually normal over long length scales) core-rim zoning (Fig. 6f), and at times present patchy zoning (Fig. 6h) or spongy textures (Fig. 3g). This last feature is limited to olivine basalt group samples. Anhedral crystals are most commonly part of glomerocrysts, and most frequently contain sector zoning features. Inclusions in clinopyroxene are primarily apatite and spinel.

Excluding rare optically-discernible aegirine rims (up to 55% aegirine; Fig. 7a) clinopyroxene form a cluster of 40–84% diopside, 0–55% hedenbergite, and 0–38% desilicated components ($\text{CaTiAl}_2\text{O}_6$ and esseneite ($\text{CaFe}^{3+}\text{AlSiO}_6$)) with less than 5% Na-components (aegirine ($\text{NaFe}^{3+}\text{Si}_2\text{O}_6$) & jadeite ($\text{NaAlSi}_2\text{O}_6$)) (Fig. 7a, b). Fe-speciation for component calculations is determined using the Droop method (Droop, 1987). Increased incorporation of desilicated components is paired primarily with a decrease in diopside, whereas the hedenbergite component is clustered between 5 and 25% and increases in the most Na-rich rims (Fig. 7b). Virtually all zoning features (oscillatory, sector, spongy) are related to replacement of diopside by desilicated components.

Trace elements are abundant in clinopyroxene, with elements either increasing or decreasing in concentration with the degree of chemical evolution in their host rocks. Among the elements decreasing from primitive to evolved samples, Sc and Cr are primarily abundant, ranging in concentration from 13 to 199 $\mu\text{g/g}$ and 0 to 8932 $\mu\text{g/g}$, respectively (Fig. 5d). Crystals in evolved samples frequently have Cr measured below detection limit. In contrast, Sr (97–890 $\mu\text{g/g}$), V (124–484 $\mu\text{g/g}$), Zr (14–625 $\mu\text{g/g}$), and Y (3–39 $\mu\text{g/g}$) increase in concentration from primitive to evolved rocks (Fig. 5c). Rare earth element concentrations in particular increase in line with whole-rock evolution, decreasing from LREE to HREE ($[\text{La}/\text{Lu}]_n = 2.6\text{--}24.9$) and peaking most commonly at Ce ($\text{Ce}_n = 3.8\text{--}121$) (Fig. 5d). In general, the concentration of REE increases with increased incorporation of Na, tetrahedral Al, Ti, and Fe^{3+} due to charge-balancing effects (Hill *et al.*, 2000; Wood & Triguila, 2001;

Sun & Liang, 2012), even if the compositional changes are in-part related to melt evolution.

Olivine

Olivine crystals can be split into categories of fully formed euhedral (Fig. 6a, b, d), rounded (Fig. 6e), and skeletal (Fig. 6c) morphologies, all of which have distinct zoning characteristics most commonly displayed in primitive morphologies. Fully formed euhedral crystals are most common and include normal (Fig. 6d), reverse (Fig. 6b), or multi-stage (Fig. 6a, b) core-rim zoning patterns. Such multi-stage zoning may occur on the scale of a few μm at crystal rims (Fig. 6a) or may extend throughout whole crystals (Fig. 6b). Rounded crystals in primitive lithologies similarly include normal and reverse zoning but additionally often display intense distortion features (Fig. 6e). Dendritic olivine is exclusively reverse-zoned. It is worth noting that olivine phenocrysts in picrites present no zoning features, and that zoning is scarce in the picritic melilitites. Olivine crystals commonly include chromite in olivine basalts and picrites, and apatite in evolved samples.

Olivine-dominated lithologies from the parasitic cones contain olivine with a range of forsterite ($\text{Fo} = 100 * \text{Mg}/(\text{Mg} + \text{Fe}^{2+})$) contents from 80 (olivine melilite basalts, micro-olivine basalts) to 92 (olivine basalts and picrites) (Fig. 7c, d). Despite significant variations in core compositions, the rims of these crystals are highly compositionally restricted to between Fo 83 and 87 (Fig. 7d). The most evolved samples host olivine spanning in forsterite content from 55 (glomeroporphyritic leucitites/nephelinites) to 77 (melilitites, massive leucitites, pyroxene-nephelinites), excluding extremely Fe-rich ($\text{Fo} < 30$) rims. Nyiragongo olivine is particularly rich in calcium (200–14 000 $\mu\text{g/g}$ Ca), scaling with decreasing forsterite content (Fig. 7c). Similarly, Mn concentrations decrease with forsterite forming an evolved (4400–13 000 $\mu\text{g/g}$) and primitive (1100–3000 $\mu\text{g/g}$) cluster. Olivine in altered melilitites can be divided between forsterite-fayalite crystals ($\text{Fo} = 77\text{--}86$) and crystals of kirschsteinite-monticellite compositions ($\text{CaMg}_{0.5\text{--}0.55}\text{Fe}_{0.45\text{--}0.5}\text{SiO}_4$).

Ni contents in olivine range from approximately 200 (massive leucitites) to 2900 $\mu\text{g/g}$ (picritic melilite basalts). A similar trend is observed for Cr, which is at near-detection limit concentrations (< 3 $\mu\text{g/g}$) for evolved samples but ranges from 20 to 1100 $\mu\text{g/g}$ for primitive samples. High inclusion density in olivine from highly evolved samples (e.g. 2016 porphyritic melilitites) impeded accurate REE determinations (Fig. 6a), but comparatively inclusion-free crystals (of near-identical major element composition to those in the 2016 lavas) included in massive leucitites report ~ 0.01 $\mu\text{g/g}$ La and ~ 0.04 $\mu\text{g/g}$ Lu. Primitive olivine is significantly poorer in these trace elements, ranging from La (median 0.0014 ± 0.009 $\mu\text{g/g}$) to Lu (0.005 ± 0.002 $\mu\text{g/g}$). Trace element contents of Ca-dominated olivine are not distinctly different from Mg-Fe dominated crystals.

Accessory phases Spinel and chromite

Fe-Ti-rich spinel is observed in all described lithologies, found as inclusions, phenocrysts, or part of glomerocrysts, and is most frequently euhedral. The Fe-Ti-rich variety will be referred to as 'spinel', whereas Cr-spinel will be referred to as 'chromite'. Exsolution features are common in these crystals, especially those contained within glomerocrysts. These crystals follow the general empirical formula $(\text{Fe}^{2+}, \text{Mg}^{2+})(\text{Fe}^{2+}, \text{Fe}^{3+}, \text{Al}^{3+}, \text{Cr}^{3+}, \text{Ti}^{4+})_2\text{O}_4$, primarily incorporating, in order of descending abundance, ulvöspinel (34–88%), magnetite (13–43%), magnesio-ferrite

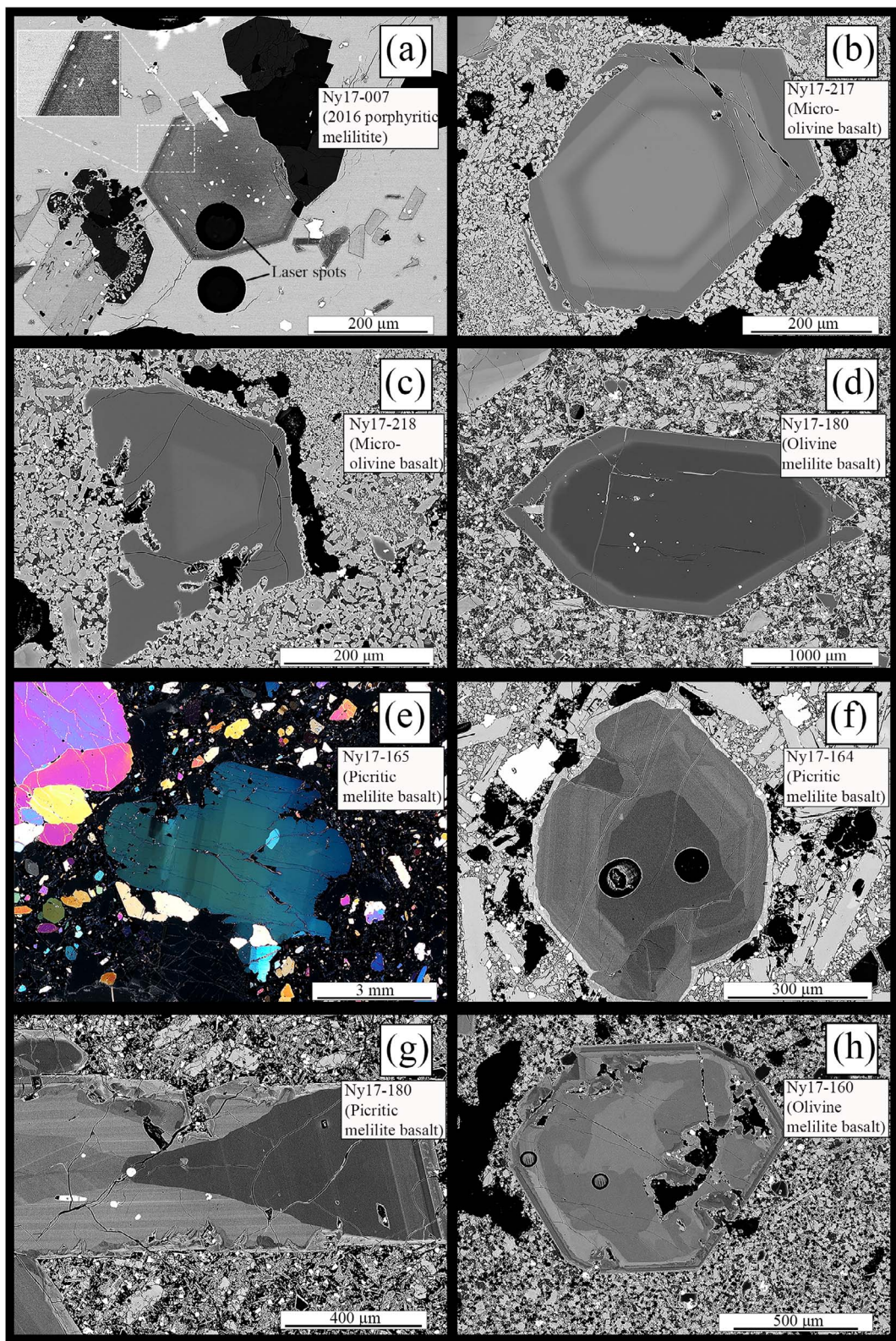


Fig. 6. Key features of (a-e) olivine and (f-h) clinopyroxene, as described in the text. (a) Oscillatory zoning in the rim of euhedral olivine from the 2016 porphyritic melilitite. (b) Multi-stage zoning throughout an olivine crystal from a micro-olivine basalt, showing four distinct zones. (c) Reverse zoning in a dendritic olivine from a micro-olivine basalt. (d) Euhedral olivine in an olivine melilitite basalt showing a lightly rounded core with a distinctly light rim, surrounded by an intermediate, euhedral rim. (e) Distortion features in a rounded olivine crystal from a picritic melilitite basalt, as recognized by zoned extinction. (f) Complex clinopyroxene zoning combining a core structure with oscillatory zoning towards the rim. (g) Hourglass sector zoning in clinopyroxene combined with oscillatory zoning from core to rim. (h) Patchy zoning in clinopyroxene combined with oscillatory zoning features at the outer rim.

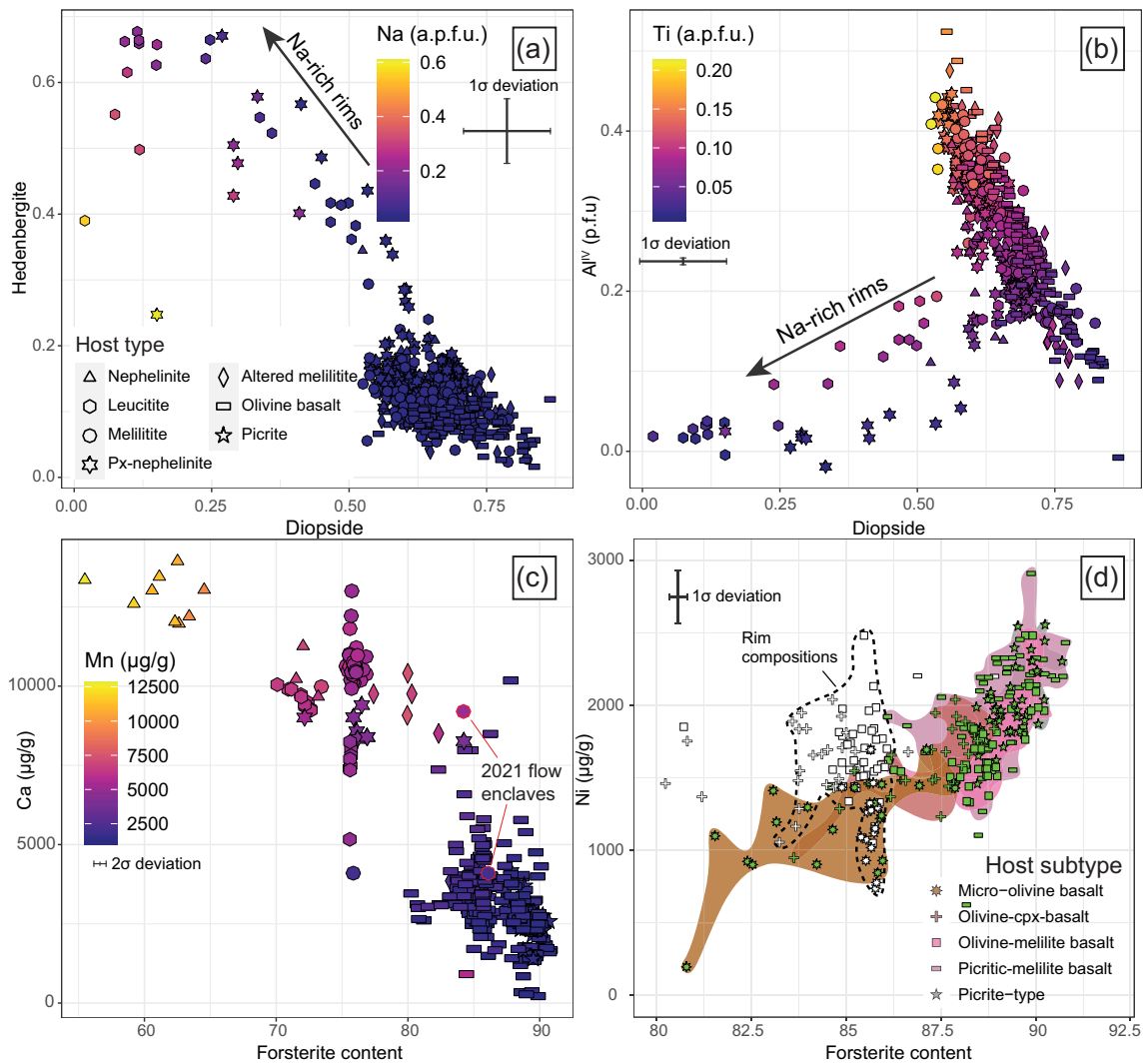


Fig. 7. Major and minor element compositions of (a-b) clinopyroxene and (c-d) olivine. Clinopyroxene components are expressed as fraction of all calculated components. (a) Hedenbergite vs diopside and (b) tetrahedral Al (Al^{IV}) vs diopside relationships in clinopyroxene display the correlation between Mg-incorporation and presence of Ti-rich desilicated components. Na-incorporation can be observed to decrease with increased abundance of desilicated components due to complications in charge balancing. The (c) Ca vs forsterite relationships in olivine display the abundance of Ca in Nyiragongo olivine and stark contrast in trace element contents between olivine in primitive and evolved hosts. (d) shows the relationship between Ni and forsterite in olivine, with open symbols representing rims and filled symbols representing cores. Fields for each host-subtype are included for better visibility among the scatter of point-data. 1 σ or 2 σ standard deviations are reported based on secondary standard measurements, see Electronic appendix 1.

(1–33%), and spinel (*sensu stricto*) (1–18%). Fe²⁺/Fe³⁺ ratios were calculated by iteratively matching to an AB₂O₄ structure. Spinel found in altered melilitites is noticeably more magnetite-rich than spinel populations found in other samples, which form a solid solution between Mg- and Ti-rich compositions with a relatively constant magnetite component (15–25%). Spinel contains high concentrations of transition metals, among which vanadium is most abundant (3159–3413 µg/g), followed by Zn (404–481 µg/g), Co (189–278 µg/g), Ni (111–221 µg/g), Zr (96–122 µg/g), Nb (83–90 µg/g), Cr (25–44 µg/g), Ta (7.4–9.3 µg/g), Sc (5.1–5.6 µg/g), and Hf (1.9–2.4). REE are significantly less abundant, all of which are measured at <1 µg/g (LREE) to <0.1 µg/g (HREE) concentrations.

Chromite is primarily an inclusion phase found in the primitive lithologies. These crystals are euhedral and most commonly sub-200 µm in size, but may range up to 500 µm in picrites. In these samples, phenocrysts of chromite also occur in the matrix. Chromite crystals found in primitive lithologies span a compositional range from chromite-rich (~50% chromite, 35% spinel, 15%

magnetite+magnesioferrite) to chromite-poor (~20% chromite, 68% spinel, 12% magnetite+magnesioferrite).

Apatite

Though apatite is primarily found as inclusions, it is also abundantly found as phenocrysts of a few hundred microns in elongation (Table 3). Though the majority of apatite crystals is inclusion free, crystals in the altered melilitites are consistently littered with primary inclusions of melt and fluid, following concentric patterns, reflecting multi-stage growth.

Apatite compositions are approximately identical among samples, following an empirical formula of Ca₅(PO₄)₃(F_{0.66-1},Cl_{0.012-0.023},OH_{0-0.3}). Note that OH-groups were not measured directly but were instead inferred from stoichiometry. Calcium replacement by Sr is minor (up to 0.06 Sr p.f.u.), but it is evident that apatite is a major Sr carrier besides melilite, including 3053 to 9476 µg/g in the measured crystals.

Perovskite and phlogopite

Perovskite and phlogopite are exclusively observed in the altered melilitites. Perovskite crystals form euhedral crystals of up to approximately 100 μm in diameter. These crystals may be zoned from core to rim. Phlogopite is less abundant, but easily recognised within these altered samples due to its clear cleavage and irregular crystal shape. Phlogopite can host a variety of inclusions (apatite, nepheline, spinel most commonly). Compositions of these phases can be found in Electronic appendix 1 Table S2 and S3.

Glasses

Glass compositions can be divided into matrix glasses from the 2016 spatter cone melilitites ($\text{Mg\#} = 35\text{--}36$, $(\text{Na} + \text{K})/\text{Al} \approx 1$, similar to the whole-rock and lava lake), highly evolved interstitial green glasses filling vesicles in pyroxene-nephelinites ($\text{Mg\#} = 2\text{--}5$, $(\text{Na} + \text{K})/\text{Al} = 6\text{--}16$) as previously described by Andersen *et al.* (2012, 2014), and scarce melt inclusions found in picritic melilite basalt olivines ($\text{Mg\#} = 53\text{--}70$, at variable degrees of recrystallization). An overview of these compositions is presented in Electronic appendix 1 Tables S2 and S3.

Whole-rock geochemistry

Major element geochemistry

Our sample collection covers a significant chemical domain, overlapping virtually all previously published data on Nyiragongo (Fig. 8, 9; Barette *et al.*, 2017). Our samples plot over a limited SiO_2 range (35.9–47.6 wt.%), the majority of which plot in the domain of foidites, with the exception of some of the melilite-deficient olivine basalts (Fig. 8). Al_2O_3 increases continuously as MgO (i.e. considered as a differentiation index) decreases, with an inflection point at approximately 12.5 wt.% Al_2O_3 and 5 wt.% MgO (Fig. 9a), changing to a steeper slope. Within this slope from 5.0 to 1.5 wt.% MgO, Al_2O_3 increases from 14.5 to 23.1 wt.% from pyroxene-nephelinites and melilitites to nephelinites and leucitites. Both K_2O (0.7–9.5 wt.%) and Na_2O (1.0–8.4 wt.%) increase as MgO drops throughout the dataset (Fig. 9d, e), clustering at the compositions of pyroxene-nephelinites and melilitites from which leucitites and nephelinites split off to high K_2O and Na_2O concentrations, respectively (Fig. 8, Fig. 9d, e). Their high concentrations generate an agpaite index of 0.20 to 1.34. In contrast, Fe_2O_3 , TiO_2 , CaO , MnO , and P_2O_5 follow kinked trends with MgO, increasing from picrites to altered melilitites following a path that moves away from primitive olivine compositions (Fig. 9b, c, f). At the 5 wt.% MgO inflexion point, these oxides decrease in concentration, moving towards nepheline and leucite compositions. P_2O_5 concentrations are consistently high (>1 wt.%), though the feldspathoid-poor olivine basalts are noticeably displaced to lower concentrations (0.75–1.03 wt.%).

Trace elements

The evolution of trace element concentrations with differentiation follows patterns comparable to major elements, with two trends split by the altered melilite subgroup. Rare earth element concentrations increase from picrites to lava lake compositions (matrix dominated and 2016 porphyritic melilitites, $\text{MgO} = \pm 4$ wt.%) (Fig. 10a), beyond which concentrations drop once more in the nepheline- and leucite-rich lithologies (Fig. 10a). Such a pattern is followed by all trace elements incompatible in all dominant mineral species (e.g. Zr; Fig. 10e). Transition metals concentrated in olivine and clinopyroxene (e.g. Sc, Ni, Cr) instead have maxima at high (≥ 10 wt.%) MgO, either in melilite-deficient

olivine basalts (Sc) or the olivine-dominated picrites (for olivine-enriched elements). At lower MgO contents, concentrations continuously drop with increasing differentiation. Large-ion lithophile elements (LILEs) concentrated in feldspathoids instead form trends increasing with differentiation, diverting at low MgO concentrations depending on the dominant lithology (Fig. 10d).

Trace element patterns of Nyiragongo volcanics are characterized by an overall high concentration compared to primitive mantle concentrations (Sun & McDonough, 1989), with a preference for incompatible trace elements (Fig. 11). Overall enrichment degrees follow major element geochemical trends, increasing from picrites to olivine basalts, into a large, homogenized cluster of all evolved lithologies. Altered melilitites, though richer in Mg than their unaltered counterparts, are among the most enriched lithological groups (Fig. 11b), reflecting their metasomatic nature (Andersen *et al.*, 2012). Negative anomalies are limited to Th, K, Pb, P, Zr, Hf, and Ti in primitive lithologies, whereas more feldspathoid-rich lithologies also present depletions of P, and Y compared to the overall trend. Rare earth element patterns present a smooth downward curve towards HREE, with a significant displacement of LREE to higher values ($[\text{Nd}/\text{Sm}]_n = 1.9\text{--}2.5$), increasing with fractionation (Fig. 10f).

DISCUSSION

Based on the petrography and geochemistry of our new samples we will now discuss evidence for the presence and structure of multiple magmatic reservoirs. We will subsequently provide textural and geochemical evidence for mineral fractionation and accumulation processes active in these reservoirs. These processes will be modelled numerically to reproduce whole-rock geochemical trends at Nyiragongo volcano, and we will provide estimates for the pressure and temperature conditions at which these processes take place using geothermobarometric methods. Lastly, the mantle sources of various lithologies will be briefly discussed.

Textural records of magma chamber processes

Mineral textures at Nyiragongo provide insights into the nature of active reservoirs, the multiplicity of which has been argued for repeatedly, usually referring to two reservoirs at 10–15 km and ± 4 km depth, as well as the crater lake itself within the main edifice (Demant *et al.*, 1994; Platz *et al.*, 2004; Pouclet & Bram, 2021). In our study, multiple reservoirs are best evidenced by the multitude of Fo contents at which olivine crystals have equilibrated (Fig. 7c, d) and the abrupt core-rim transitions showing normal zoning (Fig. 6d) (e.g. Kahl *et al.*, 2011). Resorbed anhedral cores additionally indicate short periods of disequilibrium and dissolution showing that some crystals have either been moved to more evolved melts (Liang, 2003), or that such liquids were moved into their host reservoir. Olivine crystals from the 2016 and 2021 lavas instead show a homogeneous composition but one even more evolved than previously mentioned rim compositions (Fo ~ 76 ; Fig. 7c), indicating at least three magmatic environments for olivine crystallization alone.

Sector zoning and spongy textures in clinopyroxene crystals in the olivine basalts (Fig. 6) indicate disequilibrium conditions in which growth rates exceed that of diffusion. This is triggered by high degrees of reservoir undercooling (Welsch *et al.*, 2016; Ubide *et al.*, 2019), generating sector zoning at low undercooling rates and spongy-textures at higher degrees (Welsch *et al.*, 2016; Ubide *et al.*, 2019). Whereas clinopyroxene in the picritic melilite basalts

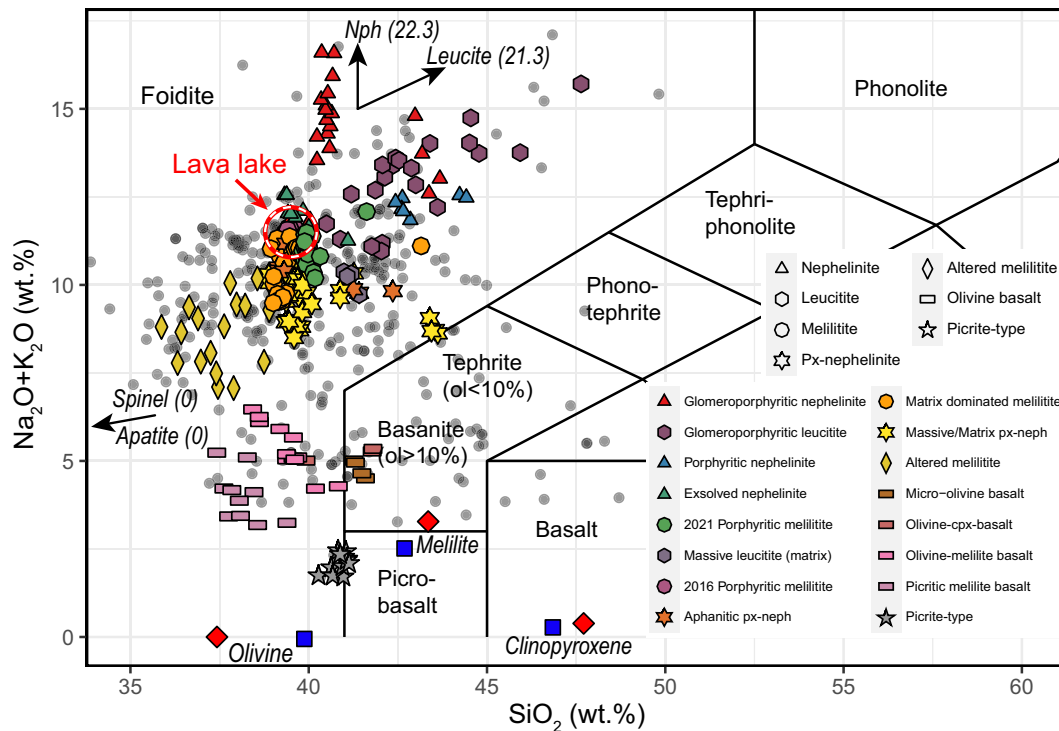


Fig. 8. Total alkali-silica (TAS) diagram of the whole-rock sample collection from Nyiragongo on a volatile-free basis, normalized to 100%, after [Lebass et al. \(1986\)](#). Samples are grouped based on both main- and subgroup, as expressed in shape and colour, respectively. Translucent background data-points represent literature data from Nyiragongo as compiled by [Barette et al. \(2017\)](#), as well as the more recent analyses of [Minissale et al. \(2019, 2022\)](#). Mineral compositions shown as squares and diamonds represent averages of all collected electron microprobe analyses from evolved and primitive lithologies, respectively. Mineral compositions outside of the field of view are indicated with arrows, listing their value on the y-axis in brackets. The lava lake composition is indicated, represented by 2016 vent lavas. Standard deviations on XRF measurements are smaller than symbols and are therefore not included in the figure.

frequently present oscillatory or sector zoning ([Fig. 6f, g](#)), spongy-textures are limited to the less olivine-rich olivine-melilite basalt subgroup, where they are juxtaposed with normal-zoned olivine ([Fig. 3g, Fig. 6h](#)). This indicates a higher degree of clinopyroxene supersaturation in the reservoir represented by these rocks.

Reaching supersaturation is most commonly achieved through 1) delayed nucleation or 2) crystallization in a diffusion field ([Donaldson, 1979; Welsch et al., 2016](#)), both of which can be triggered by mafic recharge, either superheating the reservoir or displacing melts into crustal chambers. We suggest that sector zoning in the picritic melilite basalts can be generated through repeated mafic recharge (potentially contributing to oscillatory zoning patterns), but that the spongy-textures in olivine-melilite basalts are generated when such an event moves liquids to a shallower chamber. Such displacement to colder environments causes mixing and clinopyroxene oversaturation which may be concurrent with rim development of equally displaced olivine crystals. This matches the observation that the high-Mg cores of these crystals are rounded down, reflecting dissolution prior to rim formation ([Liang, 2003](#)).

Complexly-zoned olivine crystals as found in the micro-olivine basalts may be produced similarly through repeated mafic recharge events, but given the minor compositional variation between sectors (2–3 Mg# maximum) and overall small crystal size, we suggest that magma convection may be a more suitable process ([Streck, 2008](#)).

The rheological nature of the reservoirs is perhaps best reflected by the discrepancy in crystal habits between the products of the upper conduit and the parasitic cones. For example, the crystals found in the 2016 lavas indicate that the

formation of euhedral crystals dominates in the upper levels, consistent with growth in liquid dominated reservoirs ([Holness et al., 2019; Barrière et al., 2022](#)), aided by the low viscosity of the liquid itself ([Morrison et al., 2020](#)), which promotes quick diffusion of elements and rapid crystal growth. Crystals suspended in such convecting liquid-rich bodies aggregate through synneusis ([Schwindinger & Anderson, 1989](#)), forming the glomerocrysts abundant in the main crater complex. Even the continuous introduction of hot, gas-charged magma in the upper conduit itself can be petrographically observed through micro-scale oscillatory zoning in olivine of the 2016 eruption materials ([Fig. 6a](#)) reflecting thermal oscillations produced by the pistoning motions described by [Barrière et al. \(2019\)](#). Such features have been previously described for plagioclase at the open-vent system of Erebus ([Moussallam et al., 2015](#)).

Olivine dislocation bands presented in the parasitic cone lithologies are evidence that not all of Nyiragongo's reservoirs are dominated by their liquid components ([Fig. 6e](#)). While [Demant et al. \(1994\)](#) originally interpreted these bands to reflect an origin in mantle peridotite, such features can also be evidence for deformation in crystal-dominated mush-piles, requiring only 3–12 MPa differential stresses ([Holness et al., 2019; Wieser et al., 2020](#)). We believe that the mush hypothesis is more likely for Nyiragongo, given that these crystals host abundant melt and chromite inclusions and have CaO (>0.2 wt.%) and Fo (<90) contents inconsistent with a mantle origin. Picritic melilitites and picrite-type lithologies appear to directly tap into (or accumulate crystals from) these mushes, explaining their comparative lack of normal zoning through rapid transport.

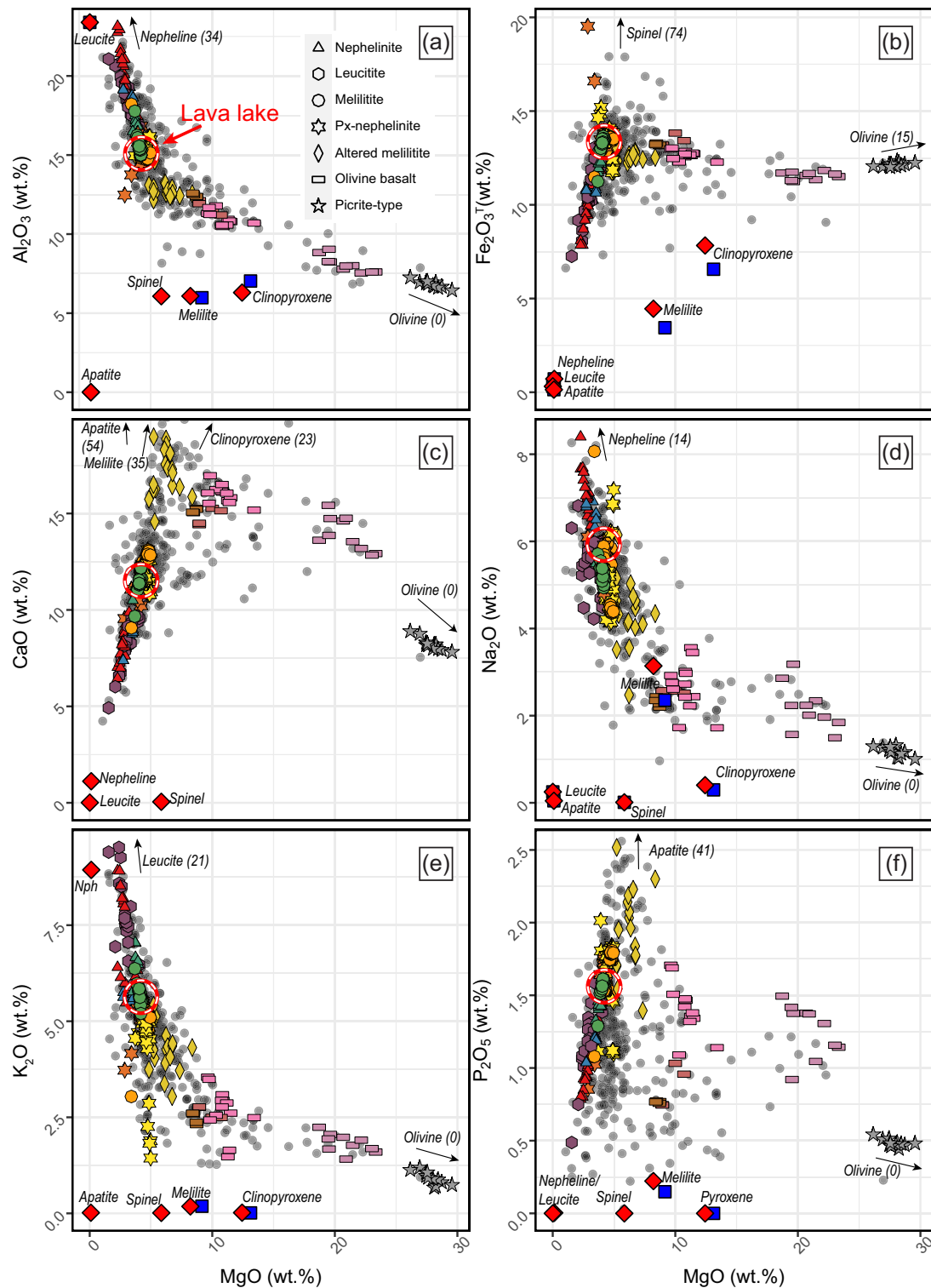


Fig. 9. Harker diagrams of the various lithologies expressed against MgO as a proxy of increasing differentiation. Symbols and colours follow the same legend as Figure 8. Mineral compositions shown as squares and diamonds represent averages of all collected electron microprobe analyses from evolved and primitive lithologies, respectively. Mineral compositions outside of the field of view are indicated with arrows, listing their value on the y-axis in brackets. All concentrations are on a volatile-free basis, normalized to 100%. Fe_2O_3^T indicates that all Fe is expressed as Fe^{3+} . Translucent background data-points represent literature data from Nyiragongo as compiled by Barette et al. (2017), as well as the more recent analyses of Minissale et al. (2019, 2022). The lava lake composition is indicated, represented by 2016 vent lavas. Standard deviations on XRF measurements are smaller than symbols and are therefore not included in the figure.

Thin rims of reverse zoning in these crystals are explained through mafic recharge events which would impact deep chambers and perhaps unlock crystal mushes prior to eruption (Cooper & Kent, 2014; Moore et al., 2014). Based on these observations

we interpret the picritic olivine melilitite basalts and picrites not to represent liquids as a whole, but instead a combination of a primitive melt (matrix) and entrained mush material (olivine phenocrysts), which were erupted quickly after mush

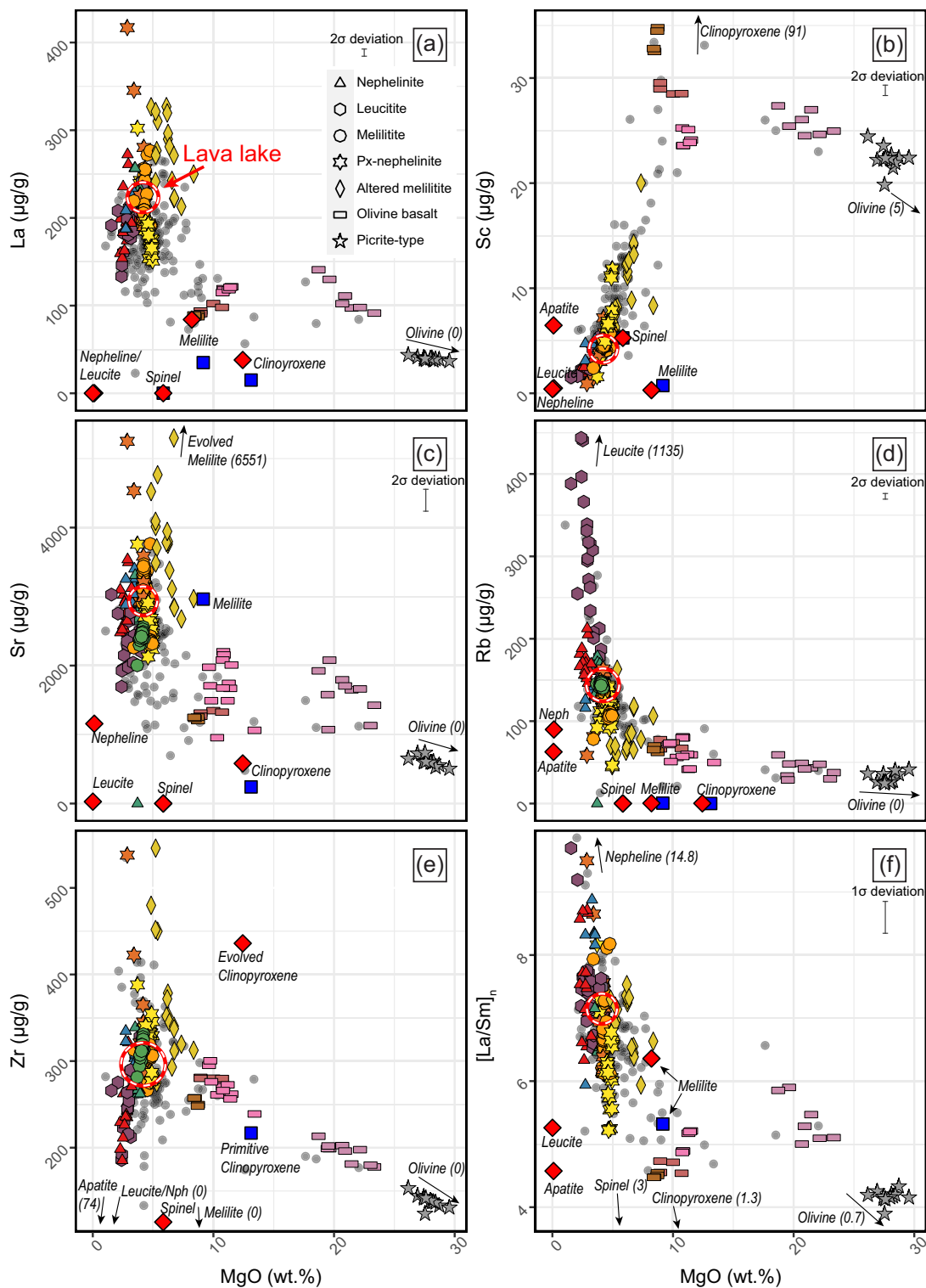


Fig. 10. Trace element concentrations in whole-rocks expressed against MgO as a differentiation proxy. Symbols and colours follow the same legend as Figure 8. Samples collected after 2017 are not displayed for (a), (b), and (f) because these samples have not been analysed by dissolution ICP-MS analysis. The (c) Sr, (d) Rb, and (e) Zr concentrations in these samples are based on XRF analysis. (f) Primitive-mantle normalized (Sun & McDonough, 1989) La/Sm concentrations, representing LREE enrichment. Mineral compositions shown as squares and diamonds represent averages of all collected electron microprobe analyses from evolved and primitive lithologies, respectively. Mineral compositions outside of the field of view are indicated with arrows, listing their value on the y-axis in brackets. Translucent background data-points represent literature data from Nyiragongo as compiled by Barette *et al.* (2017), as well as the more recent analyses of Minissale *et al.* (2019, 2022). The lava lake composition is indicated, represented by 2016 vent lavas. 2σ standard deviations are reported based on ICP-MS secondary standards, see Electronic appendix 1. Standard deviations for MgO and Zr (from XRF) are too small to display.

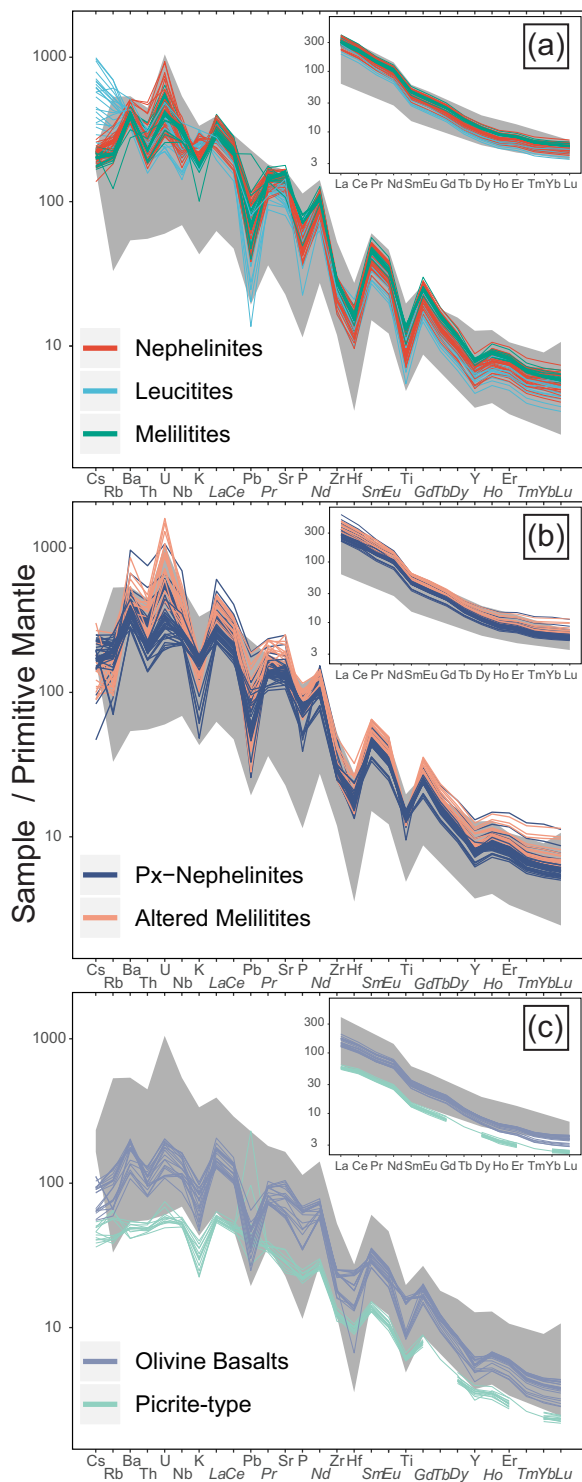


Fig. 11. Primitive-mantle normalized (Sun & McDonough, 1989) multi-element variation diagrams for whole-rock compositions, grouped by primary lithological group. REE patterns are additionally displayed in isolated form, displaying a preference for LREE, increasing with fractionation. The background shaded field represents all literature data from Niyragongo as compiled by Barette *et al.* (2017), as well as the more recent analyses of Minissale *et al.* (2019, 2022).

disaggregation and did not fully re-equilibrate and mix in upper magmatic reservoirs.

Not all reservoirs feeding parasitic cones are mush-dominated, however, as evidenced by the euhedral outer habit of normal-

zoned olivine crystals. Their primitive cores compositionally advocate for initial growth in a similar melt to that of the mush (Fig. 7d). However, their euhedral and normally zoned rims advocate for subsequent movement towards a region containing enough liquid for growth to be interface-controlled (Fig. 6d).

In fact, the rim composition of these normal zones is observed in a large population of olivine crystals, regardless of their core composition (Fig. 7d), which shows that it may represent a relatively stable, homogenized reservoir that shows connectivity with the rest of the plumbing system.

Evidence for fractional crystallization and mineral accumulation processes

Whole-rock and mineral geochemical trends indicate fractional crystallization from high-MgO to low-MgO compositions. Chadacrysts of olivine within clinopyroxene crystals indicate that the former crystallized first, consistent with increasing SiO₂ and CaO and Sc from picritic melilite basalts to olivine-melilite basalts (Fig. 8; Fig. 9c; Fig. 10b). Moreover, chromite inclusions in these olivine crystals indicate chromite crystallization to precede or happen concurrently with olivine. Though less abundant, melilite must hit the liquidus at this point as well, given its co-existence in picritic olivine-melilite basalts (Fig. 3h), matching the olivine + melilite cotectic at low silica-activity determined by Gee & Sack (1988). Significant clinopyroxene crystallization from this point onwards is evidenced by a steep drop in clinopyroxene-compatible Sc (Fig. 10b) (e.g. Beard *et al.*, 2019; Molendijk *et al.*, 2023), as well as its abundance in olivine-clinopyroxene-basalts and olivine-melilite basalts. This reflects a change to higher silica-activity (Gee & Sack, 1988). The next lithology in terms of MgO is that of the pyroxene nephelinites, which evidence the appearance of nepheline on the liquidus. Slower MgO depletion indicates diminished olivine crystallization whereas the steeply decreasing CaO indicates apatite, melilite and clinopyroxene to take its place. Leucite does not yet crystallize here, as evidenced by a sustained K₂O increase. This phase is only later seen encapsulating the earlier crystallizing minerals (Fig. 4a). The lack of decreasing SiO₂ concentrations is evidence for fractional crystallization of spinel and apatite, as is also supported by inclusions. Overall trace element concentrations increase throughout this sequence (Fig. 10; Fig. 11) due to their incompatibility in almost all crystallizing phases (Molendijk *et al.*, 2023), albeit to varying degrees. The composition of the lava lake represents the final melt, phenocryst populations of which are our best approximation of a eutectic assemblage (Table 3), indicating the stability of nepheline, melilite, leucite, spinel, apatite, and olivine, the latter of which is now of significantly more evolved composition (Fig. 7c). Anhedral habits of clinopyroxene in these lavas indicate that its crystallization is mostly limited to more primitive reservoirs, causing dissolution in this evolved melt. Further evolution towards glomeroporphyritic compositions is instead explained through floatation driven accumulation, a feature which has been described by various authors for older lava flows (e.g. Sahama, 1973, 1978; Demant *et al.*, 1994; Platz *et al.*, 2004). This is also clearly seen in lava flows of the main crater (Fig. 2b, d; Fig. 3a, b) as well as the 2021 lava flows (Fig. 2d). We can address this feature quantitatively by combining chemical data and point counting results, showing a clear correlation between leucite and nepheline volume proportions and their corresponding trace element signatures (Cs and Rb in leucite, high Sr/Ba and Rb/Cs ratios in nepheline; Fig. 12a,b). Leucites and nephelinites evolve separately from each other (e.g. Fig. 8), as is reflected in the notable absence of leucite glomerocrysts in

the 2021 lavas, despite clearly accumulating in the main crater (Fig. 2b). This observation is in line with leucite crystallizing at later-stages of magmatic evolution, due to the stability field of leucite. Leucite is not stable above 120 MPa (Platz *et al.*, 2004) and therefore primarily crystallizes in the low-pressure lava lake or shallowest conduits/reservoirs. Since the lava flows of 2021 tapped into significantly deeper material than just the upper conduit (Smittarello *et al.*, 2022), leucite is underrepresented compared to nepheline (2021 lava phenocryst populations contain 7.6–45.4% nepheline but no leucite, the matrix nepheline/leucite ratio is 50 ± 5 ; Table 2, 3), the crystallization of which starts significantly deeper.

Instead, evidence for leucite crystallization is found in the glomeroporphyritic samples in the centre of the crater, of which the geochemistry suggests addition of leucite to a lava-lake composition melt (approximated by the 2016 and 2021 eruptive compositions; Fig. 8, 12b). Texturally we observe leucite crystallization around polymineralic aggregates (Fig. 3a,b; Fig. 4a) that contain olivine in equilibrium with the surrounding matrix material (see below; Fig. 12d). This is indicative of a transition from eutectic crystallization of olivine, clinopyroxene, nepheline, spinel, and apatite to a crystallization and aggregation regime dominated by leucite (and nepheline) in the increasingly more alkali-saturated upper-conduit magmas.

Similarly, accumulation of olivine has been documented by Demant *et al.* (1994) and Platz *et al.* (2004) to explain the occurrence of picritic lithologies, which our data corroborate through correlation of Ni and Cr concentrations with olivine phenocryst abundance in the picritic melilite basalts and true picrites (Fig. 12c). Combined with Mg-Fe exchange equilibrium estimates based on $K_D^{ol-liq} \left(\frac{X_{Fe}^{ol} X_{Mg}^{liq}}{X_{Mg}^{ol} X_{Fe}^{liq}} \right)$ values calculated with the approach of Toplis (2005) (with oxygen fugacity buffered to QFM and Fe^{3+}/Fe^{2+} ratios in melts calculated with the approach of (Kress & Carmichael, 1991)) this leads us to believe that neither of these lithologies represent true melts (Fig. 12d).

In contrast, crystals from the olivine-melilite- and olivine-clinopyroxene-basalts have cores in near-equilibrium with the bulk-rock composition of their hosts and rims in equilibrium with a more evolved melt (Fig. 12d), likely the composition of the surrounding matrix.

Modelling whole-rock variability

Whole-rock geochemical trends at Nyiragongo converge on the lava lake composition (Fig. 8; Fig. 9), indicative of efficient mixing and homogenisation in the upper parts of the volcanic plumbing system, which is consistent with the liquid-dominated, convecting nature of the lava lake and, presumably, upper magma reservoirs (see above) (Barrière *et al.*, 2019), as observed for similar open-systems (Vergnolle & Métrich, 2022 and references therein). Primitive eruption products from parasitic cones are clearly excluded from this homogenization, and instead constitute MgO-rich compositions, in part affected by olivine-accumulation (see above). Platz *et al.* (2004) indicated that the gap between primitive and evolved compositions can be adequately explained through olivine and melilite fractionation, linking the two distinct source reservoirs. This interpretation developed further by Molendijk *et al.* (2023) who indicated that in addition to olivine and melilite, clinopyroxene crystallization is also required to explain trace element systematics across this compositional gap. Regardless, incorporation of high-Fo olivine crystals into the 2021 lavas that are far from being in equilibrium with their surrounding melts (Fig. 3d; Fig. 7c) suggest that primitive and evolved reservoirs are connected.

Connectivity between reservoirs indicates that a single fractional crystallization model should be able to explain the lithological diversity of Nyiragongo. To this end, we applied the same step-wise Rayleigh fractionation method as Molendijk *et al.* (2023) to our newly acquired dataset, using the following equation for major elements:

$$C_i = (C_0 - 0.01 * C_f) / F$$

and the following equation for trace elements:

$$C_i = C_0 * F^{(D-1)}$$

in which C_i , C_0 , and C_f are the bulk concentrations of a given oxide/element in the fractionated liquid, starting liquid, and fractionating crystal assemblage, respectively. F represents the fraction of melt over crystal, set to 0.99 at each step and D represents the combined partition coefficient of a given element for the crystallizing assemblage. For partition coefficients we use the data of Molendijk *et al.* (2023) but for major element compositions we use mean mineral compositions measured in evolved and primitive lithologies (Table 4). Crustal contamination by assimilation of basement material has been repeatedly ruled out (Bell & Powell, 1969; Sahama, 1978; Chakrabarti *et al.*, 2009a), and will therefore not be included in the model. Our investigation of olivine accumulation indicates that the most likely parental melt feeding Nyiragongo was either a micro-olivine basalt, an olivine-cpx basalt, or an olivine-melilite basalt. Of these, we suggest that an olivine-melilite basalt is the most likely parental melt, because micro-olivine basalts and olivine-clinopyroxene basalts frequently diverge in terms of major geochemical trends, presenting lower P_2O_5 , higher SiO_2 , and higher Sc than the main array (Fig. 8; Fig. 9f; Fig. 10b). In addition, they have an insufficiently high Mg# to have crystallised the cores of olivine crystals found in olivine-melilite basalts (Mg# of 64–74 required, assuming a K_D of 0.22–0.30; Fig. 12d). Moreover, this is in agreement with reports of compositionally similar olivine-melilite basalts erupted from the nearby Mugogo eruptive centre (Fig. 1b), which were interpreted as primary melts (Verhaeghe, 1958; Condomines *et al.*, 2015).

Contrary to Molendijk *et al.* (2023) who used mineral modes determined by least-squares fit Monte-Carlo simulations, we used our point-counting data as our closest approximation of a fractionation assemblage, the results of which are listed in Table 5. We chose Ny17–160 (Mg# = 62.5; Electronic appendix 1 Table S1) as our starting composition because it is a relatively MgO-poor olivine-melilite basalt (decreasing the likelihood of accumulation; MgO = 10.8 wt.%) for which point-counting, mineral, and trace element data is available. Based on the phenocryst-content of picritic samples as well as rhyolite-MELTS-simulations (Gualda *et al.*, 2012), the first crystallizing assemblage was set to the point-counting results of sample Ny17–165 with clinopyroxene replaced by chromite (67% olivine, 26% melilite, 7% chromite; Table 5), which is the first crystallizing phase and is required to explain Cr_2O_3 systematics (Fig. 12c). For this step we use olivine and spinel compositions from picritic samples only (Picritic melilite basalts and picrites; Table 5). While our general whole-rock trend could be explained through two-step fractionation (see Results), this initial step is required to explain the short window of increasing CaO within the olivine-melilite basalt subgroup. The olivine that crystallizes in this step is represented by high-Fo olivine cores found in olivine-melilite basalt samples, equilibrated with the starting melt composition (Fig. 7d; 12d). Fractionation of this assemblage was sustained until the liquid reached an Mg# in equilibrium with

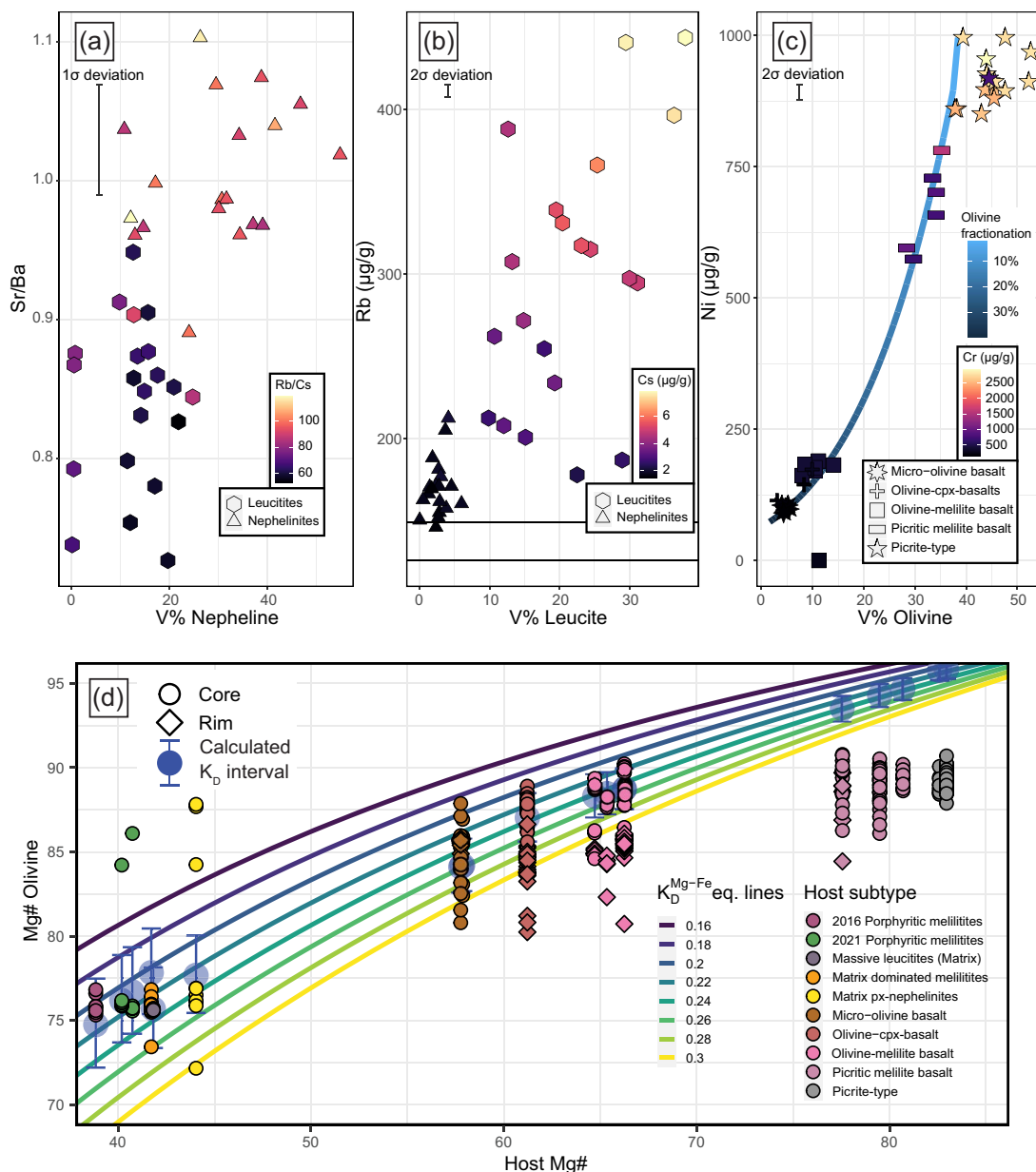


Fig. 12. Geochemical indications of accumulation processes active at Nyiragongo. Floatation-driven accumulation of (a) leucite and (b) nepheline in the lava lake can be traced with increases of Rb and Sr/Ba, respectively, whereas (c) olivine (+ chromite) accumulation in the lower plumbing system generates excess Ni. The horizontal lines in (a) represent the groundmass composition of massive leucites. Pure removal of olivine from a picritic source is simulated in (c). Equilibrium between olivine and host is modelled in (d), using the model by Toplis (2005) under QFM conditions. Shaded regions and associated error bars indicate equilibrium intervals for the respective host-rock. Standard deviations are included based on ICP-MS secondary standards, see Electronic appendix 1.

the rims of these crystals ($Mg\# = 59.6$; Fig. 12d), at a liquid fraction of 96%.

At this point, the crystallizing assemblage was switched to a modified version of the point counting results of Ny17-160 with additional melilitite, nepheline, spinel, and apatite replacing olivine and clinopyroxene (19% olivine, 35% clinopyroxene, 3% nepheline, 33% melilitite, 7.5% spinel, 2.5% apatite; Table 5). These new phases are added because we observe a change in crystallization assemblage in the wide gap of whole-rock compositions spanning from the evolved array ($MgO = 4.9$ wt.%) to the current modelled composition ($MgO = 9.5$). This fractionation step continues until the main evolved array is reached, at a liquid fraction of 58%.

The remaining liquid is expelled to the upper magmatic reservoirs, where fractionation of feldspathoids starts to dominate. For

this stage of crystallization, which continues until the 2021-lava composition is reached, we observe that the matrix proportions of sample Ny17-016, an aphanitic part of an in-crater lava flow, are most well-suited (3% olivine, 26% clinopyroxene, 15% nepheline, 24% melilitite, 10% leucite, 16% spinel, 6% apatite; Table 5). This step continues until 68% of the expelled liquid is remaining, or 39% of the total. Nepheline and leucite accumulation adequately explain any further evolved lithologies, with pure nepheline accumulation producing the glomeroporphyritic nephelinite array, and the roughly 50:50 proportions of Ny17-052 (Table 5) explaining the glomeroporphyritic leucites array.

The MgO-rich picritic melilitite basalts and picrites are adequately explained through 30–40% phenocryst accumulation following the proportions of picritic melilitite basalt Ny17-165 (67%

Table 5: Mineral modes used in each step of the fractionation modelling approach with associated sample name. Names followed by an ‘*’ sign are modified from original proportions, as explained in the text. Liquid compositions before fractionation and after each fractionation/accumulation step are included, as well as a lava lake-representative sample for comparison

Stage	Start	Fractionation			Finish	Accumulation		
Step	Step 0	Step 1	Step 2	Step 3	Lava lake	Pre-fractionation	Post-fractionation	
Sample	<u>Ny17-160</u>	Ny17-165*	Ny17-160*	Ny17-016	<u>Ny17-013</u>	Ny17-132	Ny17-165	Ny17-052
Sample subgroup	<u>Olivine-melilite basalts</u>	Picritic melilite basalts	Olivine-melilite basalts	Aphanitic-pyroxene-nephelinites	<u>2016 Glass</u>	Picrites	Picritic melilite basalts	Glomeroporphyritic leucites
Start liquid fraction (F)	-	100	96	58	-	-	-	-
End liquid fraction (F)	-	96	58	39	-	-	-	-
Olivine(%)	-	67	19	3	-	98	67	0
Clinopyroxene(%)	-	0	35	26	-	0	7	7
Nepheline(%)	-	0	3	15	-	0	0	43
Melilite(%)	-	26	33	24	-	0	26	0
Leucite(%)	-	0	0	10	-	0	0	43
Spinel(%)	-	0	7.5	16	-	0	0	7
Chromite(%)	-	7	0	0	-	2	0	0
Apatite(%)	-	0	2.5	6	-	0	0	0
	Start composition	Resulting liquid compositions						
wt.%								
SiO ₂	<u>38.62</u>	38.64	38.22	39.18	<u>39.32</u>	39.08	39.94	41.26
TiO ₂	<u>3.16</u>	3.32	4.01	4.21	<u>2.78</u>	1.58	1.67	2.69
Al ₂ O ₃	<u>10.55</u>	10.93	14.20	15.21	<u>15.02</u>	5.40	6.39	19.00
Fe ₂ O _{3(T)}	<u>12.85</u>	12.97	13.71	13.03	<u>13.36</u>	12.41	11.00	8.64
MnO	<u>0.22</u>	0.23	0.28	0.30	<u>0.29</u>	0.20	0.17	0.19
MgO	<u>10.82</u>	9.53	4.85	3.91	<u>4.10</u>	29.61	23.24	2.82
CaO	<u>16.21</u>	16.56	13.33	11.53	<u>11.48</u>	8.09	13.60	7.97
Na ₂ O	<u>3.02</u>	3.14	4.34	4.86	<u>5.89</u>	1.48	1.84	5.36
K ₂ O	<u>3.09</u>	3.25	5.14	5.79	<u>5.61</u>	1.51	1.57	8.36
P ₂ O ₅	<u>1.47</u>	1.54	1.85	1.57	<u>1.55</u>	0.73	0.77	0.98
Mg#	<u>62.52</u>	59.27	41.21	37.29	<u>37.81</u>	82.54	80.72	39.29
μg/g								
Sc	<u>23.6</u>	24.5	6.5	1.8	<u>4.2</u>	14.0	18.2	2.5
V	<u>392.3</u>	392.8	314.0	192.4	<u>256.5</u>	201.0	207.4	124.4
Cr	<u>291.2</u>	208.6	6.8	0.1	<u>2.1</u>	2613.2	1307.2	9.7
Co	<u>55.9</u>	52.2	35.3	25.2	<u>39.0</u>	104.1	84.1	16.5
Ni	<u>189.7</u>	137.1	14.5	1.3	<u>22.0</u>	1092.7	770.1	2.4
Zn	<u>82.8</u>	84.5	97.9	91.1	<u>109.6</u>	82.1	85.7	59.4
Rb	<u>81.0</u>	85.2	139.1	138.6	<u>135.3</u>	39.7	40.5	279.4
Sr	<u>2200.3</u>	2261.9	2550.5	2830.1	<u>2922.2</u>	1078.0	1465.9	2023.6
Y	<u>28.3</u>	29.7	38.3	45.2	<u>35.4</u>	13.9	15.0	30.0
Zr	<u>266.6</u>	280.1	308.3	348.5	<u>322.2</u>	130.7	139.3	236.6
Nb	<u>114.5</u>	120.3	193.5	264.2	<u>231.5</u>	56.1	57.3	174.8
Cs	<u>0.7</u>	0.7	1.1	0.9	<u>1.7</u>	0.4	0.4	4.0
Ba	<u>1230.2</u>	1292.9	2117.5	2814.4	<u>2800.9</u>	602.7	621.6	2160.1
La	<u>119.3</u>	125.1	176.6	213.6	<u>220.6</u>	58.4	63.9	140.1
Ce	<u>240.0</u>	251.5	338.1	396.8	<u>412.1</u>	117.6	129.1	260.4
Pr	<u>26.5</u>	27.8	36.0	41.4	<u>42.3</u>	13.0	14.4	27.2
Nd	<u>101.7</u>	106.5	131.0	145.6	<u>144.4</u>	49.8	55.3	95.5
Sm	<u>15.8</u>	16.5	19.5	21.3	<u>20.4</u>	7.7	8.5	14.0
Eu	<u>4.4</u>	4.6	5.4	6.0	<u>5.6</u>	2.1	2.4	4.0
Gd	<u>11.8</u>	12.4	14.3	15.4	<u>13.9</u>	5.8	6.4	10.1
Tb	<u>1.3</u>	1.4	1.7	1.9	<u>1.6</u>	0.7	0.7	1.2
Dy	<u>6.3</u>	6.6	8.2	9.4	<u>7.9</u>	3.1	3.3	6.3
Ho	<u>1.0</u>	1.1	1.4	1.7	<u>1.4</u>	0.5	0.6	1.1
Er	<u>2.7</u>	2.9	3.7	4.4	<u>3.7</u>	1.3	1.4	3.0
Tm	<u>0.3</u>	0.3	0.4	0.6	<u>0.5</u>	0.2	0.2	0.4
Yb	<u>1.9</u>	2.0	2.8	3.4	<u>2.9</u>	1.0	1.0	2.3
Lu	<u>0.3</u>	0.3	0.4	0.5	<u>0.4</u>	0.1	0.1	0.3
Hf	<u>5.6</u>	5.8	4.8	4.6	<u>4.4</u>	2.7	3.0	3.2
Th	<u>9.6</u>	10.1	16.1	21.6	<u>26.0</u>	4.7	4.8	14.3
U	<u>4.0</u>	4.2	6.9	9.5	<u>11.7</u>	2.0	2.0	6.3

olivine, 26% melilite, 7% clinopyroxene) and ~50% accumulation in the proportions of picrite Ny17–132 (98% olivine, 2% chromite), respectively (Table 5).

The model reproduces all major elements well (Fig. 13), except for TiO₂ which continuously increases in our model up until 4 wt.% (at ±4 wt.% MgO), compared to the 3.3 wt.% observed in our samples at this MgO concentration, implying that our crystallising assemblage is missing a TiO₂ sink. This likely reflects changes in the composition of our spinel phase that have not been taken into account or the cryptic crystallization of a TiO₂-rich phase such as rhönite, observed in experiments (Molendijk et al., 2023), or perovskite, observed in some lavas by Sahama (1968, 1978) and Platz et al. (2004). Trace elements are well-reproduced, though transition metals are too thoroughly depleted and HREE are slightly overestimated (Table 5; Fig. 14; Electronic appendix 2). The former most likely relates to overestimated clinopyroxene crystallization whereas the latter may be an effect of fractionation of apatite, for which we don't have experimentally constrained partition coefficients. Molendijk et al. (2023) performed a similar modelling strategy with only two fractionation steps, switching immediately from olivine, melilite, and clinopyroxene crystallization to a similar late-stage fractionation step to our third. These authors showed that very little nepheline (3%) and leucite (<1%) crystallization was required to adequately reproduce the lava lake trace element composition. However, in effect, their calculated Na₂O and K₂O values are reproduced much less accurately (+2.8 wt.% and –3.39 wt.% misfit, respectively) than those of our new model. These misfits can be minimized by switching to our new starting composition and introducing our first fractionation step, decreasing the Na₂O and K₂O misfits to +0.1 wt.% and –1.31 wt.%, respectively, but introducing new misfits for SiO₂ and CaO (–1.3 wt.% and +1.22 wt.%). The resulting model better reproduces transition metals than our own, depleting them less significantly due to a lower clinopyroxene fraction. Instead, regardless of a lack of leucite crystallization, it severely underestimates leucite-held LILE (Cs, Ba, Rb; 11–28%) as well as LREE (5–14%). Indeed, both models most likely suffer from the absence of applicable partition coefficients for both apatite and spinel, highlighting a clear gap which future work will need to address.

Geothermobarometry

Locating the depths of the major magmatic reservoirs is paramount to understanding any magmatic system and contextualizing the seismic signals it produces. To this end, simple geothermobarometric estimates for Nyiragongo were reported by Platz et al. (2004) based on leucite stability, reports from seismic studies (Tanaka, 1983), and fluid- and melt-inclusion data (Louaradi et al., 1993) indicating primary magmatic reservoirs at 4.1 km (120 MPa) and 10–14 km (320–450 MPa) depth. However, the latter study is an abstract with no further associated published work and should, therefore, be considered with caution. Clinopyroxene geothermometry has so far been limited to the use of the clinopyroxene-only model of Nimis (1995) by Platz et al. (2004), who briefly comment on its agreement with other source of evidence. However, applying the model of Nimis (1995) to our dataset (excluding those outside the compositional range recommended by Nimis (1995)) provides an unrealistic overall pressure distribution of 78 ± 155 MPa, (2.6 ± 5.3 km) with crystals from the 2016 melilitic lavas measuring in at –150 ± 136 MPa (–4.9 ± 4.6 km) and those of primitive lithologies measuring in at 143 ± 131 MPa (4.9 ± 4.5 km) (Figure 15). The uppermost reservoir at Nyiragongo is indeed expected to be located at shallow depth

(e.g. <120 MPa, following Platz et al. (2004)), but clinopyroxene crystals from associated lavas (2016, 2021 eruptive materials) consistently show signs of dissolution and thus disequilibrium (see Mineral textures and Chemistry), as has also been observed by Sahama (1978) and Platz et al. (2004). In addition, seismic observations clearly indicate that the plumbing system to extend to at least 10–15 km depth (Barrière et al., 2019, 2022; Walwer et al., 2023), making it unlikely that all crystallization of this relatively mafic phase (found together with high-Fo olivine at the Rushayo chain) is confined to the uppermost magmatic reservoirs. This pressure underestimation is likely an effect of the silica-undersaturated conditions at Nyiragongo being outside of the calibration range of this barometer (Nimis, 1995). Instead we provide first order estimates acquired with the clinopyroxene-liquid geothermobarometric equations reported by Masotta et al. (2013), the calculations of which can be found in Electronic appendix 1. These authors explicitly included silica-undersaturated compositions in their data-set, expanding upon the work of Putirka et al. (1996) which already included select alkali-rich ugandite compositions. In order to circumvent finding exact equilibrium melts for the clinopyroxene-grains (which would require an equilibrium proxy currently unavailable for these compositions), we used equilibrium estimations of co-existing olivine (Fig. 12d; see above) and assumed that these also applied to co-existing clinopyroxene crystals. In essence, this results in crystals from evolved lithologies being matched with all glasses and whole-rock compositions of their lithology and crystals from olivine-clinopyroxene basalts and micro-olivine basalts being matched with both of these whole-rock groups. The few clinopyroxene crystals measured in picritic melilitite basalts were matched with the olivine-melilitite basalts. As an additional check, crystal-melt matches with a $K_D^{px-liq}_{Fe-Mg}$ -mismatch above 0.05 (calculated with Eqn. 35alk of the same study, SEE of 0.05) were filtered out. The resulting distribution indicates two primary crystallization levels at 370 ± 90 MPa (evolved lithologies) and 790 ± 170 MPa (primitive lithologies) (Fig. 15), which roughly translate to 12.4 ± 3.0 and 26.9 ± 5.7 km depth, somewhat above the moHo, which is estimated to be 35 km deep (Nolet & Mueller, 1982). The existence of two primary magmatic reservoirs is in line with previous observations (e.g. Tanaka, 1983; Demant et al., 1994; Platz et al., 2004; Tedesco et al., 2007), but our barometric results contrast with commonly reported depth estimates which place the upper reservoir around 4 km depth (Platz et al., 2004) and the lower reservoir between 13 and 26 km depth (Tanaka, 1983; Demant et al., 1994). However, because geothermobarometric calculations of any kind are subject to significant uncertainties especially when applied to compositions poorly represented in the calibration dataset (e.g. Wieser et al., 2022), we instead decide to view these results in context of the seismic data reported by Barrière et al. (2019, 2022). These authors found frequent magma injections generating pressure drops in the upper-conduit system around 14 km depth (median of all events), coinciding approximately with the crystallization depth indicated by our main-cone clinopyroxene (Fig. 15). In addition, their deepest reported seismic event occurred at 28 km depth, in agreement with the deepest measurements by Tanaka (1983) as well as our highest pressure estimates. What follows is that the parasitic cone phenocrysts crystallize instead in a ~27 km deep (mush) reservoir, from which very little seismic activity has been reported, likely due to being near- or below the brittle-ductile transition. Magma subsequently travels upwards towards the ~14 km deep zone which is connected with the upper conduit. Given that clinopyroxene thermobarometry only indicates the formation/last equilibration depth of clinopyroxene

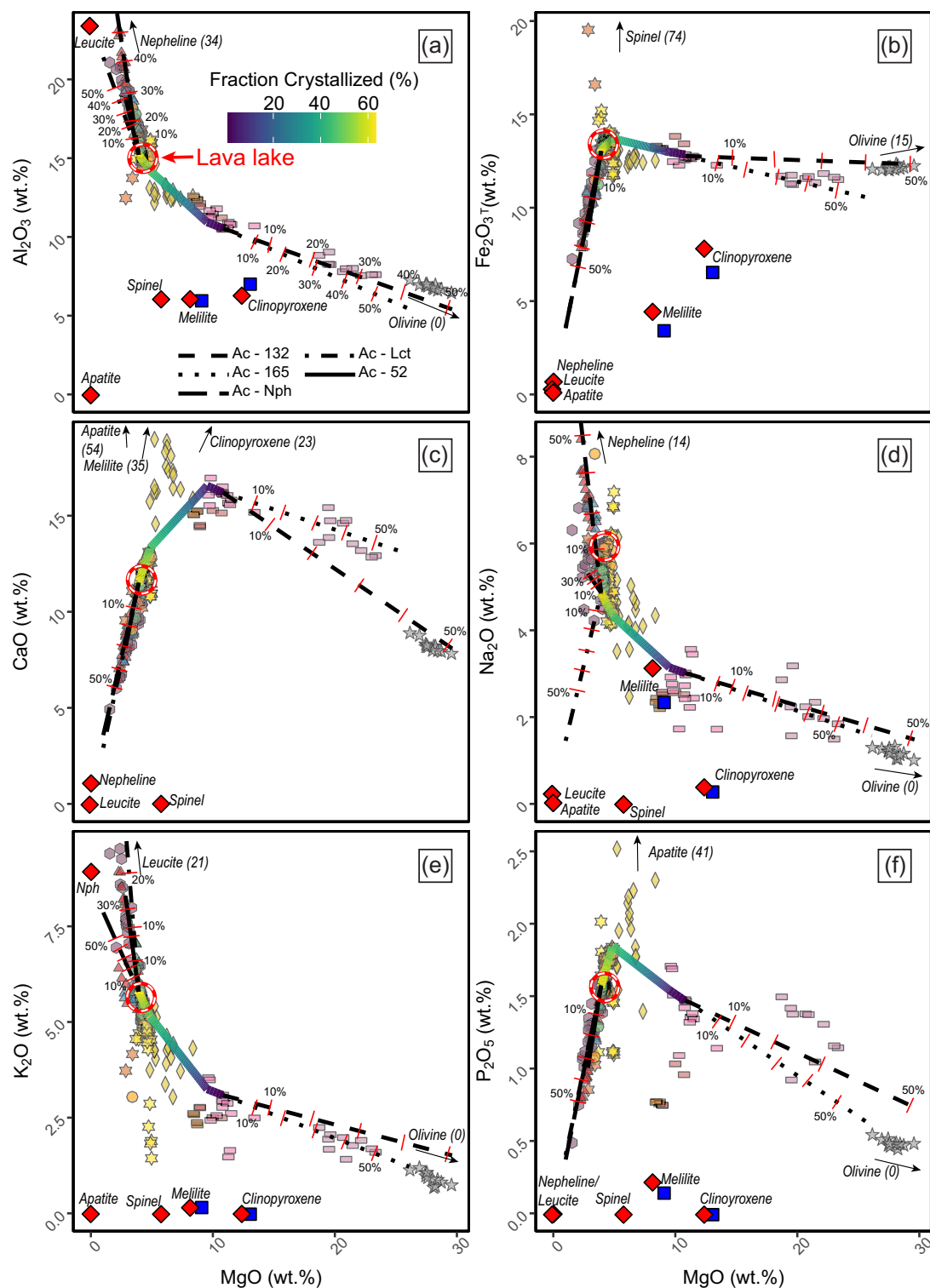


Fig. 13. Harker diagrams as Figure 9 including fractionation path following our numerical modelling approach starting at composition Ny17–160. Black accumulation lines represent direct addition of minerals to either the starting composition or final modelled melt composition in the point-counting proportions of Ny17–132 (Ac - 132), Ny17–165 (Ac - 165), Ny17–052 (Ac-52), pure nepheline (Nph), or pure leucite (Lct). Every 10% of accumulation is marked, though simplified when accumulation trends overlap. Mineral compositions for fractionation and accumulation modes can be found in Table 5. Mineral modes and step-by-step liquid compositions can be found in Table 6. Note that step 1 uses the picritic compositions, step 2 uses the primitive compositions and step 3 uses the evolved compositions of Table 5.

specifically, this hypothesis does not exclude the possibility of a shallower reservoir (<4 km depth) to which these crystals may subsequently have been moved, as suggested by (Platz *et al.*, 2004). In addition, it offers a potential explanation for the

absence of melilite phenocrysts from the eastern cones, given that under volatile-saturated conditions melilite becomes unstable at pressures higher than approximately 610 MPa (20.7 km), forming diopside and calcite (Yoder, 1975). The western cones may,

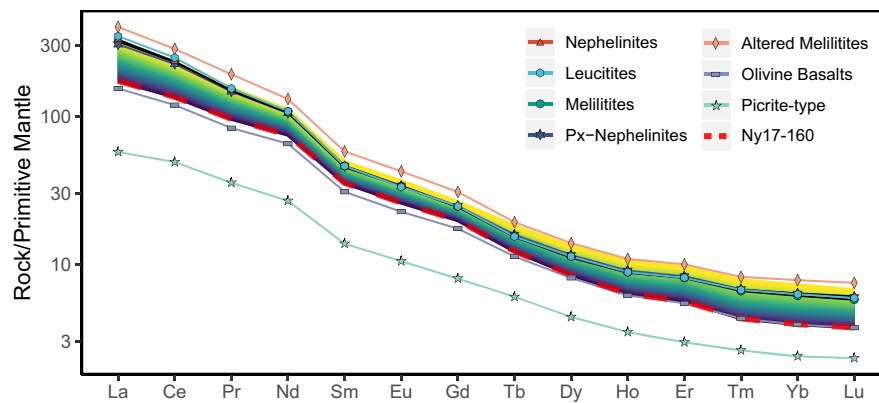


Fig. 14. Primitive-mantle normalized (Sun & McDonough, 1989) multi-element variation diagrams for REE in the modelled melt compositions, overlain by the average compositions of the primary lithological groups. Ny17-160 is additionally marked as the starting composition for the fractionation model.

therefore, tap magmas from slightly shallower reservoirs. Alternatively this contrast can only be explained through variations in CO_2 saturation between the cone regions (Yoder, 1975), variations in silica activity (Carmichael et al., 1970; Gee & Sack, 1988), or compositional difference that we also observe for a variety of elements.

Plumbing system structure

Figure 16 summarizes our observations of the plumbing system. We observe two primary magma reservoirs at 9–15 and 21–33 km depth (see section 4.3). The latter reservoir hosts primitive olivine-melilitite melts and is frequently recharged as ultimately evidenced by the sustained lava lake at the summit which requires a high

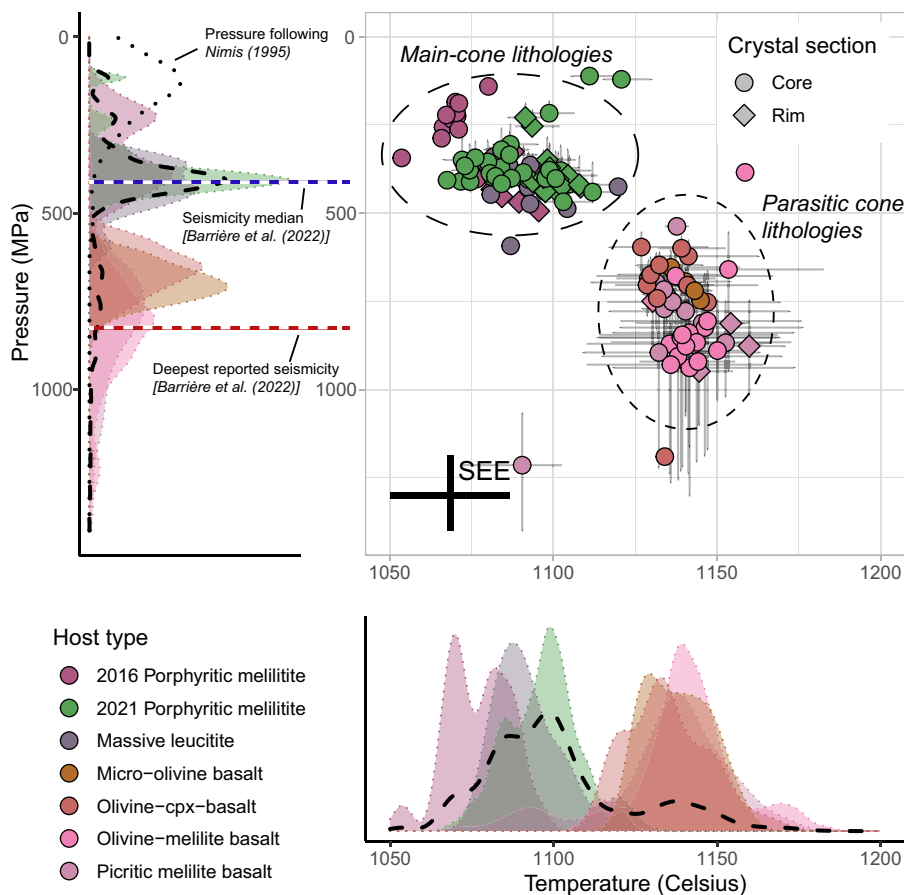


Fig. 15. Pressure-temperature distributions inferred from geothermobarometric calculations using the model of Masotta et al. (2013). Data points represent the mean pressure and temperatures calculated for individual clinopyroxene analyses. Associated error bars represent the range of calculated pressure and temperatures for individual analyses matched with different liquids (whole-rock compositions). Kernel distribution diagrams take into account all possible matches per host-type, with the black dashed line representing the overall distribution. The overall pressure distribution resulting from the model of Nimis (1995), and the median and maximum depths of seismic signals reported by Barrière et al. (2022) are also included for reference.

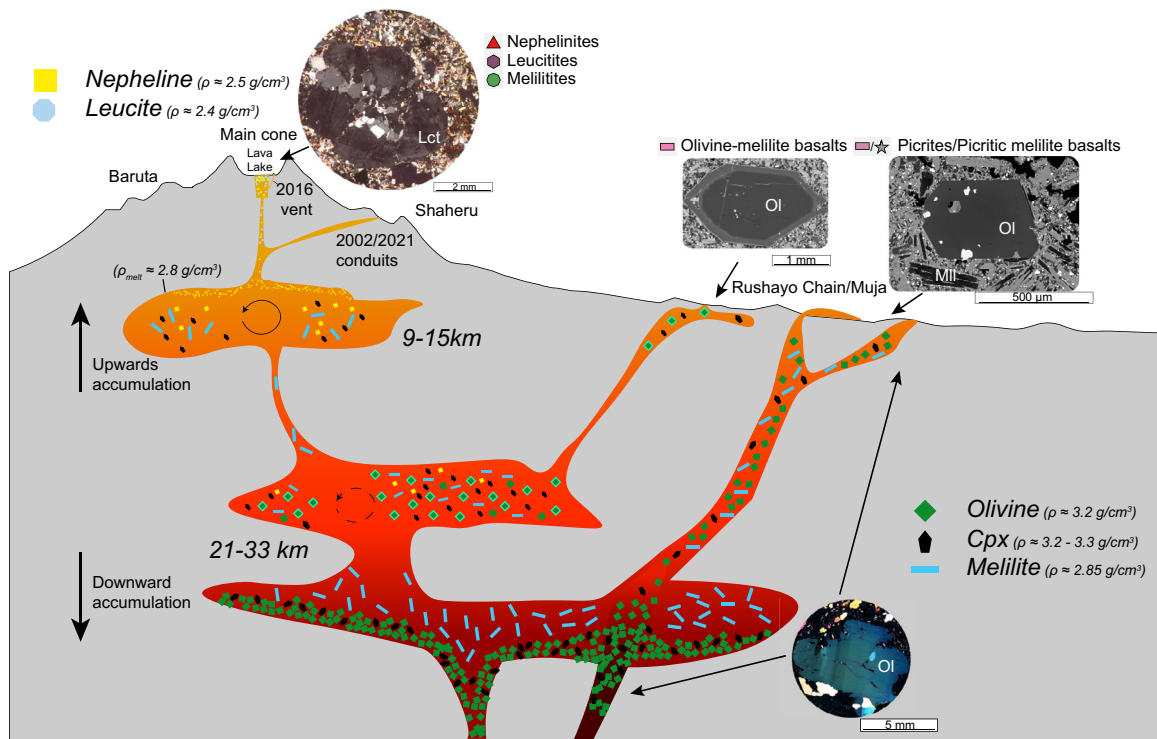


Fig. 16. Schematic model of the Nyiragongo plumbing system based on textural indications and geothermobarometric calculations, indicating olivine and clinopyroxene crystallization and subsequent deposition in deep solid-rich magmatic reservoirs frequently disturbed by mafic recharge. Upper reservoirs are dominated by feldspathoid crystallization and subsequent floatation processes. Representative petrographic images are listed where relevant. Circular arrows indicate a high liquid fraction allowing for crystal convection. Lighter shade rims around olivine represent the normal-zoning features observed in olivine-melilite basalts.

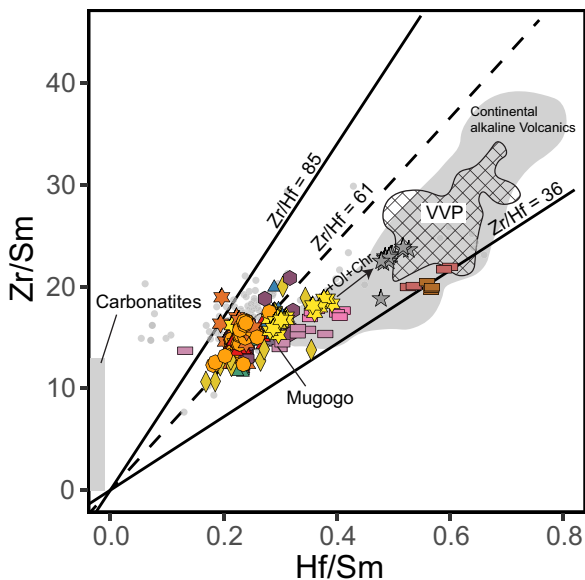


Fig. 17. Hf/Sm Zr/Sm binary trace element diagram after Chakrabarti *et al.* (2009a) and Dupuy *et al.* (1992) for all whole-rock compositions measured by ICP-MS indicating the anomalous nature of the cpx-dominated olivine basalts. Compositions derived from the other volcanic centres are listed following the compilation of Barette *et al.* (2017) under the VVP field, with the exception of Mugogo which plots underneath the Nyiragongo array. Olivine + Chromium accumulation is indicated to explain the lower Zr/Hf ratio of the picrite samples. Symbols and colours follow the same legend as Figure 8.

magma supply rate (Sawyer *et al.*, 2008; Burgi *et al.*, 2014), as well as ubiquitous zoning features in crystal cargoes. Fractional

crystallization of olivine ($\rho \approx 3.2 \text{ g/cm}^3$), melilite ($\rho \approx 2.85 \text{ g/cm}^3$), and minor clinopyroxene ($\rho \approx 3.2 - 3.3 \text{ g/cm}^3$) causes mush-development in this region, which may be partly erupted following mafic recharge events of sufficient magnitude (picrites, picritic olivine-melilite basalts). This mush material may rarely be transported to the upper main cone reservoirs, as was observed in the 2021 eruption (Fig. 3d). As fractionation continues and melt ascends, clinopyroxene crystallization starts to dominate and suspended olivine crystals develop evolved rims (Fig. 6d). Melilite changes in composition but remains in the fractionating assemblage over a wide crystallisation interval. As melts increase in alkali content they are transferred the upper reservoir, in which nepheline ($\rho \approx 2.5 \text{ g/cm}^3$) and leucite ($\rho \approx 2.4 \text{ g/cm}^3$) join the crystallizing assemblage. These phases float in the melt ($\rho \approx 2.8 \text{ g/cm}^3$; Morrison *et al.*, 2020) due to their low density, forming glomerocrysts (Fig. 3a,b). This reservoir is linked directly with the lava lake, as evidenced by the dropping level of the lava lake concurrent with injections of intrusions observed by Barrière *et al.* (2019, 2022). Further melt-evolution is characterized by an increased proportion of leucite in the crystallization assemblage in response to increasing K_2O , as evidenced by the large leucite-glomerocrysts that dominate the main-cone complex (Fig. 2b) and absence thereof from the 2021 eruption materials. Our model agrees in part with those of Sahama (1978), Demant *et al.* (1994), and Platz *et al.* (2004), with crystallization of feldspathoids dominating in upper reservoirs. However, our results indicate that, contrary to Platz *et al.* (2004), leucite crystallization does not dominate fractionation at Nyiragongo, but is rather a final step in response to K_2O oversaturation at low pressures. In addition, our model introduces more thorough constraints on reservoir depths, including a thus far unreported, crystal-rich reservoir at $790 \pm 170 \text{ MPa}$.

Source compositions

Fractionation modelling indicates that the source composition of Nyiragongo lays the foundation for the development of the key geochemical characteristics of Nyiragongo's erupted lithologies, which are only amplified by fractionation, without requiring interaction with crustal lithologies (Molendijk *et al.*, 2023). However, while our modelling efforts adequately explain the progression from olivine-melilite basalt to the lava lake composition, they fail to account for the melilite-deficient olivine basalts from the Mudjoga-Bushwaga-group. In fact, these are the only lithologies that plot outside of the foidite-field on a TAS plot (Fig. 8). They also lack a distinct P_2O_5 enrichment, and are noticeably enriched in select trace elements (e.g. Sc, Fig. 10b). These features may be attributed to the heterogeneous mantle source which is frequently inferred to underlie the VVP (Vollmer & Norry, 1983; Furman & Graham, 1999; Chakrabarti *et al.*, 2009a; Pitcavage *et al.*, 2023). This anomalous mantle source has been inferred to be the result of heterogeneous metasomatism and may vary at a scale down to <1 km (Furman & Graham, 1999). Similarly, the silica-undersaturation of Nyiragongo's magmas has frequently been attributed to carbonate metasomatism of the source lithology, as evidenced by the volcano's high CO_2 output (Aiuppa *et al.*, 2021), groundmass calcite reported by Sahama (1978) and Platz *et al.* (2004), and the highly fractionated Zr/Hf (>70; Fig. 17) and $[Eu]_n/[Ti]_n$ (>1; Fig. 11) ratios of its lavas (Dupuy *et al.*, 1992; Furman & Graham, 1999; Chakrabarti *et al.*, 2009a). While no conclusive magmatic calcite was found in our samples, we do find trace element ratios indicative of carbonate involvement in the form of high Zr/Hf ratios. The Mudjoga-Mushwaga-group lavas also diverge in this respect, with a comparatively low (36) Zr/Hf ratio compared to the main sample array (61) (Fig. 17).

This feature makes these lithologies more akin to the more silica-saturated rocks from the VVP, which have an average Zr/Hf ratio of 45 (Barette *et al.*, 2017 and references therein). Conversely, the silica-undersaturated olivine-melilite basalts erupted by Mugogo volcano (Verhaeghe, 1958; Condomines *et al.*, 2015) plot directly underneath the main Nyiragongo data-set, arguing that this volcanic centre may be tapping into a geochemically similar region of this material to Nyiragongo. In concurrence with various authors (e.g. Chakrabarti *et al.*, 2009a; Minissale *et al.*, 2022) we also observe high Dy/Yb ratios (1.7–2.2) and low K/Rb values (149–380) among our primitive compositions, indicating deep melting in the garnet stability field in the presence of phlogopite. This constrains the depth of melting to between 80 and 150 km depth (Chakrabarti *et al.*, 2009a), but does not necessarily indicate direct plume involvement, which He-isotopes contradict (Pik *et al.*, 2006). Indeed, the thick Tanzanian craton forces melting towards deeper levels (Foley *et al.*, 2012), and we therefore favour a model in which metasomatised lithospheric material is molten (e.g. Muravyeva *et al.*, 2014, 2021; Pitcavage *et al.*, 2021; Minissale *et al.*, 2022) rather than that of a plume head.

CONCLUSIONS

Petrographic and geochemical analyses of eruption products from Nyiragongo provide insights into the plumbing system structure and active processes at this highly active and highly alkaline volcanic system. Whole-rock compositions and fractionation modelling indicate that a large variety of foidite compositions are generated by fractionation and accumulation operating on parental melts with an olivine-melilite basalt-composition. Fractionation extends up to the composition of the lava lake (39–40 wt.% SiO_2 , $Na_2O + K_2O \approx 11$ wt.%), at which point at least 40% of the original

liquid is remaining. Beyond this point, further alkali-enrichment in whole-rock samples is a result of floatation-driven nepheline and leucite accumulation.

Ubiquitous olivine zoning features indicate a variety of interconnected reservoirs in the deep plumbing system, and connectivity up to the upper levels is shown through mafic xenoliths in the 2021 lava flow. Novel Geothermobarometric analysis indicates that the plumbing system extends to a reservoir at near-moho depths (21–33 km) where olivine fractionation and settling produces a mush from which picritic lithologies are derived by means of rapid magma injection and crystal entrainment. At higher levels reservoirs become more liquid dominated, as evidenced by euhedral crystals and repeating compositions among oscillatory-zoned crystals, representing a secondary, stable reservoir of olivine, melilite, and clinopyroxene fractionation. Upper reservoirs are confined to the volcanic edifice and a reservoir at 9–15 km depth in which major clinopyroxene crystallization occurs, in general agreement with seismic observations.

Evaluation of whole-rock trends and comparison with the regional context agrees with the hypotheses of having a heterogeneous metasomatised mantle source underneath the Virunga Volcanic Province, explaining the high diversity of lithologies erupted in this young rift setting.

Acknowledgements

The authors would like to thank Herman Nijs of KU Leuven for assisting in the production of thin sections which were essential to this work. We are grateful to Tilly Bouten and Eric Hellebrand of the microprobe facility at Utrecht University for their assistance with analyses. Helen de Waard is additionally thanked for her help with whole-rock ICP-MS and LA-ICP-MS analyses at Utrecht University. We thank Nicolas Demelle for his assistance in XRF analysis without which this work would not have been possible. We thank an anonymous reviewer for their constructive feedback which significantly improved the manuscript.

Data Availability

The data underlying this article are available in the article and in its online supplementary material.

Supplementary Data

Supplementary data are available at *Journal of Petrology* online.

References

- Aiuppa, A., Casetta, F., Coltorti, M., Stagno, V. & Tamburello, G. (2021). Carbon concentration increases with depth of melting in Earth's upper mantle. *Nature Geoscience* **14**, 697–703. <https://doi.org/10.1038/s41561-021-00797-y>.
- Andersen, T., Elburg, M. A. & Erambert, M. (2012). Petrology of combeite- and götzenite-bearing nephelinite at Nyiragongo, Virunga Volcanic Province in the east African rift. *Lithos* **152**, 105–121. <https://doi.org/10.1016/j.lithos.2012.04.018>.
- Andersen, T., Elburg, M. A. & Erambert, M. (2014). Extreme peralkalinity in delhayelite- and andremeyerite-bearing nephelinite from Nyiragongo volcano, east African rift. *Lithos* **206–207**, 164–178. <https://doi.org/10.1016/j.lithos.2014.07.025>.
- Baker, B. H., Mohr, P. A. & Williams, L. A. J. (1972). Geology of the eastern rift system of Africa. 136 : *Geology of the Eastern Rift System of Africa*, 1–68. <https://doi.org/10.1130/SPE136-p1>.
- Balagizi, C. M., Yalire, M. M., Ciraba, H. M., Kajeje, V. B., Minani, A. S., Kinja, A. B. & Kasereka, M. M. (2016). Soil temperature and CO_2

- degassing, SO₂ fluxes and field observations before and after the February 29, 2016 new vent inside Nyiragongo crater. *Bulletin of Volcanology* **78**, 1–11. <https://doi.org/10.1007/s00445-016-1055-y>.
- Barette, F., Poppe, S., Smets, B., Benbakkar, M. & Kervyn, M. (2017). Spatial variation of volcanic rock geochemistry in the Virunga Volcanic Province: statistical analysis of an integrated database. *Journal of African Earth Sciences* **134**, 888–903. <https://doi.org/10.1016/j.jafrearsci.2016.09.018>.
- Barrière, J., D'Oreye, N., Oth, A., Theys, N., Mashagi, N., Subira, J., Kervyn, F. & Smets, B. (2019). Seismicity and outgassing dynamics of Nyiragongo volcano. *Earth and Planetary Science Letters* **528**, 1–13.
- Barrière, J. et al. (2022). Intra-crater eruption dynamics at Nyiragongo (D.R. Congo), 2002–2021. *Journal of Geophysical Research: Solid Earth* **127**, 2002–2021.
- Batanova, V. G., Thompson, J. M., Danyushevsky, L. V., Portnyagin, M. V., Garbe-Schönberg, D., Hauri, E., Kimura, J. I., Chang, Q., Senda, R., Goemann, K., Chauvel, C., Campillo, S., Ionov, D. A. & Sobolev, A. V. (2019). New olivine reference material for in situ microanalysis. *Geostandards and Geoanalytical Research* **43**, 453–473. <https://doi.org/10.1111/ggr.12266>.
- Beard, C. D., van Hinsberg, V. J., Stix, J. & Wilke, M. (2019). Clinopyroxene/melt trace element partitioning in sodic alkaline magmas. *Journal of Petrology* **60**, 1797–1823. <https://doi.org/10.1093/ptrology/egz052>.
- Bell, K. & Powell, J. L. (1969). Strontium isotopic studies of alkaline rocks: the potassium-rich lavas of the birunga and Toro - ankole regions, east and central equatorial Africa. *Journal of Petrology* **10**, 536–572. <https://doi.org/10.1093/ptrology/10.3.536>.
- Bellon, H. & Pouclot, A. (1980). Datations K-Ar de quelques laves du rift-Ouest de l'Afrique Centrale; implications Sur l'évolution magmatique et structurale. *Geologische Rundschau* **69**, 49–62. <https://doi.org/10.1007/BF01869023>.
- Burgi, P. Y., Darrah, T. H., Tedesco, D. & Eymold, W. K. (2014). Dynamics of the mount Nyiragongo lava lake. *Journal of Geophysical Research: Solid Earth* **119**, 4106–4122. <https://doi.org/10.1002/2013JB010895>.
- Burgi, P. Y., Minissale, S., Melluso, L., Mahinda, C. K., Cuoco, E. & Tedesco, D. (2018). Models of the formation of the 29 February 2016 new spatter cone inside mount Nyiragongo. *Journal of Geophysical Research: Solid Earth* **123**, 9469–9485. <https://doi.org/10.1029/2018JB015927>.
- Carmichael, I. S. E., Nicholls, J. & Smith, A. L. (1970). Silica activity in igneous rocks. *The American Mineralogist* **55**, 246–263.
- Carn, S. A. (2002). Eruptive and passive degassing of Sulphur dioxide at Nyiragongo volcano (D.R. Congo): the 17 January 2002 eruption and its aftermath. *Acta Vulcanologica* **14**(1–2), 1–11.
- Carn, S. A., Fioletov, V. E., Mclinden, C. A., Li, C. & Krotkov, N. A. (2017). A decade of global volcanic SO₂ emissions measured from space. *Scientific Reports* **7**, 1–12. <https://doi.org/10.1038/srep44095>.
- Chakrabarti, R., Basu, A. R., Santo, A. P., Tedesco, D. & Vaselli, O. (2009a). Isotopic and geochemical evidence for a heterogeneous mantle plume origin of the Virunga volcanics, Western rift, east African rift system. *Chemical Geology* **259**, 273–289. <https://doi.org/10.1016/j.chemgeo.2008.11.010>.
- Chakrabarti, R., Sims, K. W. W., Basu, A. R., Reagan, M. & Durieux, J. (2009b). Timescales of magmatic processes and eruption ages of the Nyiragongo volcanics from 238U-230Th-226Ra-210Pb disequilibria. *Earth and Planetary Science Letters* **288**, 149–157. <https://doi.org/10.1016/j.epsl.2009.09.017>.
- Chorowicz, J. (2005). The east African rift system. *Journal of African Earth Sciences* **43**, 379–410. <https://doi.org/10.1016/j.jafrearsci.2005.07.019>.
- Condomines, M., Carpentier, M. & Ongendangenda, T. (2015). Extreme radium deficit in the 1957 AD Mugogo lava (Virunga volcanic field, Africa): its bearing on olivine-melilitite genesis. *Contributions to Mineralogy and Petrology* **169**, 1–19. <https://doi.org/10.1007/s00410-015-1124-9>.
- Cooper, K. M. & Kent, A. J. R. (2014). Rapid remobilization of magmatic crystals kept in cold storage. *Nature Cell Biology* **506**, 480–483. <https://doi.org/10.1038/nature12991>.
- Demant, A., Lestrade, P., Lubala, R. T., Kampunzu, A. B. & Durieux, J. (1994). Volcanological and petrological evolution of Nyiragongo volcano, Virunga volcanic field, Zaire. *Bulletin of Volcanology* **56**, 47–61. <https://doi.org/10.1007/BF00279728>.
- Denaeyer, M. E. (1952) *Resultats scientifiques et techniques de la mission geologique Denaeyer-Hart au Kivu*. Bruxelles: Institut Royal Colonial Belge.
- Denaeyer, M. E. (1963). Les hyaloclastites de la rive Nord du lac Kivu (Congo). *Bulletin Volcanologique* **25**, 201–215. <https://doi.org/10.1007/BF02596551>.
- Denaeyer, M. E. (1966). La rushayite, homologue sodique de la katungite, lave nouvelle du volcan Nyiragongo. *Bulletin de la Societe Francaise de Mineralogie et de Cristallographie* **89**, 107–119. <https://doi.org/10.3406/bulmi.1966.5935>.
- Denaeyer, M. E. (1969). Nouvelles données lithologiques Sur les volcans actifs des Virunga (Afrique Centrale). *Bulletin Volcanologique* **33**, 1128–1144. <https://doi.org/10.1007/BF02597712>.
- Denaeyer, M. E. (1972). Les laves du fossé tectonique de l'Afrique Centrale (Kivu, Rwanda, Toro-Ankole): I. Supplément au recueil d'analyses de 1965 II. Magmatologie III. Magmatogenèse. *Musée royale de l'Afrique centrale - Tervuren Belgique: Annales - Série in -8°, Sciences Géologiques* **72**, 1–134.
- Denaeyer, M. E. (1975) *Le Glacis des Volcans Actifs au Nord du Lac Kivu*, Paris: Mémoires du muséum National d'Histoire Naturelle-Série C-Sciences de la Terre. Muséum national d'Histoire naturelle, pp.37–79.
- Donaldson, C. H. (1979). An experimental investigation of the delay in nucleation of olivine in mafic magmas. *Contributions to Mineralogy and Petrology* **69**, 21–32. <https://doi.org/10.1007/BF00375191>.
- Droop, G. T. R. (1987). A general equation for estimating Fe³⁺ concentrations in ferromagnesian silicates and oxides from microprobe analyses, using stoichiometric criteria. *Mineralogical Magazine* **51**, 431–435. <https://doi.org/10.1180/minmag.1987.051.361.10>.
- Dupuy, C., Liotard, J. M. & Dostal, J. (1992). Zr/Hf fractionation in intraplate basaltic rocks: carbonate metasomatism in the mantle source. *Geochimica et Cosmochimica Acta* **56**, 2417–2423. [https://doi.org/10.1016/0016-7037\(92\)90198-R](https://doi.org/10.1016/0016-7037(92)90198-R).
- Durieux, J. (2004). Volcano Nyiragongo (DR Congo): evolution of the crater and lava lakes from the discovery to the present. *Acta Vulcanologica* **14–15**, 137–144.
- Ebinger, C. J. (1989). Tectonic development of the western branch of the east African rift system. *Geological Society of America Bulletin* **101**, 885–903. [https://doi.org/10.1130/0016-7606\(1989\)101<0885:TDOTWB>2.3.CO;2](https://doi.org/10.1130/0016-7606(1989)101<0885:TDOTWB>2.3.CO;2).
- Ebinger, C. J. & Furman, T. (2003). Geodynamical setting of the Virunga Volcanic Province. *Acta Vulcanologica* **14**, 1–8.
- Ebinger, C. J. & Sleep, N. H. (1998). Cenozoic magmatism throughout East Africa resulting from impact of a single plume. *Nature* **395**, 788–791. <https://doi.org/10.1038/27417>.
- Foley, S. F., Link, K., Tiberindwa, J. V. & Barifaijo, E. (2012). Patterns and origin of igneous activity around the Tanzanian craton. *Journal of African Earth Sciences* **62**, 1–18. <https://doi.org/10.1016/j.jafrearsci.2011.10.001>.
- Furman, T. & Graham, D. (1999). Erosion of lithospheric mantle beneath the east African rift system: geochemical evidence

- from the Kivu volcanic province. *Lithos* **48**, 237–262. [https://doi.org/10.1016/S0024-4937\(99\)00031-6](https://doi.org/10.1016/S0024-4937(99)00031-6).
- Furman, T., Nelson, W. R. & Elkins-Tanton, L. T. (2015). Evolution of the east African rift: drip magmatism, lithospheric thinning and mafic volcanism. *Geochimica et Cosmochimica Acta* **185**, 418–434.
- Gee, L. L. & Sack, R. O. (1988). Experimental petrology of melilitite nephelinites. *Journal of Petrology* **29**, 1233–1255. <https://doi.org/10.1093/petrology/29.6.1233>.
- Gualda, G. A. R., Ghiorso, M. S., Lemons, R. V. & Carley, T. L. (2012). Rhyolite-MELTS: a modified calibration of MELTS optimized for silica-rich, fluid-bearing magmatic systems. *Journal of Petrology* **53**, 875–890. <https://doi.org/10.1093/petrology/egr080>.
- Guillong, M., Meier, D. L., Allan, M. M., Heinrich, C. A. & Yardley, B. W. D. (2008). SILLS: a Matlab-based program for the reduction of laser ablation ICP-MS data of homogeneous materials and inclusions. *Mineralogical Association of Canada Short Course* **40**, 328–333.
- Haapala, I. (2011). Th. G. Sahama's (1910-1983) volcanological and mineralogical studies in Africa: part i. expeditions to the Virunga volcanic field and petrological-mineralogical studies on the Nyiragongo volcano. *Bulletin of the Geological Society of Finland* **83**, 41–55. <https://doi.org/10.17741/bgsf/83.1.003>.
- Hertogen, J., Vanlerberghe, L. & Namegabe, M. R. (1985). Geochemical evolution of the Nyiragongo volcano (Virunga, Western African rift, Zaire). *Bulletin of the Geological Society of Finland* **57**, 21–35. <https://doi.org/10.17741/bgsf/57.1-2.002>.
- Hill, E., Wood, B. J. & Blundy, J. D. (2000). The effect of Ca-Tschemm component on trace element partitioning between clinopyroxene and silicate melt. *Lithos* **53**, 203–215. [https://doi.org/10.1016/S0024-4937\(00\)00025-6](https://doi.org/10.1016/S0024-4937(00)00025-6).
- Hoffman, C., Courtillot, V., Feraud, G., Rochette, P., Yirgu, G., Ketefo, E. & Pik, R. (1997). Timing of the Ethiopian flood basalt event: implications for plume birth and global change. *Nature* **389**, 838–841. <https://doi.org/10.1038/39853>.
- Holness, M. B., Stock, M. J. & Geist, D. (2019). Magma chambers versus mush zones: constraining the architecture of sub-volcanic plumbing systems from microstructural analysis of crystalline enclaves. *Philosophical Transactions of the Royal Society A: Mathematical, Physical and Engineering Sciences* **377**, 20180006. <https://doi.org/10.1098/rsta.2018.0006>.
- Jochum, K. P., Stoll, B., Herwig, K., Willbold, M., Hofmann, A. W., Amini, M., Aarburg, S., Abouchami, W., Hellebrand, E., Mocek, B., Raczek, I., Stracke, A., Alard, O., Bouman, C., Becker, S., Dücking, M., Brätz, H., Klemm, R., de Bruin, D., Canil, D., Cornell, D., de Hoog, C. J., Dalpé, C., Danyushevsky, L., Eisenhauer, A., Gao, Y., Snow, J. E., Groschopf, N., Günther, D., Latkoczy, C., Guillong, M., Hauri, E. H., Höfer, H. E., Lahaye, Y., Horz, K., Jacob, D. E., Kasemann, S. A., Kent, A. J. R., Ludwig, T., Zack, T., Mason, P. R. D., Meixner, A., Rosner, M., Misawa, K., Nash, B. P., Pfänder, J., Premo, W. R., Sun, W. D., Tlepolo, M., Vannucci, R., Vennemann, T., Wayne, D. & Woodhead, J. D. (2006). MPI-DING reference glasses for in situ microanalysis: new reference values for element concentrations and isotope ratios. *Geochemistry, Geophysics, Geosystems* **7**. <https://doi.org/10.1029/2005GC001060>.
- Kahl, M., Chakraborty, S., Costa, F., Pompilio, M. & Bove, V. (2011). Dynamic plumbing system beneath volcanoes revealed by kinetic modeling, and the connection to monitoring data: an example from Mt. Etna. *Earth and Planetary Science Letters* **308**, 11–22. <https://doi.org/10.1016/j.epsl.2011.05.008>.
- Kampunzu, A. B., Bonhomme, M. G. & Kanika, M. (1998). Geochronology of volcanic rocks and evolution of the Cenozoic Western branch of the east African rift system. *Journal of African Earth Sciences* **26**, 441–461. [https://doi.org/10.1016/S0889-5362\(98\)00025-6](https://doi.org/10.1016/S0889-5362(98)00025-6).
- Komorowski, J.-C. et al. (2002). The January 2002 flank eruption of Nyiragongo volcano (Democratic Republic of Congo): chronology, evidence for a tectonic rift trigger, and impact of lava flows on the city of Goma. *Acta Vulcanologica* **14**, 27–62.
- Kress, V. C. & Carmichael, I. S. E. (1991). The compressibility of silicate liquids containing Fe₂O₃ and the effect of composition, temperature, oxygen fugacity and pressure on their redox states. *Contributions to Mineralogy and Petrology* **108**, 82–92. <https://doi.org/10.1007/BF00307328>.
- Lebas, M. J., Le Maitre, R. N., Streckeis, A. & Zanettin, B. (1986). A chemical classification of volcanic rock based on total silica diagram. *Journal of Petrology* **27**, 745–750. <https://doi.org/10.1093/petrology/27.3.745>.
- Liang, Y. (2003). Kinetics of crystal-melt reaction in partially molten silicates: 1. Grain scale processes. *Geochemistry, Geophysics, Geosystems* **4**, 1–27.
- Longerich, H. P., Jackson, S. E. & Günther, D. (1996). Laser ablation inductively coupled plasma mass spectrometric transient signal data acquisition and Analyte concentration calculation. *Journal of Analytical Atomic Spectrometry* **11**, 899–904. <https://doi.org/10.1039/JA961100899>.
- Louaradi, D., Clochiatti, R., Pineau, F. & Javoy, M. (1993). Magma storage beneath Nyiragongo volcano (Zaire): evidence from fluid and melt inclusions. *Terra Abstracts* **5**, 573.
- Masotta, M., Mollo, S., Freda, C., Gaeta, M. & Moore, G. (2013). Clinopyroxene-liquid thermometers and barometers specific to alkaline differentiated magmas. *Contributions to Mineralogy and Petrology* **166**, 1545–1561. <https://doi.org/10.1007/s00410-013-0927-9>.
- McConnel, R. B. (1972). Geological development of the rift system of eastern Africa. *Geological Society of America Bulletin* **83**, 2549–2572. [https://doi.org/10.1130/0016-7606\(1972\)83\[2549:GDOTRS\]2.0.CO;2](https://doi.org/10.1130/0016-7606(1972)83[2549:GDOTRS]2.0.CO;2).
- Minissale, S., Zanetti, A., Tedesco, D., Morra, V. & Melluso, L. (2019). The petrology and geochemistry of Nyiragongo lavas of 2002, 2016, 1977 and 2017 AD, and the trace element partitioning between melilitite glass and melilitite, nepheline, leucite, clinopyroxene, apatite, olivine and Fe-Ti oxides: a unique scenario. *Lithos* **332-333**, 296–311. <https://doi.org/10.1016/j.lithos.2019.02.023>.
- Minissale, S., Casalini, M., Cucciniello, C., Balagizi, C., Tedesco, D., Boudoire, G., Morra, V. & Melluso, L. (2022). The geochemistry of recent Nyamulagira and Nyiragongo potassic lavas, Virunga Volcanic Province, and implications on the enrichment processes in the mantle lithosphere of the Tanzania-Congo craton. *Lithos* **420-421**, 106696. <https://doi.org/10.1016/j.lithos.2022.106696>.
- Molendijk, S. M., Namur, O., Mason, P. R. D., Dubacq, B., Smets, B., Neave, D. A. & Charlier, B. (2023). Trace element partitioning in silica-undersaturated alkaline magmatic systems. *Geochimica et Cosmochimica Acta* **346**, 29–53. <https://doi.org/10.1016/j.gca.2023.01.025>.
- Moore, A., Coogan, L. A., Costa, F. & Perfit, M. R. (2014). Primitive melt replenishment and crystal-mush disaggregation in the weeks preceding the 2005–2006 eruption 9° 50' N, EPR. *Earth and Planetary Science Letters* **403**, 15–26. <https://doi.org/10.1016/j.epsl.2014.06.015>.
- Morrison, A., Whittington, A., Smets, B., Kervyn, M. & Sehlke, A. (2020). The rheology of crystallizing basaltic lavas from Nyiragongo and Nyamuragira volcanoes, D.R.C. *Volcanica* **3**, 1–28. <https://doi.org/10.30909/vol.03.01.0128>.
- Moussallam, Y., Oppenheimer, C., Scaillet, B., Buisman, I., Kimball, C., Dunbar, N., Burgisser, A., Ian Schipper, C., Andújar, J. & Kyle, P. (2015). Megacrystals track magma convection between reservoir

- and surface. *Earth and Planetary Science Letters* **413**, 1–12. <https://doi.org/10.1016/j.epsl.2014.12.022>.
- Muravyeva, N. S., Belyatsky, B. V., Senin, V. G. & Ivanov, A. V. (2014). Sr – Nd – Pb isotope systematics and clinopyroxene-host disequilibrium in ultra-potassic magmas from Toro-Ankole and Virunga, east-African rift : implications for magma mixing and source heterogeneity. *Lithos* **210–211**, 260–277. <https://doi.org/10.1016/j.lithos.2014.09.011>.
- Muravyeva, N. S., Senin, V. G., Ivanov, A. V. & Belyatsky, B. V. (2021). Leucite basanites of Virunga (east African rift): some insights into petrogenesis and source composition. *Lithos* **384–385**, 105972–105925. <https://doi.org/10.1016/j.lithos.2021.105972>.
- Namur, O., Montalbano, S., Bolle, O. & Vander Auwera, J. (2020). Petrology of the April 2015 eruption of Calbuco volcano, southern Chile. *Journal of Petrology* **61**(8), 1:33.
- Nimis, P. (1995). A clinopyroxene geobarometer for basaltic systems based on crystal-structure modeling. *Contributions to Mineralogy and Petrology* **121**, 115–125. <https://doi.org/10.1007/s004100050093>.
- Nkoubou, C., Déruelle, B. & Velde, D. (1995). Petrology of Mt Etinde nephelinite series. *Journal of Petrology* **36**, 373–395. <https://doi.org/10.1093/petrology/36.2.373>.
- Nolet, G. & Mueller, S. (1982). A model for the deep structure of the east African rift system from simultaneous inversion of Teleseismic data. *Tectonophysics* **84**, 151–178. [https://doi.org/10.1016/0040-1951\(82\)90158-5](https://doi.org/10.1016/0040-1951(82)90158-5).
- Pik, R., Marty, B. & Hilton, D. R. (2006). How many mantle plumes in Africa? The geochemical point of view. *Chemical Geology* **226**, 100–114. <https://doi.org/10.1016/j.chemgeo.2005.09.016>.
- Pitcavage, E., Furman, T., Nelson, W. R., Kalegga, P. K. & Barifajjo, E. (2021). Petrogenesis of primitive lavas from the Toro Ankole and Virunga volcanic provinces : Metasomatic mineralogy beneath East Africa's Western rift. *Lithos* **396–397**, 106192–106397. <https://doi.org/10.1016/j.lithos.2021.106192>.
- Pitcavage, E., Furman, T., Nelson, W. R., Graham, D. W., Shirey, S., Kulyanyingi, P. K. & Barifajjo, E. (2023). Geochemical constraints on the origin of primitive Potassic lavas in the eastern Virunga Volcanic Province. *Geochemistry, Geophysics, Geosystems* **24**, 1–18. <https://doi.org/10.1029/2023GC010950>.
- Platz, T., Foley, S. F. & André, L. (2004). Low-pressure fractionation of the Nyiragongo volcanic rocks, Virunga Province, D.R. Congo. *Journal of Volcanology and Geothermal Research* **136**, 269–295. <https://doi.org/10.1016/j.jvolgeores.2004.05.020>.
- Poppe, S., Smets, B., Fontijn, K., Rukeza, M. B., De Marie Fikiri Migabo, A., Milungu, A. K., Namogo, D. B., Kervyn, F. & Kervyn, M. (2016). Holocene phreatomagmatic eruptions alongside the densely populated northern shoreline of Lake Kivu, east African rift: timing and hazard implications. *Bulletin of Volcanology* **78**. <https://doi.org/10.1007/s00445-016-1074-8>.
- Pottier, Y. (1978). Première éruption historique du Nyiragongo et manifestations adventives simultanées du volcan Nyamuragira (chaîne des Virunga-Kivu-Zaire: Déc 76 - Juin 77). *Mus R Afr Centr-Tervuren Belg, Dépt Géol Min Rapp ann*, 157–175.
- Poucllet, A. & Bram, K. (2021). Nyiragongo and Nyamuragira: a review of volcanic activity in the Kivu rift, western branch of the east African rift system. *Bulletin of Volcanology* **83**. <https://doi.org/10.1007/s00445-021-01435-6>.
- Putirka, K., Johnson, M., Kinzler, R., Longhi, J. & Walker, D. (1996). Thermobarometry of mafic igneous rocks based on clinopyroxene-liquid equilibria, 0–30 kbar. *Contributions to Mineralogy and Petrology* **123**, 92–108. <https://doi.org/10.1007/s004100050145>.
- Sahama, T. G. (1953a). Mineralogy and petrology of a lava flow from Mt. Nyiragongo, Belgian Congo. *Annales Academiae Scientiarum Fennicae A III*.
- Sahama, T. G. (1953b). Parallel growth of nepheline and microp-erthitic kalsilite from north Kivu, Belgian Congo. *Annales Academiae Scientiarum Fennicae A III*.
- Sahama, T. G. (1960). Kalsilite in the lavas of Mt. Nyiragongo (Belgian Congo). *Journal of Petrology* **1**, 146–171. <https://doi.org/10.1093/petrology/1.2.146>.
- Sahama, T. G. (1962). Petrology of Mt. Nyiragongo: a review. *Transactions of the Edinburgh Geological Society* **19**, 1–28. <https://doi.org/10.1144/transed.19.1.1>.
- Sahama, T. G. (1964). Genesis of the Nyiragongo lavas. *Bulletin Volcanologique* **27**, 195. <https://doi.org/10.1007/BF02597520>.
- Sahama, T. G. (1968). Mineralogical composition of the Nyiragongo rocks. *Geologische Rundschau* **57**, 904–914. <https://doi.org/10.1007/BF01845372>.
- Sahama, T. G. (1973). Evolution of the Nyiragongo magma. *Journal of Petrology* **14**(1), 33–48. <https://doi.org/10.1093/petrology/14.1.33>.
- Sahama, T. G. (1978). The Nyiragongo main cone. *Musée royale de l'Afrique centrale - Tervuren Belgique: Annales - Série in –8°, Sciences Géologiques* **81**, 88.
- Sahama, T. G. & Hytönen, K. (1957). Götzenite and combeite, two new silicates from the Belgian Congo. *Mineralogical Magazine and Journal of the Mineralogical Society* **31**, 503–510. <https://doi.org/10.1180/minmag.1957.031.238.01>.
- Sahama, T. G. & Meyer, A. (1958). Study of the volcano Nyiragongo. A progress report. *Exploration du Parc National Albert. Mission d'études volcanologiques. Fascicule 2. Bruxelles: Institut des Parcs Nationaux du Congo Belge*.
- Santo, A. P., Capaccioni, B., Tedesco, D. & Vaselli, O. (2002). Petrographic and geochemical features of the 2002 Nyiragongo lava flows. *Acta Vulcanologica* **14**, 63–66.
- Sawyer, G. M., Carn, S. A., Tsanev, V. I., Oppenheimer, C. & Burton, M. (2008). Investigation into magma degassing at Nyiragongo volcano, Democratic Republic of the Congo. *Geochemistry, Geophysics, Geosystems* **9**, 1–17. <https://doi.org/10.1029/2007GC001829>.
- Schwindinger, K. R. & Anderson, A. T. (1989). Synneusis of Kilauea Iki olivines. *Contributions to Mineralogy and Petrology* **103**, 187–198. <https://doi.org/10.1007/BF00378504>.
- Smets, B. & Poppe, S. (2016). Volcanological map of Nyamulagira and Nyiragongo, Virunga Volcanic Province, north Kivu, Democratic Republic of Congo. Scale: 1/100,000. *Tervuren : Royal Museum for Central Africa*.
- Smets, B., Kervyn, M., Oreye, N. & Kervyn, F. (2015). Spatio-temporal dynamics of eruptions in a youthful extensional setting: insights from Nyamulagira volcano (D.R. Congo), in the western branch of the east African rift. *Earth Science Reviews* **150**, 305–328. <https://doi.org/10.1016/j.earscirev.2015.08.008>.
- Smets, B., d'Oreye, N., Kervyn, M. & Kervyn, F. (2017). Gas piston activity of the Nyiragongo lava lake: first insights from a stereographic time-lapse camera system. *Journal of African Earth Sciences* **134**, 874–887. <https://doi.org/10.1016/j.jafrearsci.2016.04.010>.
- Smittarello, D., Smets, B., Barrière, J., Michellier, C., Oth, A., Shreve, T., Grandin, R., Theys, N., Brenot, H., Cayol, V., Allard, P., Caudron, C., Chevrel, O., Darchambeau, F., de Buyl, P., Delhayé, L., Derauw, D., Ganci, G., Geirsson, H., Kamate Kaleghetso, E., Kambale Makundi, J., Kambale Nguomoja, I., Kasereka Mahinda, C., Kervyn, M., Kimanuka Ruriho, C., le Mével, H., Molendijk, S., Namur, O., Poppe, S., Schmid, M., Subira, J., Wauthier, C., Yalire, M., d'Oreye, N., Kervyn, F. & Syavulisembo Muhindo, A. (2022). Precursor-free eruption triggered by edifice rupture at Nyiragongo volcano. *Nature* **609**, 83–88. <https://doi.org/10.1038/s41586-022-05047-8>.

- Smittarello, D., Grandin, R., Jaspard, M., Derauw, D., Oreya, N. & Shreve, T. (2023). Nyiragongo crater collapses measured by multi-sensor SAR amplitude time series journal of geophysical research : solid earth. *Journal of Geophysical Research: Solid Earth* **128**. <https://doi.org/10.1029/2023JB026683>.
- Stamps, D. S., Calais, E., Saria, E., Hartnady, C., Nocquet, J., Ebinger, C. J. & Fernandes, R. M. (2008). A kinematic model for the east African rift. *Geophysical Research Letters* **35**, 1–6. <https://doi.org/10.1029/2007GL032781>.
- Streck, M. J. (2008). Mineral textures and zoning as evidence for open system processes. *Reviews in Mineralogy and Geochemistry* **69**, 595–622. <https://doi.org/10.2138/rmg.2008.69.15>.
- Sun, C. & Liang, Y. (2012). Distribution of REE between clinopyroxene and basaltic melt along a mantle adiabat: effects of major element composition, water, and temperature. *Contributions to Mineralogy and Petrology* **163**, 807–823. <https://doi.org/10.1007/s00410-011-0700-x>.
- Sun, S.-S. & McDonough, W. F. (1989). Chemical and isotopic systematics of oceanic basalts: implications for mantle composition and processes. *Geological Society, London, Special Publications* **42**, 313–345. <https://doi.org/10.1144/GSL.SP.1989.042.01.19>.
- Tanaka, K. (1983). Seismicity and focal mechanisms of the volcanic earthquakes in the Virunga volcanic region. *Volcanoes Nyiragongo and Nyamuragira: geophysical aspects* **19**, 28.
- Tazieff, H. (1949). Première exploration du cratère du volcan Nyiragongo. *Bulletin de la Société Belge de Géologie* **58**, 165–172.
- Tedesco, D. (2002). The pre-2002 activity - 1995 Nyiragongo and Nyamulagira activity in the Virunga National Park: a volcanic crisis. *Acta Vulcanologica* **14/15**, 149–155.
- Tedesco, D., Vaselli, O., Papale, P., Carn, S. A., Voltaggio, M., Sawyer, G. M., Durieux, J., Kasereka, M. & Tassi, F. (2007). January 2002 volcano-tectonic eruption of Nyiragongo volcano, Democratic Republic of Congo. *Journal of Geophysical Research: Solid Earth* **112**, 1–12. <https://doi.org/10.1029/2006JB004762>.
- Thonnard, R. L. G. & Denaeyer, M. E. (1965). Carte volcanologiques des Virunga, Feuille no. 1: Groupe occidental. *Centre National de Volcanologie (Belgium)*.
- Toplis, M. J. (2005). The thermodynamics of iron and magnesium partitioning between olivine and liquid: criteria for assessing and predicting equilibrium in natural and experimental systems. *Contributions to Mineralogy and Petrology* **149**, 22–39. <https://doi.org/10.1007/s00410-004-0629-4>.
- Ubide, T., Mollo, S., Zhao, J. X., Nazzari, M. & Scarlato, P. (2019). Sector-zoned clinopyroxene as a recorder of magma history, eruption triggers, and ascent rates. *Geochimica et Cosmochimica Acta* **251**, 265–283. <https://doi.org/10.1016/j.gca.2019.02.021>.
- Vergnolle, S. & Métrich, N. (2022). An interpretative view of open - vent volcanoes. *Bulletin of Volcanology* **84**. <https://doi.org/10.1007/s00445-022-01581-5>.
- Verhaeghe, M. A. P. (1958) Le Volcan Mugogo. *Éruption du 1er août 1957. Exploration du Parc National Albert, Mission d'études volcanologiques. Fascicule 3*. Bruxelles: Institut des Parcs Nationaux du Congo Belge.
- Vollmer, R. & Norry, M. J. (1983). Unusual isotopic variations in Nyiragongo nephelinites. *Nature* **301**, 141–143. <https://doi.org/10.1038/301141a0>.
- Walwer, D., Wauthier, C., Barrière, J., Smittarello, D., Smets, B. & Oreya, N. (2023). Modeling the intermittent lava Lake drops occurring between 2015 and 2021 at Nyiragongo volcano. *Geophysical Research Letters* **1**, 12.
- Wauthier, C., Cayol, V., Kervyn, F. & D'Oreya, N. (2012). Magma sources involved in the 2002 Nyiragongo eruption, as inferred from an InSAR analysis. *Journal of Geophysical Research: Solid Earth* **117**, 1–20. <https://doi.org/10.1029/2011JB008257>.
- Wauthier, C., Cayol, V., Smets, B., D'Oreya, N. & Kervyn, F. (2015). Magma pathways and their interactions inferred from InSAR and stress modeling at Nyamulagira volcano, D.R. Congo. *Remote Sensing* **7**, 15179–15202. <https://doi.org/10.3390/rs71115179>.
- Welsch, B., Hammer, J., Baronnet, A., Jacob, S., Hellebrand, E. & Sinton, J. (2016). Clinopyroxene in postshield Haleakala ankaramite: 2. Texture, compositional zoning and supersaturation in the magma. *Contributions to Mineralogy and Petrology* **171**, 1–19.
- Wieser, P. E., Edmonds, M., Maclennan, J. & Wheeler, J. (2020). Microstructural constraints on magmatic mushes under Kilauea volcano, Hawai'i. *Nature Communications* **11**, 1–14. <https://doi.org/10.1038/s41467-019-13635-y>.
- Wieser, P. E., Kent, A. J. R., Till, C. B., Donovan, J., Neave, D. A., Blatter, D. L. & Krawczynski, M. J. (2022). Barometers behaving badly: assessing the influence of analytical and experimental uncertainty on clinopyroxene thermobarometry calculations at crustal conditions. *Journal of Petrology*, 14.
- Wood, B. J. & Trigila, R. (2001). Experimental determination of aluminous clinopyroxene-melt partition coefficients for potassic liquids, with application to the evolution of the Roman province potassic magmas. *Chemical Geology* **172**, 213–223. [https://doi.org/10.1016/S0009-2541\(00\)00259-X](https://doi.org/10.1016/S0009-2541(00)00259-X).
- Yoder, H. S. (1975). Relationship of melilite-bearing rocks to kimberlite: a preliminary report on the system akermanite-CO₂. *Physics and Chemistry of the Earth* **9**, 883–894. [https://doi.org/10.1016/0079-1946\(75\)90058-0](https://doi.org/10.1016/0079-1946(75)90058-0).